

ZAHID ULLAH KHAN

Synthesis and characterization of multicolor-emitting
quantum dots: insight into study in RAW macrophages
for the development of bionanoprobe

São Paulo

2020

ZAHID ULLAH KHAN

Síntese e caracterização de quantum dots de emissão multicolorida:
insight de um estudo com macrófagos RAW para o desenvolvimento de
bionanossondas

Tese apresentada ao Programa de Pós- Graduação Interunidades
em Biotecnologia da Universidade de São Paulo, Instituto
Butantan e Instituto de Pesquisas Tecnologia para obtenção do
Título de Doutor em Biotecnologia.

Área de concentração: Biotecnologia

Orientador: Prof. Dr. Magnus Ake Gidlund

Versão corrigida. A versão original encontra-se disponível na
Secretaria de Pós-graduação que aloja o Programa de Pós-
Graduação.

São Paulo

2020

ZAHID ULLAH KHAN

Synthesis and characterization of multicolor-emitting quantum dots:
insight into study in RAW macrophages for the development of
bionanoprobe

Thesis submitted to the Interunit Postgraduate Program in
Biotechnology, University of São Paulo, Institute of Butantan
and Institute of Technology Research to obtain the title of Doctor
in Biotechnology..

Concentration area: Biotechnology

Orientador: Prof. Dr. Magnus Ake Gidlund

Corrected version. The original version is available from the
Graduate Secretariat hosting the Graduate Program.

São Paulo

2020

CATALOGAÇÃO NA PUBLICAÇÃO (CIP)

Serviço de Biblioteca e Informação Biomédica

Instituto de Ciências Biomédicas

Universidade de São Paulo

Ficha Catalográfica elaborada pelo autor

Ullah Khan, Zahid

Synthesis and characterization of multicolor-emitting quantum dots: insight into study in RAW macrophages for the development of bionanoprobe / Zahid Ullah Khan; orientador Magnus Ake Gidlund. -- São Paulo, 2020.

164 p.

Tese (Doutorado) -- Universidade de São Paulo, Instituto de Ciências Biomédicas.

1. Quantum dots. 2. RAW macrophages. 3. cell viability. 4. fluorescence imaging. 5. cellular uptake mechanism of QDs. I. Ake Gidlund, Magnus, orientador. II. Título.

UNIVERSIDADE DE SÃO PAULO

Programa de Pós-Graduação Interunidades em Biotecnologia

Universidade de São Paulo, Instituto Butantan, Instituto de Pesquisas Tecnológicas
Candidato: Zahid Ullah Khan

Titulo da Tese: Síntese e caracterização de quantum dots de emissão multicolorida: insight de um estudo com macrófagos RAW para o desenvolvimento de bionanossondas

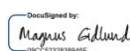
Orientador: Prof. Dr. Magnus Ake Gidlund

A Comissão Julgadora dos trabalhos de Defesa da Tese de Doutorado, em sessão pública realizada a 13/10/2020 considerou.

(x) Aprovado

() Reprovado

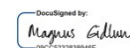
Examinador: Assinatura



Nome: Beate Saegesser Santos

Instituição: UFPE- Departamento de Ciências Farmacêuticas

Examinador: Assinatura



Nome: Henrique Andrade Rodrigues da Fonseca

Instituição: EPM-UNIFESP

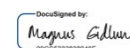
Examinador: Assinatura



Nome: Elizabeth Natal de Gaspari

Instituição: IAL(ICB)

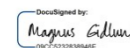
Examinador: Assinatura



Nome: Henrique Eisi Toma

Instituição: IQ - USP

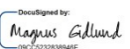
Examinador: Assinatura



Nome: Maria Claudia França da Cunha Felinto

Instituição: IPEN(IPEN)

Presidente: Assinatura



Nome: Magnus Ake Gidlund

Instituição: ICB-USP



Cidade Universitária "Armando de Salles Oliveira", Butantã, São Paulo, SP - Av. Professor Lineu Prestes, 2415 - ICB III - 05508 000
Comissão de Ética em Pesquisa - Telefone(11) 3091-7733 - e-mail: cep@icb.usp.br

CERTIFICADO DE ISENÇÃO

Certificamos que o Protocolo CEP-ICB nº**1118/2020** referente ao projeto intitulado: **"Síntese e caracterização de quantum dots de emissão multicolorida: insight de um estudo com macrófagos RAW para o desenvolvimento de bionanossondas"**, sob a responsabilidade do(a) aluno(a) **Zahid Ullah Khan**, e orientação do(a) Prof.(a) Dr.(a) **Magnus Ake Gidlund**, do Programa de Pós-Graduação Interunidades em Biotecnologia, foi analisado pela **CEUA** - Comissão de Ética no Uso de Animais e pelo **CEPSH** - Comitê de Ética em Pesquisa com Seres Humanos, tendo sido deliberado que o referido projeto não utilizará animais que estejam sob a égide da Lei nº 11.794, de 8 de outubro de 2008, nem envolverá procedimentos regulados pela Resolução CONEP nº 466/2012.

São Paulo, 21 de julho de 2020.

Profa. Dra. **Luciane Valéria Sita**
CoordenadoraCEUA ICB/USP

Profa. Dra. **Camila Squarzoni Dale**
CoordenadoraCEPSH ICB/USP

Dedication

Dedicated to the spring of love—my parents.

ACKNOWLEDGMENTS

“In the name of Allah, the Most Beneficent, the Most Merciful.”

I would like to express my gratitude to all those at the Institute of Biomedical Sciences, Institute of Chemistry, and Institute of Tropical Medicine, University of Sao Paulo, who helped me to accomplish the work. I would also like to express my rich gratitude to my honorable mentors, collaborators, fellow friends, and facilitators especially to:

My Supervisor Prof. Dr. Magnus Ake Gidlund, who supported me, invigorated my spirit and left no stone unturned to unveil the mysteries and turn into a reality with me throughout the memorable peregrination of my Doctorate.

Prof. Dr. Hermi Felinto de Brito (IQ-USP), who provided me a pleasant environment, all the available facilities, and opportunity to guide me and work under his magnificent guardianship.

My brother Dr. Latif Ullah Khan from Synchrotron-light for Experimental Science and Applications in the Middle East (SESAME), who assisted me in the characterization of quantum dots and removed all the hurdles and smoothed the pathway to the final achievement of my Doctorate.

My mentor and friend Dr. Mayara Klimuk Uchiyama (IQ-USP), who played key role in the study and created the possibilities out of impossibilities by her sincere affection and consistent endeavors.

My collaborators and friends Prof. Dr. Hiro Goto, Dr. Eduardo, and Dr. Luiza from IMT-USP, who facilitated me magnanimously in the work.

My friends and lab fellows, Dr. Cassio, Dr. César, Dr. Helliomar, Dr. Israel, Dr. Leonnam, Dr. Tiago Ian, Lucca, Matheus from IQ-USP, who never made me felt alone by their memorable company, and assisted me generously in the exigency.

My collaborator, Dr. Maria Claudia França da Cunha Felinto, who provided me facility installed in the Instituto de Pesquisas Energéticas e Nucleares (IPEN).

Dr. Marta M. Antoniazzi and Simone G. S. Jared, who provided a transmission electron microscope facility installed in the Laboratory of Structural Biology, Institute of Butantan.

I am grateful to the Programa de Pós-Graduação Interunidades em Biotecnologia, Universidade de São Paulo for providing me the opportunity, guidance, and all the available facilities to make the work possible.

I gratefully acknowledge the financial support extended by “The World Academy of Sciences for the advancement of science in developing countries (TWAS)” and Conselho Nacional de Desenvolvimento Científico e Tecnológico (CNPq), (No. 190932/2015-5).

“The most beautiful things have been hidden or made invisible, and the most wonderful amusement has been preserved in the playing with them.”

(Zahid Khan)

ABSTRACT

Khan, Z.U. **Synthesis and characterization of multicolor-emitting quantum dots: insight into study in RAW macrophages for the development of bionanoprobe** 2020. 164p. Ph.D. Thesis - Instituto de Ciências Biomédicas (Immunologia), Universidade de São Paulo, São Paulo, 2020.

The design and development of new generation bionanoprobes is strictly relied upon the precise and previous knowledge of particle-cell behavior, movement of a particle in and out of the cell, and the fate of particle in the course. The ability to manipulate and overcome the cell and particle activities are the prerequisite to enhance the diagnostic sensitivity and therapeutic efficiency. The current work aimed to unravel the intrinsic potentials of different quantum dots (QDs) for the future development of bionanoprobe utilized in the diagnosis and monitoring of macrophages-mediated disorders such as atherosclerosis, osteoporosis, autoimmune diseases, etc. Initially, different types of highly photoluminescence QDs, encompassing ZnSe:Mn²⁺, multicolor-emitting ZnSe:Eu²⁺/Mn²⁺@ZnS, color-tunable CdSe/ZnS, and CdS/ZnS were synthesized *via* a high-temperature organo-metals method, rendered water-soluble by ligand exchange approach and determined their physicochemical and photoluminescence properties. The QDs presented excellent colloidal stability, good dispersion in a biological medium, intense photoluminescence emission, small size between 4-7 nm, and high crystallinity. The QDs were evaluated in a murine macrophage cell line, RAW 264.7, and analyzed qualitatively and quantitatively by CytoViva® Hyperspectral enhanced dark-field and dual-mode fluorescence (DMF) imaging system, transmission electron microscopy (TEM), and flow cytometry (FACS). Various cytotoxicity assays containing annexin V/propidium iodide assay, MTT assay, trypan blue exclusion assay, and assay for apoptosis-linked gene expression were performed, confirming no noticeable deleterious effect of QDs on cells within the desired incubation period. The QDs presented efficient cellular uptake and gave an intense fluorescent signal that enabled us to detect easily through the fluorescence microscopy and FACS. Besides that, the cellular uptake of QDs at a lower temperature (4 °C) was significantly depleted or completely halted in some cases, indicating a preferential uptake mechanism by energy-dependent endocytic pathways. The QDs were observed to adhere to cell membranes, both singly and aggregately, before being endocytosed by a specific pathway. To elucidate the endocytosis pathways, cells were treated with QDs in the presence of different pathway-specific pharmacological inhibitors: amiloride, phenylarsine oxide, sucrose, methyl-β-cyclodextrin and cytochalasin D. The obtained results indicated that the cellular uptake of all QDs was facilitated predominantly *via* clathrin and/or caveolae-mediated endocytosis, as expected. However, in the case of ZnSe:Eu²⁺/Mn²⁺@ZnS, (CdSe/ZnS)_A and

(CdSe/ZnS)_B the cellular internalization was also executed by additional pathways of micropinocytosis or phagocytosis. Conclusively, the QDs presented excellent colloidal stability, high cell viability, enhanced fluorescence signal in cells, and distinct entry pathway in RAW macrophages, suggesting them interesting candidates to explore for the development of future bionanoprobe used for diagnosis of macrophages-mediated disorders.

Keywords: Quantum dots, RAW macrophages, cell viability, fluorescence imaging, and cellular uptake mechanism of QDs.

RESUMO

Khan, Z. U. **Síntese e caracterização de quantum dots de emissão multicolorida: insight de um estudo com macrófagos RAW para o desenvolvimento de bionanossondas.** 2020. 164p. Tese (Doutorado em Imunologia) – Instituto de Ciências Biomédicas (Imunologia), Universidade de São Paulo, São Paulo, 2020.

O design e o desenvolvimento de uma nova geração de nanossondas são estritamente baseados no conhecimento preciso e prévio do comportamento entre células-nanopartículas, no movimento das partículas dentro e fora da célula, além de seu destino durante o percurso. A capacidade de manipular e superar as atividades de células e partículas são o pré-requisito para aprimorar a sensibilidade do diagnóstico e a eficiência terapêutica. O presente trabalho visou desvendar a potencialidade intrínseca de vários *quantum dots* (QDs) para o desenvolvimento futuro de nanossondas para o diagnóstico e monitoramento de distúrbios mediados por macrófagos como aterosclerose, osteoporose, doenças autoimunes, etc. Inicialmente, diferentes tipos de QDs de alta fotoluminescência, consistindo em ZnSe:Mn²⁺, ZnSe:Eu²⁺/Mn²⁺@ZnS de emissão de multicores, CdSe/ZnS que emite cor a depender de seu tamanho e CdS/ZnS foram sintetizados por método organometálico de alta temperatura, e tornados solúveis em água pelo método de troca de ligantes, determinando suas propriedades físico-químicas e ópticas. Os QDs apresentaram boa estabilidade coloidal, boa dispersão em meios biológicos, intensa emissão fotoluminescente, tamanho pequeno entre 4-7 nm e alta cristalinidade. Foi avaliado o efeito dos QDs na linhagem celular de macrófago murino, RAW 264.7, e analisados qualitativa e quantitativamente pelo ultramicroscópio hiperespectral de campo escuro e de fluorescência CytoViva®, microscopia eletrônica de transmissão (TEM) e citometria de fluxo (FACS). Foram realizados ensaios de citotoxicidade como de anexina V/iodeto de propídio, MTT, exclusão por azul de tripano e ensaio de expressão de genes ligados à apoptose, onde não confirmaram qualquer efeito deletério óbvio dos QDs nas células, dentro do período de incubação estudado. A captação celular dos QDs foi muito eficiente e forneceu um sinal intenso de fluorescência que permitiu sua detecção facilmente através de microscopia de fluorescência e FACS. Além disso, a captação celular de QDs em baixas temperaturas (4 °C) foi significativamente diminuída ou completamente interrompida em alguns casos, indicando uma preferência pelo mecanismo de endocitose dependente de energia. Foi também observado que os QDs aderem levemente e agregam à membrana celular antes de serem endocitadas por um caminho específico. Para elucidar as vias de endocitose, as células foram tratadas com QDs na presença de diferentes inibidores farmacológicos específicos da via: amilorida, óxido de fenilarsina, sacarose,

metil- β -ciclodextrina e citocalasina D. Os resultados obtidos indicaram que a captação celular foi predominantemente facilitada via endocitose mediada por clatrina e/ou caveolae para todos os QDs, como esperado. Entretanto, no caso dos ZnSe:Eu²⁺/Mn²⁺@ZnS, (CdSe/ZnS)_A e (CdSe/ZnS)_B a internalização celular foi também executada por outros caminhos como micropinocitose ou fagocitose. Conclusivamente, os QDs apresentaram boa estabilidade coloidal, alta viabilidade celular, sinal de fluorescência aprimorado nas células e vias de entrada distintas em macrófagos RAW, sugerindo que os QDs aqui estudados são candidatos interessantes a serem explorados para o desenvolvimento de futuras nanossondas para diagnóstico de distúrbios mediados por macrófagos.

Palavras-chave: Pontos quânticos, macrófagos RAW, viabilidade celular, imagem por fluorescência e mecanismo de captação celular de QDs.

LIST OF FIGURES

Figure 1.1 - Size-dependent bandgap engineering and discrete energy states formation in QDs (a) and photographs of different colors of QDs.....	28
Figure 1.2 - Representative diagrams of bands alignment in core-shell QDs.....	31
Figure 1.3 - Schematic illustration of partial energy transfer mechanism in E^{2+} and Mn^{2+} doped ZnSe QDs.....	32
Figure 1.4 - Schematic representation of CdTe QDs preparation via organo-metals procedure.....	34
Figure 1.5 - A schematic of a Teflons [®] lined stainless steel autoclave typically used in the laboratory for hydrothermal/solvothermal syntheses.....	36
Figure 1.6 - Fluorescence images of cells stained with QDs.....	40
Figure 1.7 - Schematic representation of endocytic pathways utilized by cells in the uptake of nanoparticles.....	45
Figure 4.2.1 - Schematic illustration of the ligand exchange reaction of OA/OLA/DDT capped ZnSe: Mn^{2+} QDs with 3-MPA organic ligand to become aqueous soluble.....	72
Figure 4.2.2 - XRD patterns of ZnSe and ZnSe: xMn^{2+} ($x = 5, 10, \text{ and } 15 \text{ mol}\%$) QDs.....	73
Figure 4.2.3 - XPS spectra, including wide-scan or survey (a), high resolution spectra measured in bonding energy ranges of Zn 2p (b), Se 3d (c), Mn 2p (c), S 2p (e), O 1s (f) and C 1s (g) signals for the 3-Mercaptopropionic acid capped Mn^{2+} doped ZnSe QDs.....	75
Figure 4.2.4 - AFM topography (a), phase contrast images (b) and height profile (Z-dimension) histogram (c) of 3-MPA capped ZnSe: Mn^{2+} QDs, bright-field (BF) (d), high-angle annular dark-field (HAADF) (e), HRTEM images (f-g) and histogram of particle size distribution (h) of OLA capped ZnSe: Mn^{2+} QDs.....	76
Figure 4.2.5 - Particles size distribution histogram of ZnSe: Mn^{2+} QDs suspension in Milli-Q water (a), RPMI+FBS (10%) cell culture medium (b), FBS (100%) (c), and Zeta potential in Milli-Q water (d) and RPMI+FBS (10%) (e).....	77
Figure 4.2.6 - UV-Visible absorption spectra (a), excitation spectra (b), emission spectra (c), partial energy level diagrams, blue color dashed arrow denotes energy transfer, and the blue, dark bluish, and yellow color downward wide arrows represent the radiative decays from bandgap, surface traps, and dopant Mn^{2+} ion, respectively (d), luminescence decay curves (e) and digital photograph (f) of ZnSe: xMn^{2+} QDs under UV irradiation lamp ($\lambda = 365 \text{ nm}$).....	79

Figure 4.3.1 - Schematic illustration of core ZnSe:xEu ²⁺ /yMn ²⁺ (x = 4, 8, and 12; y = 12 mol%) and ZnSe:xEu ²⁺ /yMn ²⁺ @ZnS core-shell QDs preparation.....	81
Figure 4.3.2 - Schematic illustration and digital photographs of phase transfer of ZnS passivated ZnSe:xEu ²⁺ ,yMn ²⁺ (x, y = 12 mol%) core-shell QDs solution from chloroform layer to water layer after ligand exchange reaction, under UV irradiation lamp ($\lambda = 365$ nm).....	82
Figure 4.3.3 - X-ray diffraction patterns of ZnSe:xEu ²⁺ /yMn ²⁺ (x = 4, 8, and 12; y = 0 and 12 mol%) and ZnS passivated ZnSe:xEu ²⁺ ,yMn ²⁺ (x, y = 12 mol%) and ZnSe:Eu ²⁺ (4 mol%) core-shell QDs.....	83
Figure 4.3.4 - AFM topography 2 and 3-dimensional images (a-c) and histogram of grain size distribution of ZnS passivated ZnSe:xEu ²⁺ ,yMn ²⁺ @ZnS (x, y = 12 mol%) core-shell QDs.....	84
Figure 4.3.5 - HRTEM images and EDS spectra of ZnSe:xEu ²⁺ ,yMn ²⁺ (a,b,d), and ZnS passivated ZnSe:xEu ²⁺ ,yMn ²⁺ (x, y = 12 mol%) (c,e) QDs.....	85
Figure 4.3.6 - Size-distribution histogram (by number) of ZnSe:xEu ²⁺ ,yMn ²⁺ @ZnS (x, y = 12 mol%) core-shell QDs in (a-c) Milli-Q water, FBS (10%) supplemented RPMI, and pure FBS (100%) media and (d and e) zeta potential in water and FBS (10%) supplemented RPMI media, respectively.....	87
Figure 4.3.7 - UV-visible absorption spectra (a), excitation (b), and emission spectra (c) of ZnSe and ZnSe:Mn ²⁺ (12 mol%) QDs.....	88
Figure 4.3.8 - UV-visible absorption spectra (a), excitation spectra (b-c), emission spectra (d), schematic representation of energy level diagram, grey arrow denotes photogenerated electron-hole pair (exciton), left blue arrow represents radiative recombination of exciton, second right black denotes interconfigurational transition from 4f ⁷ ground level to the 4f ⁶ 5d ¹ state of the Eu ²⁺ ion, black dashed arrows indicate energy transfer to dopant impurities, right blue and red arrows illustrate the radiative decays for Eu ²⁺ and Mn ²⁺ ions, respectively (e), and digital photographs of ZnSe:Eu ²⁺ (4mol%) and ZnSe:xEu ²⁺ ,yMn ²⁺ (x = 4 and 12; y = 12 mol%) QDs, under UV irradiation lamp at $\lambda = 365$ nm (f).....	89
Figure 4.3.9 - UV-visible absorption spectra (a), excitation spectra (b), and emission spectra of ZnS (3 and 4 MLs) passivated ZnSe:Eu ²⁺ (4 mol%) ZnSe:xEu ²⁺ ,yMn ²⁺ (x, y = 12 mol%) core-shell QDs (c) The abbreviation “ML” in the inset stands for the monolayers of ZnS shell materials.....	90
Figure 4.3.10 - Luminescence decay curves and lifetimes of representative ZnSe:xEu ²⁺ ,yMn ²⁺ (x = 4, 8, and 12; y = 12 mol%) and ZnSe:xEu ²⁺ ,yMn ²⁺ @ZnS (x, y = 12 mol%) samples monitored by excitation at 365 nm and emission at 586 nm. The inset shows the variation of lifetime of Mn ²⁺ based on increasing the content of Eu ²⁺	92

Figure 4.4.1 - Schematic illustration of nucleation processes of core CdSe and preparation of (CdSe/ZnS) _A , (CdSe/ZnS) _B , and (CdSe/ZnS) _C core-shell QDs.....	93
Figure 4.4.2 - Schematic illustration and digital photographs of (CdSe/ZnS) _A (top) and (CdSe/ZnS) _B (bottom) core-shell QDs solutions phase transfer from chloroform layer to water layer after treatment with 3-MPA (HS(CH ₂) ₂ COOH) ligand, under irradiation of UV lamp ($\lambda= 365$ nm).....	94
Figure 4.4.3 - XRD patterns of unpassivated CdSe and 3MLs of ZnS passivated orange-emitting (CdSe/ZnS) _A , green-emitting (CdSe/ZnS) _B , and blue-emitting (CdSe/ZnS) _C core-shell QDs.....	95
Figure 4.4.4 - HRTEM images (different magnifications) and histogram of particles size distributions of the core CdSe (a-c) and green-emitting core-shell (CdSe/ZnS) _B (d-f) QDs.....	96
Figure 4.4.5 - Size-distribution histogram of orange-emitting (CdSe/ZnS) _A (a-c) and green-emitting (CdSe/ZnS) _B (d-f) core-shell QDs in Milli-Q water, FBS (10%) supplemented RPMI, and pure FBS (100%) media (a-c). Zeta potential of (CdSe/ZnS) _A (g) and (ZnSe/ZnS) _B (h) core-shell QDs in Milli-Q wate.....	98
Figure 4.4.6 - UV-visible absorption spectra (a), excitation spectra (b), emission spectra (c), and photographs under UV light (d) of CdSe, orange-emitting (CdSe/ZnS) _A , green-emitting (CdSe/ZnS) _B , and blue-emitting (CdSe/ZnS) _C core-shell QDs.....	100
Figure 4.5.1 - Schematic illustration and digital photographs of CdS/ZnS core-shell QDs solutions phase transfer from the chloroform layer to water layer after ligand exchange reaction, under irradiation of UV lamp ($\lambda= 365$ nm).....	102
Figure 4.5.2 - XRD patterns of ZnS, unpassivated CdSe and 3-6MLs of ZnS passivated CdS core-shell QDs.....	103
Figure 4.5.3 - AFM topography (a), phase contrast images (b), height profile (Z-dimension) histogram (c), HRTEM images (different magnifications) (d,e) and histogram of particles size distributions (f) of 3-MPA capped CdS/ZnS QDs.....	104
Figure 4.5.4 - Size-distribution histogram of CdS/ZnS core-shell QDs in Milli-Q water (a), FBS (10%) supplemented RPMI (b), pure FBS (100%) (c), and zeta-potential in Milli-Q water.....	105
Figure 4.5.5 - UV-visible absorption spectra (a), excitation spectra (b) and emission spectra (c) of 6MLs ZnS passivated CdS core-shell QDs.....	107
Figure 5.1.1 - Cytotoxicity assessment of ZnSe:Mn ²⁺ QDs: annexin V/PI assay (a), apoptosis-linked genes expressed level of mRNA of pro-apoptotic gene Bax (b) and anti-apoptotic gene Bcl-2 (c).....	110
Figure 5.1.2 - Cellular viability assessment of QDs by trypan blue dye exclusion assay.....	111

Figure 5.1.3 - CytoViva hyperspectral enhanced dark-field images of ZnSe:Mn ²⁺ treated cells obtained at different time intervals.....	112
Figure 5.1.4 - CytoViva enhanced dark-field and dual-mode fluorescence (DMF) images of live cells treated with ZnSe:Mn ²⁺ QDs.....	113
Figure 5.1.5 - TEM images of control and ZnSe:Mn ²⁺ treated cells obtained after different incubation periods.....	114
Figure 5.1.6 - Effect of pathway-specific inhibitors on ZnSe:Mn ²⁺ QDs uptake.....	115
Figure 5.2.1 - Effect of ZnSe:xEu ²⁺ ,yMn ²⁺ @ZnS (x, y = 12 mol%) QDs on cell viability and activation.....	118
Figure 5.2.2 - Dual mode CytoViva enhanced dark-field and fluorescence images of cells treated with ZnSe:xEu ²⁺ ,yMn ²⁺ @ZnS (x, y = 12 mol%) QDs.....	119
Figure 5.2.3 - TEM images of cellular uptake and colocalization of ZnSe:xEu ²⁺ ,yMn ²⁺ @ZnS (x, y = 12 mol%) QDs.....	120
Figure 5.2.4 - CytoViva enhanced dark-field and dual-mode fluorescence (DMF) images of multicolor-emitting ZnSe:xEu ²⁺ ,yMn ²⁺ @ZnS (x, y = 12 mol%) QDs.....	121
Figure 5.2.4 - CytoViva enhanced dark-field and dual-mode fluorescence (DMF) images of time-dependent uptake and exocytosis.....	122
Figure 5.2.5 - Quantitative analyses of ZnSe:xEu ²⁺ ,yMn ²⁺ @ZnS (x, y = 12 mol%) QDs uptake mechanism by FACS.....	125
Figure 5.3.1 - Effects of orange-emitting (CdSe/ZnS) _A (left) and green-emitting CdSe/ZnS) _A (right) QDs (25, 50, and 100 µg/mL) on cell viability of RAW macrophages incubated for 24 and 48 hours.....	127
Figure 5.3.2 - CytoViva enhanced dark-field and dual-mode fluorescent images (DMF) images of live RAW macrophages stained with orange-emitting (CdSe/ZnS) _A (A) and green-emitting (CdSe/ZnS) _B (B) QDs.....	128
Figure 5.3.3 - FACS quantitative analyses of the influence of pathway-specific inhibitors on orange-emitting (CdSe/ZnS) _A (A) and green-emitting (CdSe/ZnS) _B (B) QDs uptake.....	130
Figure 5.3.4 - Effect of pathway-specific inhibitors on orange-emitting (CdSe/ZnS) _A (left) and green-emitting (CdSe/ZnS) _B (right) QDs.....	131
Figure 5.4.1 - Effect of CdS/ZnS QDs (25, 50, and 100 µg/mL) on the cell viability of RAW macrophages incubated for 24 and 48 hours.....	133
Figure 5.4.2 –CytoViva enhanced dark-field and dual-mode fluorescence images of live RAW cells treated with red-emitting CdS/ZnS QDs.....	134
Figure 5.4.3 – FACS analyses of the effect of pathway-specific inhibitors on red-emitting CdS/ZnS QDs.....	135

LIST OF SCHEMES

Figure 3.1 - Flow chart diagram (left) and the representative reaction assembly (right) for the ZnSe:xMn ²⁺ (x = 5, 10, and 15 mol%) QDs synthesis <i>via</i> organo-metals approach.....	51
Figure 3.2 - Schematic illustration of the syntheses of ZnSe:xEu ²⁺ /yMn ²⁺ (x = 4, 8, and 12; y = 0 and 12 mol%) core (left) and ZnSe:xEu ²⁺ /yMn ²⁺ @ZnS core-shell (right) QDs...	54
Figure 3.3 - Schematic illustration of CdSe core (left) and CdSe/ZnS core-shell QDs (right) preparation.....	57
Figure 3.4 - Flow chart diagrams of core CdS (left) and CdS/ZnS core-shell (right) QDs preparation.....	60
Figure 3.5 - Flow chart diagram of aqueous solubilization of QDs <i>via</i> ligand exchange reaction.....	61

ABBREVIATIONS AND SYMBOLS

τ : Fluorescence lifetime

3-MPA: 3-Mercaptopropionic acid

AFM: Atomic Force Microscope

CB: Conduction Band

CME: Clathrin-mediated Endocytosis

CvME: Caveolae-mediated Endocytosis

Cyt D: Cytochalasin D

DDT: 1-Dodecanethiol

DLS: Dynamic Light Scattering

DMEM: Dulbecco's Modified Eagle Medium

DMSO: Dimethyl sulfoxide

dNTP: Deoxyribonucleotide Triphosphate

EDS: Energy Dispersive X-Ray Spectroscopy

eV: Electron Volt

FACS: Fluorescence-activated Cell Sorting

FBS: Fetal Bovine Serum

FWHM: Full Width at Half Maximum

HRTEM: High-resolution Transmission Electron Microscope

M β CD: Methyl- β -cyclodextrin

MLs: Monolayers

MTT: 3-(4,5-dimethylthiazol-2-yl)-2,5-diphenyltetrazolium bromide

mV: Millivolt

OA: Oleic Acid

ODE: 1-Octadecene

OLA: Oleyl Amine

PAO: Phenylarsine Oxide

PBS: Phosphate Buffered Saline

PCR: Polymerase Chain Reaction

PI: Propidium Iodide

PL: Photoluminescent

QY: Quantum Yield

RNA: Ribonucleic Acid

ROS: Reactive Oxygen Species

RPMI: Roswell Park Memorial Institute

TEM: Transmission Electron Microscope

XPS: X-ray Photoelectron Spectrometer

XRD: X-ray Diffraction

ζ: Zeta-potential

λ: Wavelength

TABLE OF CONTENTS

1 INTRODUCTION.....	
1.1 Introduction to Semiconductor Quantum Dots (QDs).....	27
1.2. Surface Modification and Types of QDs.....	28
1.2.1. Surface Passivation.....	28
1.2.2. Core-Shell QDs.....	29
1.2.3. Type-I and Inverse Type-I QDs.....	29
1.2.4. Type II QDs.....	30
1.2.5. Quasi-Type II QDs.....	30
1.2.6. Dopant Impurities.....	31
1.3. Synthetic Approaches to QDs Preparation.....	32
1.3.1. Organo-metals Method.....	32
1.3.2. Aqueous Rout to QDs Synthesis.....	34
1.3.3. Hydrothermal/Solvothermal Approach to QDs Synthesis.....	35
1.3.4. Biosynthesis of QDs.....	36
1.3.5. Surface Chemistry of QDs.....	37
1.4. Biomedical Applications of QDs.....	37
1.4.1. QDs Induced Toxicity.....	38
1.4.2. Biosensing.....	39
1.4.3. Bioimaging.....	39
1.5. Factors Affecting the Cellular Uptake of Particles.....	41
1.6. Uptake Mechanism of Nanoparticles.....	41
1.6.1. Phagocytosis.....	42
1.6.2. Pinocytosis.....	43
2 OBJECTIVES.....	47
3 EXPERIMENTAL SECTION.....	
Experimental Part A.....	49
3.1. Reagents and solvents.....	49
3.2. Preparation of ZnSe:xMn ²⁺ (x = 5, 10, and 15 mol%) QDs.....	50
3.2.1. Synthesis of ZnSe:Mn ²⁺ QDs.....	50
3.3. Preparation of ZnSe:xEu ²⁺ /yMn ²⁺ and ZnSe:xEu ²⁺ /yMn ²⁺ @ZnS QDs.....	52
3.3.1. Synthesis of core ZnSe: xEu ²⁺ ,yMn ²⁺ (x = 4, y = 12 mol%) QDs.....	52

3.3.2. Surface passivation of ZnSe:xEu ²⁺ ,yMn ²⁺ and ZnSe: xEu ²⁺ with ZnS monolayers.....	53
3.3.2.1. Synthesis of ZnSe:xEu ²⁺ /yMn ²⁺ @ZnS core-shell QDs.....	53
3.4. Preparation of CdSe and CdSe/ZnS core-shell QDs.....	55
3.4.1. Synthesis of core CdSe QDs.....	55
3.4.2. Preparation of color-tunable CdSe/ZnS core-shell QDs.....	55
3.4.2.1. Synthesis of CdSe/ZnS core-shell QDs.....	56
3.5. Preparation of CdS and CdS/ZnS core-shell QDs.....	58
3.5.1. Synthesis of CdS QDs.....	58
3.5.2. Surface passivation of CdS core by ZnS shell.....	58
3.5.2.1. Synthesis of CdS/ZnS core-shell QDs.....	59
3.6. Aqueous solubilization of QDs <i>via</i> ligand exchange reaction.....	61
3.7. Materials characterization.....	62
3.7.1. X-ray Diffraction (XRD).....	62
3.7.2. Transmission Electron Microscope (TEM).....	62
3.7.3. Dynamic Light Scattering (DLS).....	62
3.7.4. Atomic Force Microscope (AFM).....	62
3.7.5. X-ray Photoelectron Spectrometer (XPS).....	63
3.7.6. Photoluminescent Spectroscopy.....	63
3.7.7. UV-visible Absorption Spectroscopy.....	63
Experimental Part B.....	64
3.8. Cell Culture Growth.....	64
3.8.1. Cells counting.....	64
3.9. Toxicity Assessment of QDs in RAW Macrophages.....	64
3.9.1. Trypan blue exclusion assay.....	65
3.9.2. MTT and Griess assay.....	65
3.9.3. Annexin V/Propidium (PI) staining assay.....	66
3.9.4. Quantitative PCR for the expression of pro- and anti-apoptotic macrophage genes.....	67
3.10. Time-dependent Uptake and Imaging of QDs in RAW Macrophages.....	67
3.10.1. CytoViva hyperspectral microscopy imaging and mapping.....	68
3.10.3. Transmission electron microscopy imaging.....	68
3.11. Uptake Mechanism of QDs in RAW Macrophages.....	69
3.11.1. Microplate reader analysis.....	69
3.11.2. Flow cytometry (FACS) analysis.....	70

3.4.10. Statistical analysis.....	70
4 CHARACTERIZATION OF QDs.....	
4.1. Color-tunable fluorescent quantum dots.....	72
4.2. Orange-emitting ZnSe:xMn ²⁺ (x = 5, 10, and 15 mol%) QDs.....	72
4.2.1. Physicochemical characterization.....	73
4.2.2. Photoluminescence study.....	77
4.3. Multicolor-tunable ZnSe:Eu ²⁺ /Mn ²⁺ @ZnS Core-Shell QDs.....	81
4.3.1. Physicochemical characterization.....	82
4.3.2. Photoluminescence study.....	87
4.4. Color-tuning via interfacial alloying in CdSe/ZnS nanocrystals.....	93
4.4.1. Physicochemical characterization.....	94
4.4.2. Photoluminescence study.....	98
4.5. Red-emitting CdS Core and CdS/ZnS Core-Shell QDs.....	102
4.5.1. Physicochemical characterization.....	102
4.5.2. Photoluminescence study.....	106
5 DEVELOPMENT OF BIONANOPROBE.....	
5.1. Orange-emitting ZnSe:Mn ²⁺ QDs as a Bionanoprobe for Macrophages.....	109
5.1.1. Assessment of QDs Cytotoxicity.....	109
5.1.2. Time-dependent uptake of QDs.....	111
5.5.3. Cellular Uptake Mechanism of QDs.....	114
5.2. Wide Visible-Range Fluorescence ZnSe:Eu ²⁺ /Mn ²⁺ @ZnS QDs as Nanoprobe for Bioimaging.....	117
5.2.1. Assessment of QDs Cytotoxicity.....	117
5.2.2. Fluorescence Imaging of QDs in RAW Cells.....	118
5.2.3. Time-dependent uptake and exocytosis of QDs.....	121
5.2.4. Cellular Uptake Mechanism of QDs.....	122
5.3. Exploring the Potentials of Color-tunable CdSe/ZnS QDs as Nanoprobe for Macrophages.....	126
5.3.1. Assessment of QDs Cytotoxicity.....	126
5.3.2. Fluorescence Imaging of QDs in RAW Cells.....	127
5.3.3. Cellular Uptake Mechanism of QDs.....	128
5.4. Developing the Red-emitting CdS/ZnS Core-Shell QDs Based Nanoprobe For Macrophages.....	132
5.4.1. Cytotoxicity Assessment of QDs.....	132
5.4.2. Fluorescence Imaging of Cells.....	133

5.4.3. Cellular Uptake Mechanism of QDs.....	134
6 CONCLUSION AND PERSPECTIVES.....	
6.1 Conclusion.....	138
6.2. Perspective.....	140
REFERENCES.....	142
ANNEX A.....	159
ANNEX – CURRICULUM VITAE.....	162

Chapter 1

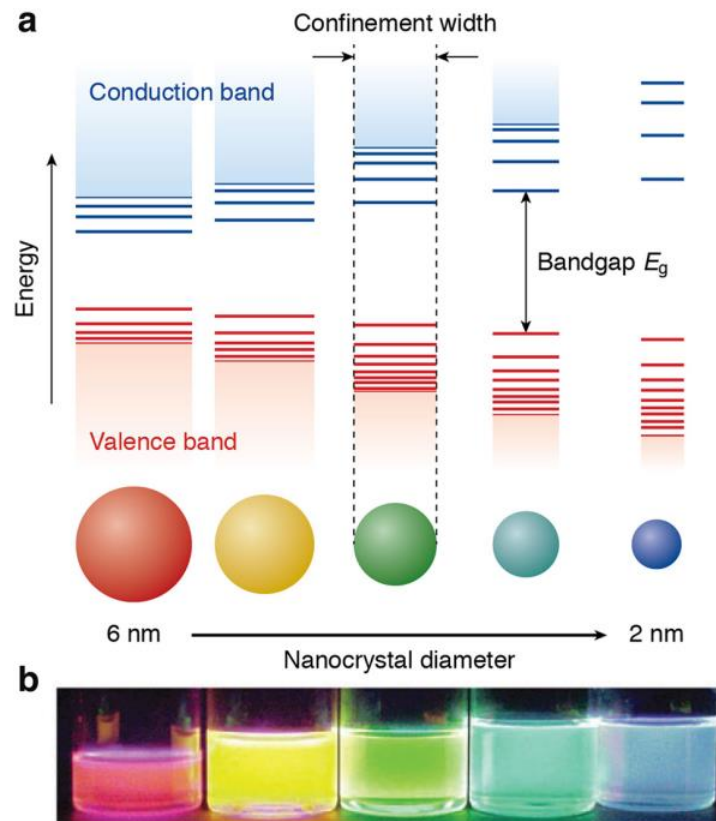
INTRODUCTION

1.1 Introduction to Semiconductor Quantum Dots (QDs)

Semiconductor QDs are tiny light-emitting particles (1-10 nm) made up of hundreds to thousands of atoms of groups, such as I-VI (e.g., Ag_2X QDs, X = S, Se, and Te), II-VI (e.g., ZnX and CdX QDs, X = S, Se, and Te), III-V (e.g., InAs, InP, InSb, GaAs, and GaSb QDs), IV-VI (e.g., PdX QDs, X = S, Se, and Te), and I-III-VI₂ (e.g., CuInS_2 and CuInSe_2 QDs) elements in the periodic table [4]–[8]. The photoluminescence properties of QDs stem from the radiative recombination of photogenerated charged carriers due to quantum confinement effect that is realized when the particle size is lesser than Bohr's exciton radius of that specific enclosure [9], [10]. In the bulk materials, the Bohr's exciton radius (defined as the average distance between VB holes and CB electrons) is comparatively much smaller than the dimensions of semiconducting materials, and the energy levels are continuous, however, while dwindling its size comparable to that of Bohr's radius, the energy levels are quantized. Under light exposure, an electron-hole pair (also known as *exciton*) is generated by exciting the electron to quantized band structure depending upon the transition probabilities. Subsequently, the exciton is relaxed, releasing the energy through various pathways: such as phonon-assisted relaxation, exciton radiative recombination, non-radiative decay due to surface states/traps, auger recombination, electronic energy transfer to the vibrational energy of ligands, etc. [10]–[12]. The optical properties of QDs are size-dependent (**Figure 1.1**); as the size of QDs decreases, the bandgap widens, and the energy levels are more quantized, resulting in a blue-shift of luminescence spectra. By modulating the size of QDs, the PL emission can be tuned over a wide wavelength range (400-4000 nm) across the ultraviolet, visible, and NIR regions [4]. Furthermore, the electron-hole wavefunctions can be modulated by shape, choice of component materials, and their dimensions. Due to their exceedingly unprecedented properties, QDs have excelled in the traditional organic dyes; they have superior photochemical stability, longer lifetime than those of fluorescent dyes, comparatively narrower emission bands.

Therefore, based on these unique photonic properties, the QDs have been extensively explored in the past decades and are being made consistent endeavors by the researchers to investigate for the integration of nanotechnology and biotechnology in a single platform, capable of performing multiple biomedical functions, ranging from diagnostic and therapy to bio-labeling and bioimaging.

Figure 1.1- Size-dependent bandgap engineering and discret energy states formation (a) and photographs of different colors of QDs [146].



1.2. Surface Modification and Types of QDs

1.2.1. Surface Passivation

Besides the quantum confinement effect, the optical and electronic properties of QDs are also dictated by the surface chemistry, because the surface atoms have lower coordination numbers compared to the interior atoms of QDs. Therefore, they lead to the formation of unsaturated dangling bonds that act as nonradiative de-excitation channels for the electronically charged carriers and significantly reduce the quantum yields (QYs) [13]. To overcome these undesirable effects, surface passivation is an effective strategy to eliminate the surface defects/traps and enhance the photoluminescence QYs, consequently, modulate the physicochemical properties of QDs. Moreover, it also imparts additional unprecedented features to QDs, such as, it protects them from the harsh environment that causes their oxidation and degradation and dictates the solubility, biocompatibility, and reproducibility applications of the QDs. Surface passivation by another

semiconductor with lower lattice mismatch and large bandgap (*e.g.*, ZnS, ZnSe, ZnTe, and CdS) is an excellent choice to maximally increase the confinement effect [14] and enhance the QYs.

1.2.2. Core-Shell QDs

In a core-shell system, the shell of larger bandgap materials is epitaxially grown to create a potential barrier and confine the exciton at the core-shell interface. To obtain better passivation, the lower lattice mismatch between the core and shell materials is considered an ideal choice to avoid the interfacial strain and misfit dislocations that can effectively change the optical properties of the core. The thickness of the shell also has a profound effect on the luminescent properties of the core. Larger thick shell generates non-radiative recombination sites that trap the photogenerated electron-hole pair and consequently reduce the QYs of QDs [12]. In core-shell heterostructures, the optoelectronic properties are dictated by the bandgap as well as the relative position of valence and conduction band of shell and offset energy to those of core QDs. Hence, by tailoring the shell thickness (number of layers), the photoluminescence properties and life-time can be designed and tuned, which are usually unachievable with discrete QDs of either core or shell material [15]. Based on the band edge alignment of conduction and valence band and charge delocalization in core-shell, the QDs have been classified into type-I, type-II, and quasi-type-I or type-II heterostructures [10]. It is noteworthy that in core-shell heterostructure, the lattice mismatch between two crystalline materials with different lattice parameters is a crucial factor to be specially considered during shell growth. A larger mismatch causes the stress at the interface, which is relieved by generating interfacial misfit dislocations that act as nonradiative centers and reduce the QYs.

1.2.3. Type-I and Inverse Type-I QDs

In type-I materials, the bandgap of the core is narrow and is sandwiched within shell materials of the wider bandgap. Additionally, the conduction band (CB) of the core is located lower than the CB of the shell, whereas the valence band (VB) of the core is higher than the VB of the shell (**Figure 1.2**). As a result, both charged carriers are completely cordoned off in core by the shell, and the bandgap emission is almost preserved or undergoes a small red-shift. Contrary, in the inverse type-I QDs, the bandgap of the shell is localized in the bandgap of core (**Figure 1.2**), and the electron hole-pair is confined entirely or partially in the shell [11]. Upon increasing the shell thickness, the hetero-nanostructure QDs bandgap alignment is switched from type-I to type-

II or quasi type-II structure, and the exciton is spatially segregated over the entire QDs [9], [16]. Contrary to type-I, the inverse type-I structure exhibit color-tunability by modulating the band gaps alignment [17], for instance, observed in ZnSe/InP/ZnS QDs.

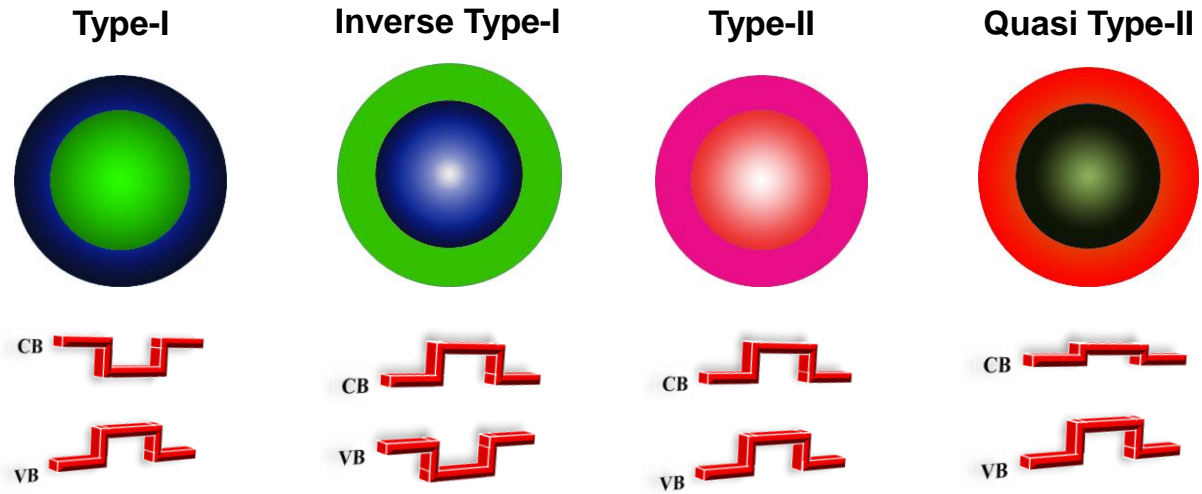
1.2.4. Type II QDs

In type-II band alignments, valence or conduction band of shell material is lied within the bandgap of core (forms staggered band-edge alignment) (**Figure 1.2**), resulting in the spatial segregation of electron-hole pair (indirect exciton) in QDs confined one charge carrier in the shell and the counterpart carrier in core regime. Charge carriers recombination occur across the core-shell interface, and consequently, the PL emission wavelength is smaller than that of the bandgap of comprising materials due to spatially indirect transitions [10], [11]. By tailoring the core size or relative positions of band gaps or shell thickness, the emission of type-II structure can be tuned over extended wavelength regime (Vis-NIR regions) that would otherwise not be obtainable with a single material [18]. However, the delocalization of one charge carrier reduces the spatial overlap of electron-hole pair and recombination dynamics, leading to extended single and multiple excitons lifetimes and lower QYs compared to that of the type-I nanostructure. The intrinsic charge separation characteristics provide a promising opportunity for various applications, such as lasing, photovoltaic cells, and nonlinear optics [19]. Some of the previously reported type-II heterostructures include ZnTe/ZnSe [20], CdSe/CdS/ZnS [41], CdTe/CdS [19], [21], CdTe/CdSe [19], [22], [23], CdSe/ZnTe [22], InP/CdS [16] etc.

1.2.5. Quasi-Type II QDs

In this nanostructure, the band alignment is flat, and the offset between conduction band edge states of core and shell is smaller (**Figure 1.2**). Therefore, one of the charge carriers (electron or hole) is localized in core or shell, and the other is spatially distributed over the entire QDs. Consequently, the leakage of one of the carriers into shell causes the lowering of radiative recombination of an exciton, resulting in red-shifted emission and longer lifetime, for example, observed in CdTe/CdSe[24] QDs.

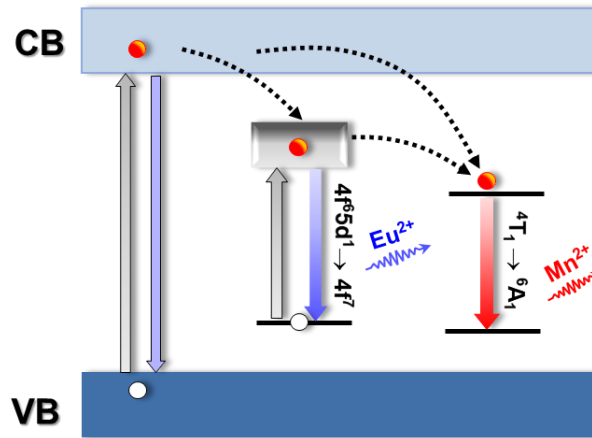
Figure 1.2 - Representative diagrams of bands alignment in core-shell quantum dots.



1.2.6. Dopant Impurities

The optoelectronic properties of QDs can be modulated by judicious incorporation of certain dopant impurities (**Figure 1.3**), such as lanthanide ions and transition metal ions into host NCs lattice. Most importantly, the dopants ions change the electronic states, impart unique optical, electrical, and magnetic properties to the QDs [25]. The incorporated dopant ions act either as electron donors or acceptors. The carrier-dopant exchange interactions (also known as sp-d exchange interactions) between the dopant's unpaired electrons and semiconductor band electrons give a unique magneto-optical or magneto-transport properties that are usually unachievable with un-doped QDs. Furthermore, the dopant ions present extended lifetime due to the forbidden intraconfigurational transitions than that of the bandgap or defect emission of host and provide propitious opportunity to evade the background fluorescence in biomedical applications. However, the incorporation of dopant ions to host is believed to be laborious; probably, it is due to the lattice mismatch and self-purification effect of the metal. To date, a number of studies have been published to explore the magnetic and optoelectronic potentialities of transition metal ions (e.g., Ag, Ti, Sn, Fe, Ni, Cr, Cu, Mn, Co) [14], [25]–[29] and lanthanide ions (e.g., Sm, Dy, Tm, Er, Eu, Tb, Gd, Yb) dopants [28], [30], [31] in semiconductor NCs.

Figure 1.3- Schematic illustration of partial energy transfer mechanism in E^{2+} and Mn^{2+} doped ZnSe QDs.



Grey arrow denotes photogenerated electron-hole pair (exciton), right blue arrow represents radiative recombination of exciton, black dashed arrows indicate energy transfer to the dopant impurities, second right black arrow denotes interconfigurational transition from $4f^7$ ground level to the $4f^65d^1$ excited state of the Eu^{2+} ion, blue and red arrows show the radiative decays for Eu^{2+} and Mn^{2+} ions, respectively.

1.3. Synthetic Approaches to QDs Preparation

Since the last two decades, many synthetic strategies have been orchestrated to fabricate the fluorescent quantum dots, mainly classified into aqueous and non-aqueous routes. This variation relies upon the nature, solubility, availability, and chemical properties of precursors. Both methods have their own merits and demerits. Non-aqueous synthetic route is usually performed at high temperatures to produce QDs of high quality, good crystallinity, and mono-dispersity with outstanding optical properties. However, the pitfalls of such a synthetic procedure are the water-insolubility of the obtained QDs, which is remarkably essential for their applications [32] in biological systems.

1.3.1. Organo-metals Method

This synthetic approach was first reported by Steigerwald and Brus in the early 1990s [33] and later on improved and developed to a more practical level by Murray et al. in 1993 [34] for the synthesis of high-quality cadmium chalcogenides QDs. The organo-metals approach employs an elevated temperature ($\sim 320^\circ\text{C}$), high-boiling solvent, and usually inert atmosphere. Principally, it consists of three components: *i*) precursors that act as source for NCs synthesis, *ii*) coordinating

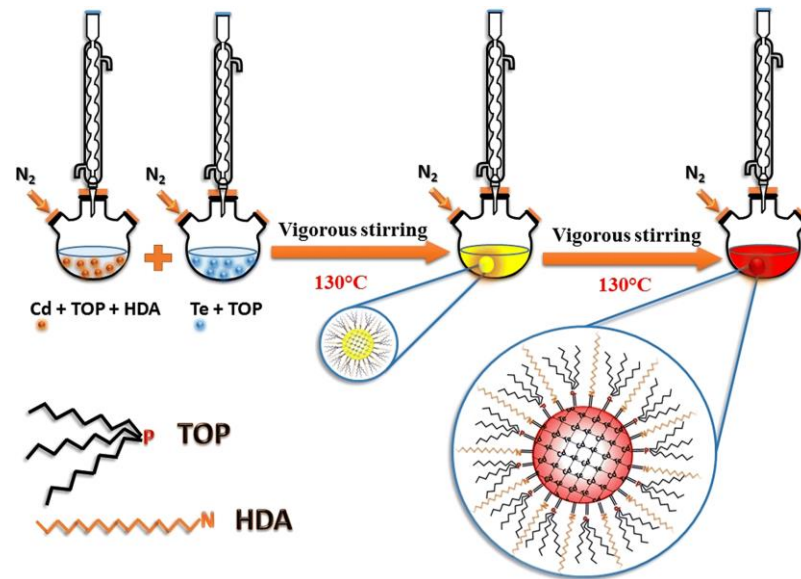
solvents or organic surfactants made up of tri-n-octylphosphine oxide (TOPO) [10], [13], [15], hexadecyl amine (HDA) [10], [13], tetradecyl-phosphonic acid (TDPA) [24], hexyl-phosphonic acid (HPA), octadecylamine (ODA) [19], oleic acid (OA) [19], oleyl amine (OLA) [16], [30], [35], 1-dodecanethiol (DDT) [17], and *iii*) noncoordinating solvents consisted of tri-n-octylphosphine *i.e.* tributyl-phosphine (TBP) [17], trihexyl-phosphine (THP), and trioctyl-phosphine (TOP) [5], [19], [22], [30], 1-Octadecene (ODE) [5], [17], [19], [20], [30], [35]. The coordinating solvent acts as a size-regulating and stabilizing agent that binds to the surface of particles and dictates the nucleation, crystals growth kinetics and morphology of QDs. It also prevents the NCs from aggregation, ensures their solubility, and protects from oxidation [36]. In this procedure (**Figure 1.4**), initially, organo-metals or metal-organic complexes (as metal source) are prepared by ligating naked metal ions to an appropriate ligand. They are reacted further to decompose or form a supersaturation of monomers which is followed by a burst of nucleation and crystal growth of monodisperse QDs [37]. It is important to quench the reaction at the right time, because, the relatively large size distribution of QDs is obtained when the concentration of monomers is depleted. This occurs due to the phenomena of dissolution of smaller particles and the continuous growth of larger particles called “Oswald ripening” [38].

Hot-injection procedure: In a typical approach, batch reactor (typically, three-necked round-bottom flask) containing organic solvents and stabilizers is evacuated to remove the volatile impurities. Organo-metals precursors and elemental chalcogens (S, Se, Te) are dissolved in an appropriate solvent (generally TOP and TBP) and added swiftly to a reaction mixture in an inert atmosphere, under vigorous magnetic stirring [39]. The temperature is usually adjusted to the desired value, and the reaction is allowed to proceed for a designated time. Certain reaction parameters must be systematically optimized to synthesize the high-quality QDs [13]: *i*) relative concentration of both coordinating and non-coordinating solvents, *ii*) injection condition, *iii*) reaction temperature, and time, *iv*) precursors concentration and reactivity and *v*) kinetics of nucleation and growth processes.

One pot non-injection: it is an alternate approach to evade the hot-injection complexities and produce high-quality monodisperse QDs relatively at a lower temperature. In such a system, all the reagents or single-source precursors are loaded in a three-necked flask and subsequently heated to obtain the QDs [40], [41]. Multiple types of semiconductor nanorods, nano-tetrapods, nanowires, nanotubes, nanosheets have been previously reported [42] by the organo-metals synthesis method.

The organo-metals approach produces QDs of high quality, narrow size distribution, outstanding crystallinity, superior optical properties, *i.e.*, high PL-QYs (~97%) [43]. On the other hand, it also carries some intrinsic disadvantages in terms of environment-unfriendly, hazardous chemical production, cost-effectiveness, low batch to batch reproducibility, and non-aqueous solubility, that limit their applications in biological and biomedical fields [6].

Figure 1.4 - Schematic representation of CdTe QDs preparation *via* organo-metals procedure [1].



1.3.2. Aqueous Rout to QDs Synthesis

The QDs prepared by the organo-metals method are usually not aqueous soluble, owing to the hydrophobic nature of organic ligands. Therefore, they cannot be directly applied in biological and clinical applications. To overcome this barrier, post-treatment procedures, *e.g.*, hydrophilic ligand exchange, polymer encapsulation, silica deposition, or phospholipid micelles formation, are applied. However, in this method, the optical and physicochemical properties of QDs are adversely affected [44]–[46]. Aqueous synthesis route is an effective alternative approach to prepare water-soluble and biocompatible QDs. This strategy is modeled on the basis of heating at reflux the ionic precursors (generally, metal acetate, nitrate, sulfate, chlorate or perchlorate) with S²⁻ precursor (NaS₂) in an inert ambience and the presence of different types of stabilizing agents, such as, 1-thioglycerol [47], glutathione (GSH) [7], [45], 3-mercaptopropionic acid (3-MPA) [21], [48], mercaptoacetic acid (MAA), mercaptosuccinic acid (MSA)[48], dithiothreitol (DTT), thioglycolic acid (TGA) [23], [48], thiolactic acid (TLA) [48], 2-mercaptoethylamine (2-MEA), cysteine [44],

2-mercaptoethanol [47], 1-mercapto-2-propanol, 2-dimercapto-3-propanol [6], dihydrolipidic acid (DHLA) etc [49]. The photoluminescence QYs of the QDs prepared by this approach is strictly relied upon varying the experimental conditions, such as pH of the medium, precursor concentration, temperature, and refluxing time [50], [51].

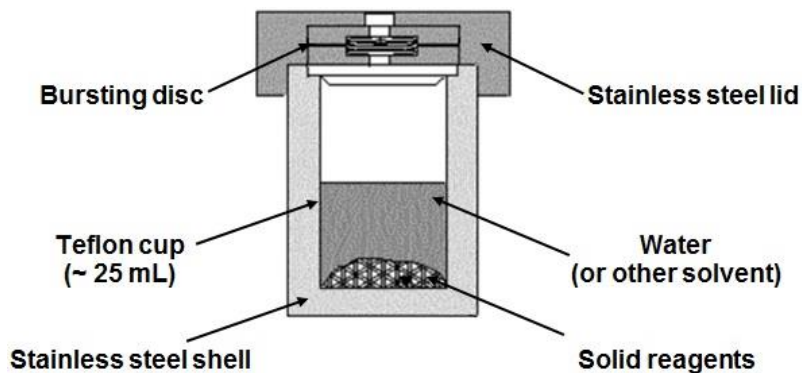
The aqueous medium approach exhibits various advantages, such as it is reproducible, more versatile, cost-effective, suitable for large scale production, economically favorable, and eco-friendly. On the other hand, the QDs prepared by aqueous approach have also some intrinsic limitations. They are poorly protected by weakly-bound thiol-containing ligands; therefore, they are prone to degradation, aggregation, oxidation, and decomposition [52]. Besides, the QDs prepared by this method show broad emission and low QYs.

1.3.3. Hydrothermal/Solvothermal Approach to QDs Synthesis

Hydrothermal and solvothermal approaches are similar synthetic routes to synthesize colloidal QDs except that the latter is performed in non-aqueous phase medium such as ethanol, ethylenediamine, etc. The hydrothermal reaction is performed in an aqueous medium containing metal precursors (cation and anion species) and amines or thiol-carrying stabilizers (sometimes also act as sulfur source) in a tightly sealed Teflon-lined stainless steel autoclave (**Figure 1.5**) under an autogenous pressure and at temperature ~ 200 °C [14], [53], [54]. The paramount importance of the system is to design and fabricate color-tunable QDs, which are relied upon certain experimental conditions, such as precursor's concentration, pH, temperature, and duration of the reaction. To date, the syntheses of various fluorescence QDs have been reported by this method such as CuInS₂ [55], ZnS [54], ZnSe:Mn²⁺ [56], CdTeS [57], CdS [58] etc.

In an atypical approach, the solution of precursor materials is prepared in deionized water, and its pH is adjusted to a particular value. The solution is loaded in a Teflon-lined stainless-steel autoclave and heated to specific reaction temperature, to grow the nanocrystals, for a designated time depending upon the experimental conditions. There are various advantages of the synthetic route: *i*) it is environmentally friendly and cheap, *ii*) the prepared QDs are water-soluble, biocompatible and reproducible, and *iii*) they have lower lattice defects [14]. However, unlike the organic solvents approaches, the QDs prepared by this method have relatively low QYs, large size distribution, and lower crystallinity [38].

Figure 1.5 - A schematic of a Teflons[®] lined stainless steel autoclave typically used in the laboratory for hydrothermal/solvothermal syntheses [2].



1.3.4. Biosynthesis of QDs

This approach employs the inherent enzymatic characteristics of microorganisms such as fungi, yeast, virus, and bacteria to synthesize the fluorescence QDs (especially metal sulfides) [59], [60]. The living biological system usually recruits two types of molecular machinery to produce the NCs: *i*) in intracellular synthesis, the precursor ions are taken up by cells and subsequently converted to QDs by the intracellular enzymatic activities, and *ii*) in extracellular synthesis, the QDs are prepared by the biochemical reactions of enzymes at the cell surface or by enzymes secreted in the biological milieu [39], [61]. The representative QDs previously synthesized by a biological approach include CdS (*Halobacillus* sp) [59], CdTe (*Escherichia coli* or *Saccharomyces cerevisiae*) [61], [62].

The biosynthesis approach has some distinctive invincible features when compared to the conventional synthesis approaches: *i*) the reaction is performed at the moderate reaction conditions, *ii*) the QDs are produced by the intrinsic enzymatic reactivities and intracellular metal redox and stabilizing agents (amino acid, peptides, proteins, nucleotides, and phosphorylated molecules) in the biological milieu, and *iii*) the physicochemical characteristics of QDs can be modulated *via* the genetic engineering of physiologic factors and intracellular redox conditions [39], [63]. Biosynthesis is accredited to be eco-friendly, non-toxic, and compatible for pharmaceutical and medicinal applications. This method has some inherent demerits, such as the QDs are polydisperse, time-consuming, and production rate is slow.

1.3.5. Surface Chemistry of QDs

The strategy is usually employed to transform the non-aqueous soluble QDs into aqueous soluble and biocompatible one, well dispersible under physiological conditions such as pH 7.4, 37 °C in the presence of proteins, salts and other biomolecules for use in biological and biomedical purposes. Principally, the stabilizing layers of native surfactants (e.g., alkyl phosphine, alkyl phosphine oxide, aliphatic amines and aliphatic carboxylic acids etc.,) are replaced by bifunctional stabilizing agents, containing hydrophilic moiety (amine, carboxyl and thiol) and metal element-binding group, such as 1-thioglycerol [47], GSH [45], 3-MPA [21], [64], MAA [65], DTT [65], thioglycolic acid (TGA) [64], [66], thiolactic acid (TLA)[66], 2-MEA[7], cysteine[44], 2-mercaptoethanol [47], thiomalic acid (TMA) [66], mercaptoundecanoic acid (MUA) [65], 2,3-dimercaptosuccinic acid (DMSA) [66], and DHLA [65] through ligand exchange reaction [49]. The soft acidic group (usually thiol) is usually linked to the surface of QDs, and the hydrophilic groups (carboxylic or amine) interact with the bulk water molecules [67]. To perform the ligand exchange reaction, various chemical reducing reagents, e.g., sodium borohydride, tetramethylammonium hydroxide, and sodium hydroxide solution (w/v) have been previously used [63].

There are various advantages of direct synthesis in an aqueous medium, for instance, it is safe, cheap, using less toxic organic reagents and lower temperature (<100 °C). Besides, the QDs are water-soluble and biocompatible for biological applications. However, there are some shortcomings of this approach: it alters the physicochemical nature of QDs and decreases the QYs, and the thin surface ligands are susceptible to local conditions such as pH, temperature, and concentration [7]. The thiol ligand may form disulfides and consequently dissociate from the QDs that render them to destabilize and precipitate out of water [68]. Other techniques, such as encapsulation within block copolymers shell, liposomes and phospholipids micelles, fatty acids, dendrimers, amphiphilic polysaccharides, phytochelatin-peptides histidine-rich proteins, oligomeric phosphine coating or addition of silica shell, are also performed to make the QDs water soluble [7].

1.4. Biomedical Applications of QDs

In the past decades, nano-sized materials have successfully integrated multi-structural, multi-disciplinary and multi-dimensional features of nanotechnology with biology and medicine

into a single nano-formulation employed in various applications: biomolecules-delivery, bio-labeling, bio-detection [69], bio-tracking, bio-imaging [7], [70], and theranostics nano-medicine [4], [5], [71], [72]. Nanomaterials have high surface/volume ratio, high loading capability, and facile surface modification characteristics; therefore, they can be conjugated to a variety of biomolecules such as nucleic acids, antibodies, proteins, oligonucleotides, etc., to direct them to the site of interest and achieve maximum concentration *in vitro* and *in vivo* study. Particularly, semiconductor quantum dots (QDs) have been more explored due to their unique optoelectronic properties, size-dependent color-tunability, and high physicochemical stability. QDs have superior photo-physical and photochemical properties than conventional organic dyes and fluorophores; therefore, they are considered more appropriate to investigate for more advanced purposes[14].

1.4.1. QDs Induced Toxicity

Multiple physicochemical characteristics of QDs have been reported to induce toxicity *in vivo* and *in vitro*: such as QDs dose, size, aggregation, morphology, surface chemistry, redox activity, chemical composition, photochemical stability, cell type, and time of incubation. Furthermore, under physiological conditions (pH, redox potential, and enzymatic cleavage), QDs are prone to degradation, leading to the production of heavy metal ions (e.g., Cd^{2+} , Hg^{2+} , and Pb^{2+}) [69], [73]. The QDs dots induce several adverse effects to cells: they change the functional, morphological, and biochemical coherency of cells, and damage to fundamental cell organelles such as lysosomal rupture, mitochondria dysfunction, disturbance of endoplasmic reticulum, and nuclei. Moreover, the QDs cause protein aggregation, damage to the plasma membrane, fibrils formation, enhanced autosome formation, inhibition of DNA repairing, eventually leading to cell death [8], [74]. Among them, Cd and Pb-based chalcogenides have been explored for biomedical purposes; however, they have been indicted toxic because of leaching out Cd^{2+} and Pb^{2+} ions that induce ROS (such as singlet $^1\text{O}_2$, hydrogen peroxide, and hydroxyl radical) production which oxidize cellular macromolecules, e.g., lipids, proteins, nucleic acids, and DNA, leading to cell death [7], [69]. Additionally, Pb deregulates the functions of the hepatic, renal, hematopoietic, and central nervous system.

To evade/reduce toxicity, various approaches have been alternatively investigated: preparation of Cd free QDs (e.g., InAs, InP, GaAs, GaP, ZnSe/ZnS [75], MoS_2 [70], $\text{CuInS}_2/\text{ZnS}$

[5], AgInS₂ [7], Ag₂S [4]) and lanthanide/transition metal ions doped QDs [22]–[28], formation of nontoxic shell, and encapsulation in to polymers.

1.4.2. Biosensing

Quantum dots have the intrinsic ability to transfer energy to lower energy acceptor molecules *via* fluorescence resonance energy transfer (FRET), leading to a downfall in emission intensity of QDs. The acceptor molecule can either be fluorophores and concomitantly its emission intensity is enhanced or quenchers (non-fluorescent energy acceptor molecule) that extinguish the signal [76]. Due to the inherent features of size-dependent color-tunability, QDs can transfer energy to acceptor molecules in broad regions of UV-visible and NIR radiations. Additionally, QDs carry unique physicochemical and optoelectronic properties compared to the organic dyes and protein fluorophores and are more resistant to biodegradation, photobleaching, and radical formation. Therefore, the integration of QDs with suitable acceptor molecules provide propitious opportunity to develop the bio-analytical devices for the detection and monitoring of biological events. QDs-based FRET technology has been used to detect and monitor the conformational changes, interactions, and dynamics of biomolecules such as antibodies, antigens, enzymes, nucleic acids, pathogens, DNA, proteins [77]–[79], etc. Quantum dots act as an effective FRET energy acceptor in combination with down conversion lanthanides (particularly Eu and Tb) and upconversion (Yb (III), Er (III), and Tm (III)), leading to an enhanced emission intensity and longer photoluminescent lifetime that enable the bio-analytical probes several times more efficient [76]. Unlike FRET, by generating the excitation state through chemical reactions, the donor molecules transfer nonradioactive energy via chemiluminescence and bioluminescence resonance energy transfer (CRET and BRET, respectively) to QDs. FRET-and BRET-based QDs biosensor can be used to diagnose several diseases by measuring the upregulated expression and activity level of proteases.

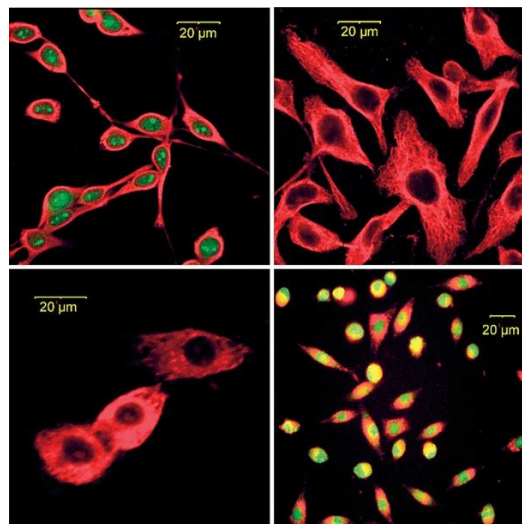
1.4.3. Bioimaging

Bioimaging is the primary non-invasive technique (**Figure 1.6**) for the early diagnosis of complex diseases and obtaining detailed information on qualitative and quantitative changes in tissues and organs. Inspired by the invincible properties, scientists have extensively unraveled the QDs to promote for various types of *in vitro* and *in vivo* biological imaging: targeted cellular imaging, multicolor imaging, multimodal imaging, multiphoton imaging, and deep tissues imaging

of multiple biological specimens (e.g., stem cells, tissues, cancer cells, tumor neovasculature, bacteria, virus, etc.) [63], [73]. Quantum dots provide auspicious opportunity to surface functionalization, logistics loading, and consolidating capability of multiple features; therefore, by conjugating to specific ligands (such as antibodies, peptides, proteins, and aptamers), they can be enabled to guide to an area of interest and perform multiples studies (simultaneous visualization and qualitative and quantitative analyses) at extracellular, intracellular, and subcellular levels such as membrane dynamics, extracellular receptors, intracellular cargo transport, and cell development [8], [73]. Incorporation of magnetic impurities (Mn, Ni, Gd) into QDs, chemical conjugation, and co-encapsulation of QDs and magnetic nanomaterials in a matrix has opened new avenues to researchers to integrate the optical and other imaging modalities e.g., computed tomography, positron emission tomography, and magnetic resonance imaging in a single entity for the acquisition of detailed information of subcellular, tissues and organs, and anatomical structures at high spatial resolution.

In deep tissue analyses, penetration of radiations (in the visible region) to a specific site is hampered by severe tissue scattering, and light absorption by various biomolecules (e.g., proteins, DNA, NADH, and FAD) and the incoming signal is masked by endogenous autofluorescence. Quantum dots, due to size-dependent color tunability up to NIR regions (NIR-I $\lambda_{em} = 650-1000$ nm) and (NIR-II $\lambda_{em} = 1000-1700$ nm) windows, can belittle these restrictions and enable the deep-tissue mapping and imaging of tumor cells, tumor vasculature, and lymph nodes [80], [81].

Figure 1.6 – Fluorescence images of cells stained with QDs [147].



1.5. Factors Affecting the Cellular Uptake of Particles

The understanding of nanoparticles-cellular behaviors is the grass root to develop new generation bionanoprobe and enhance diagnostics and theranostics efficiency. The nature of cells and physicochemical characteristics of cargos strongly affect the fate of cellular uptake, intracellular transporting, subcellular localization, excretion processes, and cellular functions such as proliferation, apoptosis, and cytoskeletal formation [82]. The morphology, surface chemistry, and chemical composition of particles are the key factors to dictate the dynamic of NP-cell interaction and adhesion, the kinetic processes initiated by the heterogeneous nano-bio interfaces, invagination, and the tension created against the enwrapped particles by cell membrane [82]–[84].

The size of particles is the critical determinant of the endocytic pathway and rate of uptake. It affects the cellular adhesion, membrane stretching, membrane bending energy, and the wrapping time of particles. Although it is not completely clear to predict specific pathway for the particular size of particles, yet it has been hypothesized that particles can enter cells *via* routes consistent to its threshold radius: particles of 100-200 nm size are internalized by clathrin-mediated endocytosis [85], [86] and 60-80 nm by caveolin-mediated endocytosis [87], [88], 40-50 nm by clathrin and caveolae-independent endocytosis [89], whereas larger particles and macromolecules (>0.5 nm) are engulfed by phagocytosis [78]–[80]. The particles ranging in the size of 30-50 nm have been reported to interact efficiently with cells and subsequently internalize compare to the smaller particles (15-30 nm) and larger particles (70-240 nm). Surface charge impinges a significant influence on particles-cellular interactions and uptake. The endocytosis is initiated at the interfacial forces such as electrostatic interactions, van der Waals forces, hydration, and hydrophobic effects where the positively charged particles are more efficiently internalized due to nanoparticles-cell electrostatic interactions rather than negatively charged and neutral particles [84]. The shape of particles also affects cellular uptake patterns. Rod-like particles have been reported to internalize quickly compared to spherical particles and the particles of irregular shapes.

1.6. Uptake Mechanism of Nanoparticles

The understanding of cellular recognition and interaction, uptake pathway, intracellular localization, and the subcellular fate of substances is of great importance to improve the diagnostic accuracy, targeted delivery and therapeutic efficiency of payloads and avoid the off-site problems [90]. Intracellular delivery of specific payload can be embodied by four different mechanisms: 1)

non-endocytosis *via* passive mechanism transport, 2) endocytosis pathway, 3) mechanical treatment-mediated transportation i.e., electroporation, sonoporation, and microinjection, and 4) chemical treatment-facilitated transfection, e.g., peptides translocation [8], [63], [73], [91]. Based upon the physicochemical characteristics of cargos, the cellular endocytosis is executed by two different major mechanisms: 1) phagocytosis, which engulfs large particles with a size of $>0.5 \mu\text{m}$ and microorganisms (bacteria and virus) and cellular debris and 2) pinocytosis or cell drinking process which uptakes fluid and particles of size $<0.5 \mu\text{m}$ within small vesicular structures. However, it's noteworthy that exact pathway for a certain size of particles is still debatable, it is because that the pathway is strongly governed by the physicochemical characteristics such as surface chemistry, chemical composition, and morphology of particles and geometry of cell surface-and particles interaction [82], [90], [92]–[94].

1.6.1. Phagocytosis

Phagocytosis is the intrinsic ability of certain types of cells named as professional phagocytes encompassing monocytes, macrophages, dendritic cells, and nucleophiles. To some extent, another type of cells referred to as para-and nonprofessional phagocytes also exhibit phagocytic activities, but to a lower extent, these include epithelial cells, fibroblast cells, natural killer cells, and the inflammatory mediators producing cells (basophile, eosinophil and mast cells) [88], [93], [95]. Their primary function is the clearance of pathogens (bacteria, viruses, and yeast), hazardous materials, the remnant of dead cells, and arterial deposits of fat. Phagocytosis is usually initiated by cell-surface recognition and proceeds *via* interaction of cell surface receptors and ligands-presented by materials or *via* electrostatic interaction (i.e., ionic, electrostatic, van der Waal forces) between the cells and materials surface [86], [95]. The major receptors involved in the process encompass Fc receptors (FcR) and complement receptors (CR) and other receptors, i.e., scavenger receptors and mannose/fructose receptors to some extent [86], [88], [92]. Following the cell-particle interaction, cascade of signals is generated that induces the rearrangement and assembly of actin and formation of pseudopodial vesiculations, enveloping the materials in a zipper-like fashion (**Figure 1.7**). The materials are subsequently engulfed and internalized in a vesicle known as phagosome, which is further trafficked to lysosomes, forming acidified enzyme-rich (i.e., hydrolases and cathepsins) phagolysosomes [92], [96].

1.6.2. Pinocytosis

It can be further subcategorized into macropinocytosis, receptor-mediated uptake (clathrin- and caveolae-mediated endocytosis), and clathrin- and caveolae-independent endocytosis. The endocytic pathway proceeds in three different stages: 1) the plasma membrane is adhered to a substance and undergoes invagination to form vesicles, 2) subsequently, the budded vesicles are pinched off the membrane and sequestered to the cytosol. The internalized cargos are either recycled back to the plasma membrane or transported and addressed to various compartments. The clathrin- and caveolae-mediated pathway share similar molecular machinery such as actin, epsin, cortactin, intersectin, dynamin, and cholesterol, however, they differ in

Clathrin-mediated endocytosis (CME): clathrin-receptor mediated endocytosis is considered to be a most physiologically important pathway in eukaryotic cells involved in the nutrients uptake, internalization of plasma membrane constituents and macromolecules, internal trafficking, intracellular communication, and membrane recycling [86], [92]. CME is usually executed in the clathrin-enriched region of cell membranes that can internalize materials in volume proportional to the internal size of clathrin-coated vesicles that ranges 100-200 nm in diameter [85], [86]. The process is initiated at particle-cell interaction mediated by receptors or nonspecific interaction referred to as receptor-independent CME *via* hydrophobic and electrostatic interactions. In CME, the cargo is enwrapped along with trans-membrane receptors in clathrin-coated pits induced *via* cell membrane curvature driven by polymerization of clathrin and co-assembly of adapter and accessory proteins (e.g., amphiphysin, epsin, and SNX9) into complex architecture. Depending upon the type of cells, several receptors (epidermal growth factor receptors, low-density lipoprotein receptors, transferrin receptors, and β_2 adrenergic receptors) participate in the clathrin-mediated endocytosis [91], [92]. Additionally, ~150 proteins are involved in the clathrin nucleation, architecture of clathrin-coated vesicles, invagination, and regulation of the CME process [86], [88], [92]. The pit is deeply invaginated into cells and pinched off the cell membrane by GTPase enzyme dynamin forming clathrin-coated vesicle, which is fused with endosome (**Figure 1.7**) and then trafficked to lysosomes *via* endolysosome pathway [97]. The clathrin protein, some receptors, and ligands are dissociated and recycled back to the cell membrane. The pathway is exploited by several types of viral and bacterial pathogens and drug delivery to get entry to cells [86], [92].

Caveolae-mediated endocytosis (CvME): CvME is the predominant pathway in most of the cells, such as endothelial cells, smooth muscle cells, adipocytes, and fibroblast cells but lacked in neurons

and leukocytes [88], [95]. Following the cargo-cell interaction, CvME undertakes characteristic flask-shaped membrane invagination of 60-80 nm in diameter [87], [88], [98] at the distal end which is stabilized by caveolin, a dimeric protein, that binds to membrane cholesterol-rich lipid-raft domain. Caveolae are also enriched in some glycosphingolipids and sphingomyelin relative to the cell membrane. Another protein named cavin is known to aid caveolae formation and functional regulation with caveolin [86], [92]. The vesicle is cut off the membrane by dynamin, a GTPase enzyme, and is trafficked to endosomes or caveosomes (**Figure 1.7**). The endosomes are either recycled back to the membrane for reuse or fused with lysosomes, leading to the degradation of cargos in the acidic environment. The caveosomes (having neutral pH) can escape the acidic environment of lysosomes and transport the payloads to the Golgi apparatus and endoplasmic reticulum. Therefore this pathway is usually exploited by pathogens (virus and bacteria) to evade the lysosomal degradation [88], [95]. The pathway plays a physiologically crucial role in endocytosis, transcytosis, signal transduction, regulation of membrane proteins, and cholesterol homeostasis [88], [95]. It also provides propitious opportunity to deliver the theranostics and degradable materials such as genes and protein, avoiding the acidic environment of lysosomes.

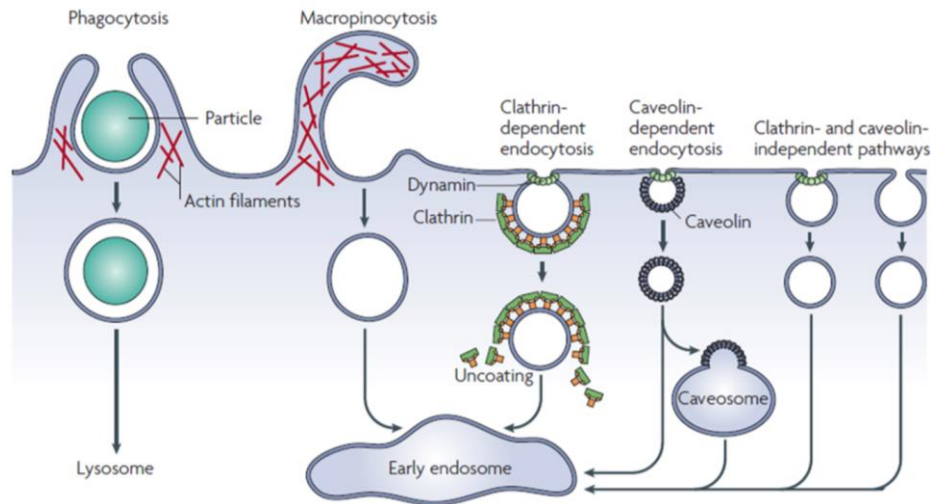
Clathrin-independent pathway: The pathway doesn't use a clathrin coat for vesicle formation and is a dynamin-dependent and-independent (**Figure 1.7**), sometimes regulated by ligands and membrane lipids. The pathway involves in cell lacking clathrin. It is utilized by cell-surface proteins and bacterial toxins to enter the cells and participate in the modulation of intercellular signaling, cellular polarization, cellular spreading, and plasma membrane repair [3], [99].

Caveolae-independent pathway: Caveolae-independent endocytosis is a fast cholesterol-dependent pathway devoid of dynamin II that uptake the cargos and transport *via* non-endosomal cytosolic organelles to the endoplasmic reticulum. The pathway involves the uptake of extracellular fluid, growth hormones, interleukin-2, and glycosylphosphatidylinositol [3].

Macropinocytosis: macropinocytosis is a unique actin-driven pathway specialized to internalize extracellular fluid, macromolecules, large particles, and pathogens *via* relatively large endocytic vesicles (0.2-5 μm) known as macropinosomes [88], [92], [95]. The pathway accompanies Rho-family GTPases that induces signaling cascades to generate membrane protrusion/ruffles to enwrap cargos. However, unlike phagocytosis, the protrusion is collapsed on the cell membrane to form macropinosomes, entrapping the extracellular cargos (**Figure 1.7**). The macropinosomes are either recycled back to the cell surface or transported to lysosomes where they are exposed to enzymatic

degradation. Macropinocytosis plays a physiologically crucial role in immune surveillance. In immature dendritic, it serves in antigen presentation and down-regulation of activated signaling. In therapy, it is being exploited to deliver proteins, nucleic acid, and liposomes.

Figure 1.7 - Schematic representation of endocytic pathways utilized by cells in the uptake of nanocrystals [3].



Chapter 2

OBJECTIVES

2 OBJECTIVES

The major aims and objective of this study were the:

- Designing and development of biocompatible and photoluminescent nanoprobe for biomedical applications.
- Synthesis and characterization of highly photoluminescence and photochemically and colloidally stable QDs.
- Assessment of QDs effect on cell viability.
- Elucidation of cellular uptake mechanism.
- Qualitative and quantitative detection of QDs in cells.
- Determination of sensitivity (e.g. minimum time or QDs concentration required for signal generation and detection).

Chapter 3

EXPERIMENTAL SECTION

3 Experimental Part A

3.1. Reagents and solvents

All the reagents and solvents (summarized in **Table 1**) were purchased commercially and used without further treatment or modification. Europium chloride hexahydrate ($\text{EuCl}_3 \cdot 6\text{H}_2\text{O}$) was prepared from its respective oxide by treatment with concentrated hydrochloric acid according to the previously reported method [100].

Table 1. Reagents and solvents used in the syntheses of aqueous soluble quantum dots.

Reagents	Company
Selenium powder (Se \geq 99.5%)	Sigma-Aldrich
3-Mercaptopropionic acid (3-MPA \geq 99%)	Sigma-Aldrich
Oleylamine (OLA \geq 70%)	Sigma-Aldrich
1-Octadecene (ODE \geq 90%)	Sigma-Aldrich
1-Dodecanthaiol (DDT \geq 98%)	Sigma-Aldrich
Manganese chloride ($\text{MnCl}_2 \geq 99\%$)	Sigma-Aldrich
Sodium hydroxide (NaOH \geq 97%)	Vetec
Hydrochloric acid (HCl \geq 37%)	Vetec
Oleic acid (OA)	Synth
Cadmium acetate dihydrate ($\text{Cd}(\text{CH}_3\text{CO}_2)_2 \cdot 2\text{H}_2\text{O} \geq 99\%$)	Synth
Chloroform	Synth
Hydrogen peroxide ($\text{H}_2\text{O}_2 \geq 29\%$)	Synth
Ethyl alcohol	Synth
Acetone	Synth
Zinc acetate dihydrate ($\text{Zn}(\text{CH}_3\text{CO}_2)_2 \cdot 2\text{H}_2\text{O} \geq 98\%$)	Alfa Aesar
Zinc oxide ($\text{ZnO} \geq 99\%$)	Merk
Milli-Q water	
Europium oxide hexahydrate ($\text{Eu}_2\text{O}_3 \geq 99.99\%$)	Rhodia

3.2. Preparation of ZnSe: $x\text{Mn}^{2+}$ ($x = 5, 10, \text{ and } 15 \text{ mol\%}$) QDs

ZnSe: $x\text{Mn}^{2+}$ ($x = 5, 10, \text{ and } 15 \text{ mol\%}$) QDs were synthesized in noncoordinating ODE and coordinating solvents/stabilizing agents OA/OLA/DDT at high temperature (280 °C) under continuous nitrogen (N_2) flow and vigorous magnetic stirring (**Figure 3.1**) by modified method, as previously reported in the literature [101].

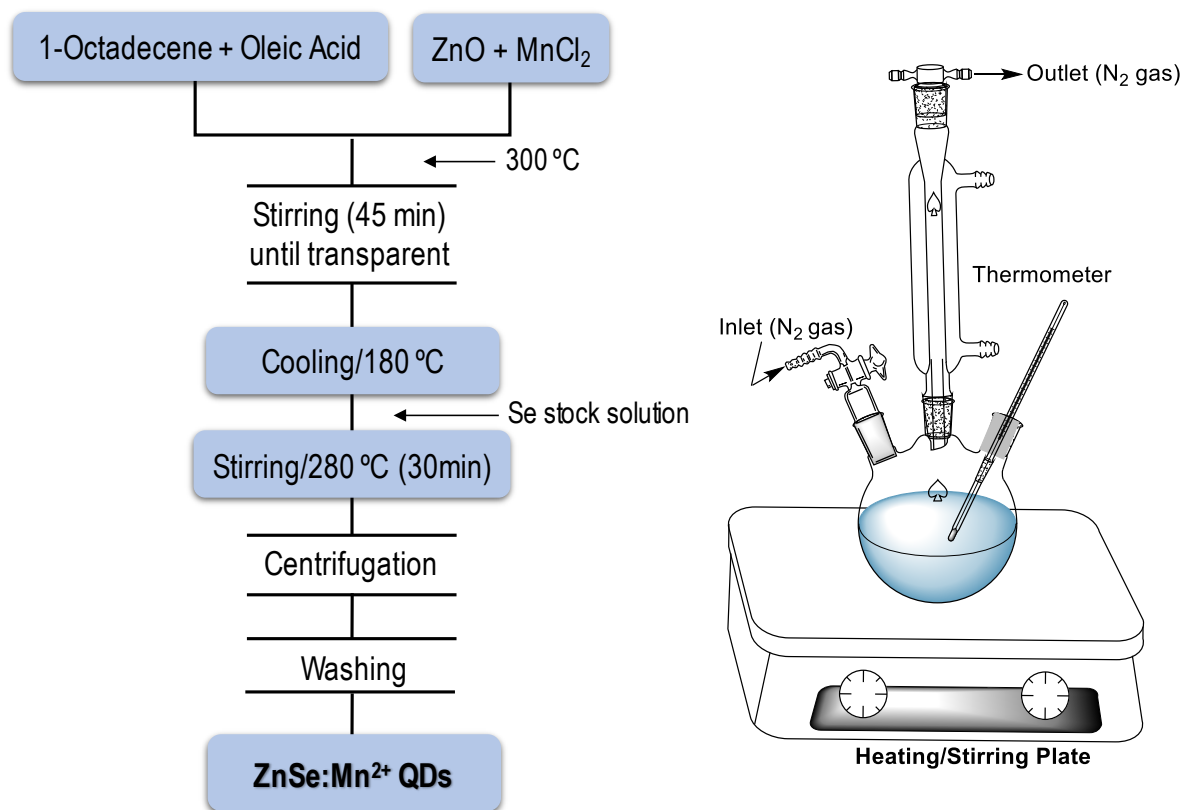
Synthesis of Metal-oleate: Typically, 77.31 mg of ZnO (0.95 mmol) and 6.29 mg of MnCl_2 (0.05 mmol) were mixed in ODE (10 mL) and OA (5 mL), then loaded in the three-necked flask. The mixture was de-aerated and dehumidified by heating at 120 °C for 30 min, under continuous N_2 flow and magnetic stirring. Subsequently, the temperature was elevated to 300 °C and maintained unless a slightly yellowish and transparent solution of Zn-oleate and Mn-oleate was formed, which was used as *in situ* precursors for ZnSe: Mn^{2+} QDs preparation.

Se stock solution (0.33 mM): This solution was prepared by mixing 78.96 mg of Se powder (1 mmol) in OLA (1 mL) and DDT (2 mL) mixture under magnetic stirring at ambient temperature for 1 hour.

3.2.1. Synthesis of ZnSe: Mn^{2+} QDs

The Mn^{2+} doped ZnSe QDs were synthesized at high temperature through the organometals method, using the above metal-oleate and selenium stock solution as precursors. In a typical procedure, the temperature of the metal-oleate solution was adjusted to 180 °C and quickly injected the freshly prepared Se solution (0.33 mM). The reaction mixture was heated to 280 °C and let the reaction for 30 min to achieve maximum nucleation and crystal growth of ZnSe: Mn^{2+} (5 mol%) QDs. Eventually, the solution was cooled to 70 °C and injected two times the volume of ethanol to precipitate the OA/OLA/DDT capped ZnSe: Mn^{2+} (5 mol%) QDs. The product was centrifuged and purified by washing several times with ethanol to remove the unreacted precursors and byproducts. The other ZnSe: $x\text{Mn}^{2+}$ ($x = 10 \text{ and } 15 \text{ mol\%}$) QDs were also prepared by the same procedure, using the stoichiometric concentrations of the dopant ions.

Figure 3.1 - Flow chart diagram (left) and the representative reaction assembly (right) for the ZnSe:xMn^{2+} ($x = 5, 10,$ and 15 mol%) QDs synthesis *via* organo-metals approach.



3.3. Preparation of ZnSe: $x\text{Eu}^{2+}/y\text{Mn}^{2+}$ and ZnSe: $x\text{Eu}^{2+}/y\text{Mn}^{2+}$ @ZnS QDs

Two-step approach was adopted to prepare the un-passivated ZnSe: $x\text{Eu}^{2+}/y\text{Mn}^{2+}$ ($x = 4, 8,$ and $12; y = 12$ mol%) QDs and ZnS passivated ZnSe: $x\text{Eu}^{2+},y\text{Mn}^{2+}$ ($x, y = 12$ mol%) and ZnSe: Eu^{2+} (4 mol%) core-shell QDs (**Figure 3.2**). Initially, ZnSe: $x\text{Eu}^{2+},y\text{Mn}^{2+}$ ($x, y = 12$ mol%) and ZnSe: Eu^{2+} (4 mol%) QDs were synthesized and purified, then, they were epitaxially passivated by ZnS in a separate reaction. The synthesis was performed *via* organo-metals synthetic approach in non-coordinating solvent ODE and coordinating solvent/stabilizing agent OA, as described below.

Synthesis of Metal-oleate: In a typical approach, the three-necked flask containing 22.54 mg of ZnO (0.277 mmol), 4.5 mg of $\text{EuCl}_3 \cdot 6\text{H}_2\text{O}$ (0.012 mmol), and 4.98 mg of MnCl_2 (0.039 mmol) in a mixture of ODE (10 mL), OA (5 mL) and DDT (2 mL) was magnetically stirred at 120°C under consistent N_2 flow for 30 min to deoxygenate and dehumidify the reaction mixture. Subsequently, the temperature was elevated to 220°C and maintained for 30 min to obtain a slightly yellowish and transparent solution of metal-oleate. Interestingly, the meantime, Eu^{3+} was reduced to Eu^{2+} ion during the syntheses of the following quantum dots.

Se stock solution (0.11 mM): 26.056 mg of Se (0.33 mmol) powder was suspended in DDT:OLA (2:1 mL) solution, then, the reaction mixture was magnetically stirred at 120°C in N_2 ambient for overnight.

3.3.1. Synthesis of core ZnSe: $x\text{Eu}^{2+},y\text{Mn}^{2+}$ ($x = 4$ and $y = 12$ mol%) QDs

The ZnSe: $x\text{Eu}^{2+},y\text{Mn}^{2+}$ ($x = 4$ and $y = 12$ mol%) QDs were synthesized at high temperature, through a organo-metals method, using the above metal-oleate and selenium stock solutions as precursors. In a typical procedure, the temperature of the above prepared metal-oleate solution was adjusted to 200°C and quickly injected the above freshly prepared Se solution (0.11 mM) under continuous magnetic stirring and N_2 ambient. Subsequently, the reaction was let to proceed for 15 min to achieve maximum nucleation and crystals growth of ZnSe: $x\text{Eu}^{2+},y\text{Mn}^{2+}$ ($x = 4$ and $y = 12$ mol%) QDs. Finally, the solution was cooled to 60°C by removing the heating source, and the reaction was quenched by injecting three times the volume of ethanol, resulting in precipitation of QDs materials. The product was washed several times by repeatedly suspending in chloroform/acetone mixture and subsequent centrifugation to remove the undesired reaction contents. Similarly, other ZnSe: $x\text{Eu}^{2+}/y\text{Mn}^{2+}$ ($x = 8$ and $12; y = 12$ mol%) and ZnSe: Eu^{2+} (4

mmol%) QDs were prepared by adopting the same synthetic approach and same reaction conditions, using the stoichiometric concentration of Eu^{2+} and Mn^{2+} ions impurities.

3.3.2. Surface passivation of $\text{ZnSe}:\text{xEu}^{2+},\text{yMn}^{2+}$ and $\text{ZnSe}:\text{xEu}^{2+}$ with ZnS monolayers

In a typical synthesis (**Figure 3.2**), successive three and four monolayers (3MLs and 4MLs) of ZnS were grown over the purified $\text{ZnSe}:\text{xEu}^{2+},\text{yMn}^{2+}$ ($x, y = 12$ mol%) and $\text{ZnSe}:\text{Eu}^{2+}$ (4 mol%) QDs in non-coordinating solvent ODE and coordinating solvent/stabilizer OA/OLA/DDT. In this procedure, two separates solutions of Zn-oleate and S were prepared using the equimolar (1:1) amount of Zn and S precursors.

Zn-oleate solution (0.123 mM). Typically, 217.305 mg of $\text{Zn}(\text{CH}_3\text{COO})_2 \cdot 2\text{H}_2\text{O}$ (0.99 mmol), OA (6 mL), and ODE (2 mL) solvents were mixed in a three-necked flask and stirred at 130 °C in N_2 atmosphere for 3 h or until the mixture turned transparent.

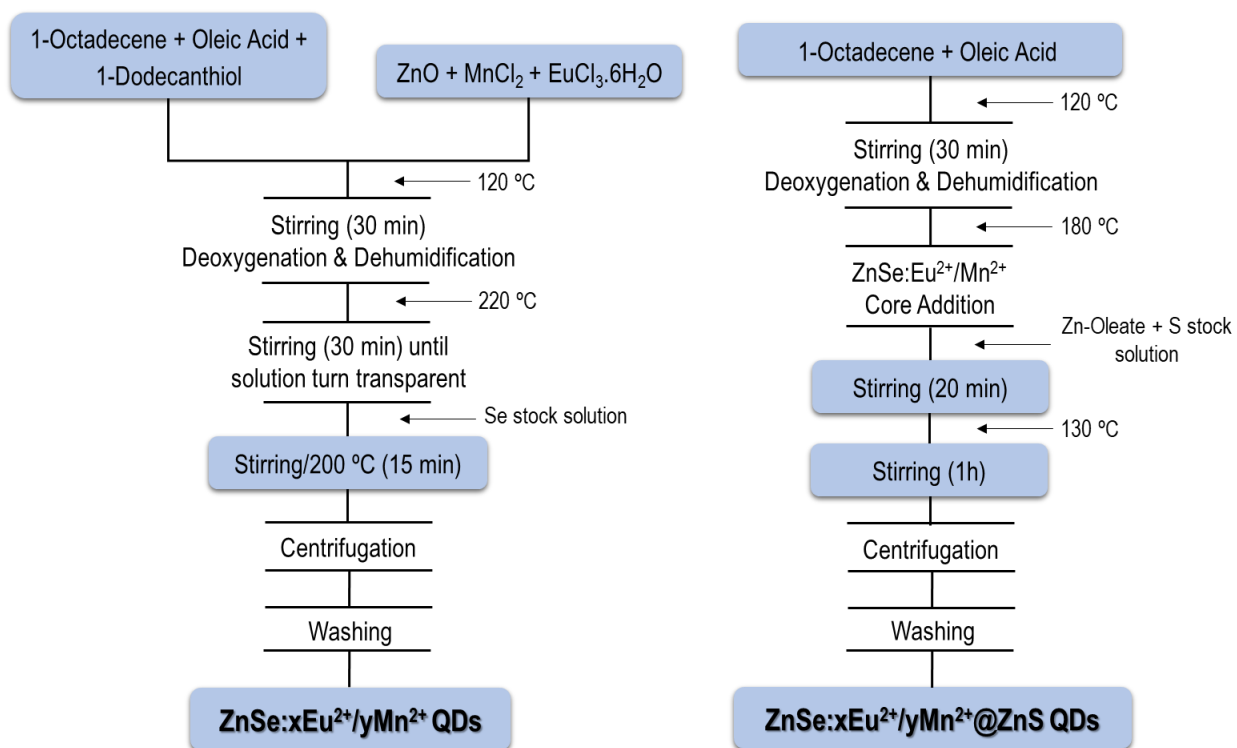
S stock solution (0.55 mM). 31.744 mg of S (0.99 mmol), DDT (1.2 mL) and OLA (0.6 mL) were mixed in 5 mL flask and stirred at ambient temperature for 30 min to obtain a yellowish transparent solution.

3.3.2.1. Synthesis of $\text{ZnSe}:\text{xEu}^{2+}/\text{yMn}^{2+}@\text{ZnS}$ core-shell QDs

In a typical procedure of ZnS shell growth on the surface of core $\text{ZnSe}:\text{xEu}^{2+},\text{yMn}^{2+}$ ($x, y = 12$ mol%) QDs, the ODE (10 mL) and OA (5 mL) solvents were loaded in a three-necked flask and heated to 180 °C. Subsequently, 49.0 mg of already purified core $\text{ZnSe}:\text{xEu}^{2+};\text{yMn}^{2+}$ ($x, y = 12$ mol%) QDs were dispersed in mixture of ODE (1.5 mL) and DDT (0.5 mL) solvents by vigorous sonication and injected in to above freshly prepared solvents mixture. To deposit 3MLs of ZnS shell, the already prepared Zn-oleate (0.123 mM) and S (0.55 mM) precursors solutions were mixed thoroughly, and then, divided into three different portions of 1:2:3 ratios by volume, corresponding to the epitaxial growth of 1st, 2nd, and 3rd MLs of ZnS on the surface of $\text{ZnSe}:\text{xEu}^{2+};\text{yMn}^{2+}$ core QDs. Accordingly, three different injections of the three different portions (1:2:3 by volume) of shell precursors were performed sequentially and periodically in a dropwise fashion (~1 drop/3s), and the growth time was set to 20 min interval after each subsequent injection. Following the post 20 min interval of 3rd injection, the temperature was cooled down to 130 °C and let the reaction for an additional 1h to achieve the maximum nucleation and crystal growth of the ZnS shell. Eventually, the temperature was dropped down to 60 °C and added three times the volume of

ethanol to precipitate the 3MLs ZnS passivated ZnSe: $x\text{Eu}^{2+}$, $y\text{Mn}^{2+}$ QDs. Similarly, 4MLs of ZnS shell were epitaxially grown using the stoichiometric concentration of Zn-oleate and S precursors and the same above reaction conditions.

Figure 3.2 - Schematic illustration of the syntheses of ZnSe: $x\text{Eu}^{2+}$ / $y\text{Mn}^{2+}$ ($x = 4, 8, \text{ and } 12; y = 0$ and 12 mol%) core (left) and ZnSe: $x\text{Eu}^{2+}$ / $y\text{Mn}^{2+}$ @ZnS core-shell (right) QDs.



3.4. Preparation of CdSe and CdSe/ZnS core-shell QDs

A two-steps approach was adopted to prepare CdSe/ZnS core-shell QDs, as shown in **Figure 3.3**. Initially, CdSe QDs were synthesized and purified according to the procedure, as described below, and subsequently passivated with ZnS shell in a separate reaction.

Synthesis of Cd-oleate: The round bottom flask containing a mixture of ODE (10 mL), OA (5 mL), and 133.26 mg of $\text{Cd}(\text{CH}_3\text{CO}_2)_2 \cdot 2\text{H}_2\text{O}$ (0.5 mmol) was heated to 120 °C under continues N_2 flow and magnetic stirring for 30 min to deoxygenate and dehumidify the reaction mixture. Thereafter, the temperature was elevated to 200 °C and maintained until a transparent solution of Cd-oleate was formed, which was used as a precursor for the synthesis of CdSe QDs.

Se stock solution (0.166 mM): 39.48 mg of Se (0.5 mmol) was mixed in DDT (2.0 mL) and OLA (1.0 mL) solvents and loaded in 5 mL flask. The mixture was magnetically stirred in N_2 atmosphere at 120 °C for overnight.

3.4.1. Synthesis of core CdSe QDs

The CdSe QDs were synthesized at high temperature *via* an organo-metals method, using the above Cd-oleate and selenium solutions as precursors (**Figure 3.3**). In a typical procedure, the metal-oleate solution was heated to 200 °C and quickly injected the above freshly prepared hot Se precursor stock solution. The nucleation and growth process was let to proceed and intermittently monitored until red-emitting CdSe QDs were achieved. The reaction was quenched by dropping down the temperature to 60 °C and adding three times the volume of ethanol. The CdSe QDs were isolated by centrifugation and washed several times to remove the unreacted precursors, byproducts, and solvent.

3.4.2. Preparation of color-tunable CdSe/ZnS core-shell QDs

Color-tunable CdSe/ZnS core-shell QDs were prepared *via* interfacial alloying in CdSe and ZnS heterostructures by the organo-metals synthetic approach at 180 °C under N_2 atmosphere. In this synthesis, various S stock solutions labeled as A, B, and C were used to synthesize the orange-emitting $(\text{CdSe/ZnS})_A$, green-emitting $(\text{CdSe/ZnS})_B$, and blue-emitting $(\text{CdSe/ZnS})_C$ core-shell QDs, respectively.

Synthesis of Zn-oleate: The solution of 217 mg of $\text{Zn}(\text{CH}_3\text{CO}_2)_2 \cdot 2\text{H}_2\text{O}$ (0.99 mmol) in ODE (10 mL) and OA (5 mL) were loaded in a three-necked flask and heated to 120 °C under consistent N_2

flow and magnetic stirring for 30 min to deoxygenate and dehumidify the reaction mixture. Subsequently, the temperature was elevated to 200 °C and maintained until a slightly-yellowish and transparent solution of Zn-oleate was formed.

S stock solution (0.495 mM): Three different stock solutions of S designated as A, B, and C were prepared at a fixed amount of 31.7 mg of S (0.99 mmol) while varying the volumes of OLA:DDT solvents from 1:0 to 1:1 and 0:1 mL.

S stock solution A. 31.7 mg of S (0.99 mmol) powder and DDT (2 mL) were mixed in 5 mL flask and magnetically stirred at ambient conditions for 30 min to obtain a clear and transparent solution.

S stock solution B. 31.7 mg of S (0.99 mmol) powder, OLA (1 mL), and DDT (1 mL) were mixed in 5 mL flask and magnetically stirred at room temperature for 30 min to obtain a clear and transparent solution.

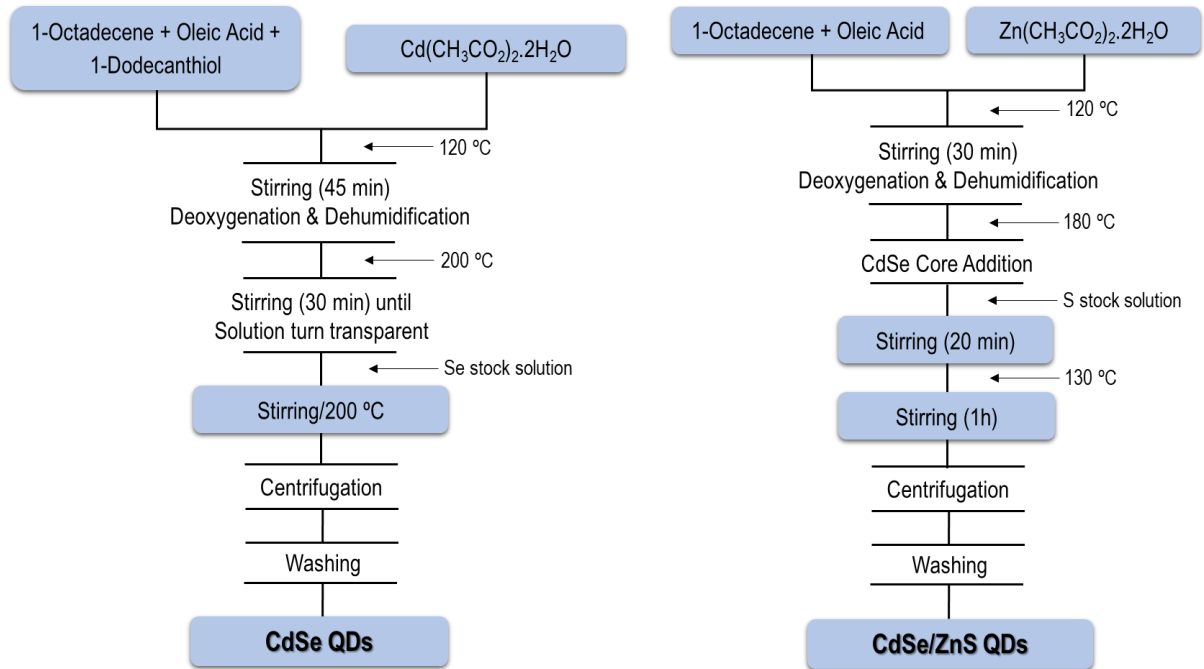
S stock solution C. 31.7 mg of S (0.99 mmol) powder and OLA (2 mL) were mixed in 5 mL flask and magnetically stirred at ambient temperature for 30 min to obtain a clear and transparent solution.

Finally, each solution was divided into three different volumes, i.e., 0.6 mL, 1.0 mL, and 1.4 mL, and used for coating the successive layers (such as 1, 2, and 3 MLs, respectively) of ZnS shell over the surface of core CdSe QDs.

3.4.2.1. Synthesis of CdSe/ZnS core-shell QDs

In a typical synthesis, the temperature of the as-prepared Zn-oleate solution was adjusted to 180 °C and added 63.0 mg of already purified core CdSe QDs dispersion in ODE (2 mL). Subsequently, to prepare an orange-emitting (CdSe/ZnS)_A, injection of solution A into the above reaction mixture was performed in dropwise fashion (~1 drop/3s) and let the reaction post-injection for 20 min to achieve the maximum epitaxial growth of the first ML of ZnS. Similarly, other injections (i.e., 2nd and 3rd) were performed sequentially and periodically to deposit the 2MLs and 3MLs of ZnS shell, pursuing the above reaction conditions. Following the post 20 min interval of 3rd injection, the temperature was dropped down to 130 °C and let the reaction for an additional 1h to maximally grow the 3MLs of ZnS on the surface of the core CdSe QDs.

Figure 3.3 - Schematic illustration of CdSe core (left) and CdSe/ZnS core-shell QDs (right) preparation.



Finally, the solution was cooled down to 60°C and injected three times by volume of ethanol to precipitate the CdSe/ZnS core-shell QDs. The same synthetic approach was adopted to prepare the green-emitting $(\text{CdSe/ZnS})_B$ and blue-emitting $(\text{CdSe/ZnS})_C$ core-shell QDs utilizing the Sulphur solution B and C, respectively.

3.5. Preparation of CdS and CdS/ZnS core-shell QDs

CdS/ZnS core-shell QDs were prepared by two steps procedure *via* pyrolysis of organometals precursors in noncoordinating solvent ODE under nitrogen (N₂) atmosphere at elevated temperature, as described in the flow charts (**Figure 3.4**). Initially, CdS QDs were synthesized and then subsequently passivated with ZnS shell in a separate reaction.

Synthesis of Cd-oleate: 266.53 mg of Cd(CH₃CO₂)₂·2H₂O (1 mmol) was dissolved in ODE (10 mL) and OA (5 mL) solvents in a three-necked flask, and then, de-aerated and dehumidified at 120 °C under consistent N₂ flow for 30 min. Subsequently, the temperature was elevated to 200 °C to obtain the final transparent solution of Cd-oleate.

S stock solution (0.333 mM). 32.065 mg of S (1 mmol), DDT (2.0 mL), and OLA (1.0 mL) were mixed and vigorously stirred at ambient temperature for 30 min to obtain a yellowish transparent solution.

3.5.1. Synthesis of CdS QDs

In a typical synthesis, the temperature of the Cd-oleate containing solution was adjusted to 160 °C and injected quickly the Sulphur precursor solution. Thereafter, the reaction was allowed to keep at two different times, *i.e.*, 5 and 10 min, to embody the crystal growth of CdS QDs. Eventually, the heating source was removed, and the reaction was quenched by adding three times the volume of ethanol at 60 °C. The CdS precipitate was isolated by centrifugation and decantation of the supernatant. The precipitation and redispersion processes were repeated several times in chloroform/acetone (1:2 vol/vol) to remove the undesirable reaction contents.

3.5.2. Surface passivation of CdS core by ZnS shell

The surface passivation of core CdS with ZnS shell is based on the number of injections of S precursor solution in the reaction mixture containing core CdS QDs and shell precursor Zn-oleate. Approximately 6 MLs of ZnS were successively grown on the CdS *via* a two-step method. The amount of Zn and S precursors required for ZnS shell deposition on to the core CdS was determined from the weight and molar ratio between the purified core CdS QDs and ZnS shell precursors.

Synthesis of Zn-oleate: 73.096 mg of Zn(CH₃CO₂)₂·2H₂O (0.33 mmol), ODE (5 mL), and OA (3 mL) were mixed in a three-necked flask. Then, the mixture was degassed and dehumidified under

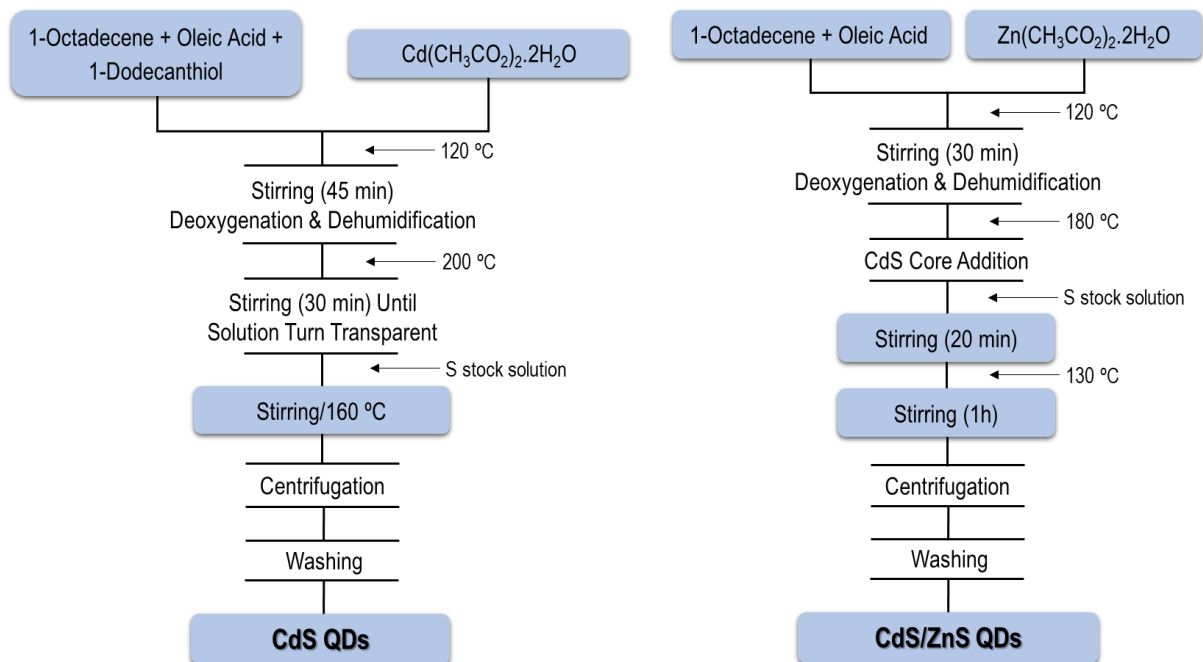
N₂ atmosphere at 120 °C for 30 min. Subsequently, the temperature was elevated to 250 °C and let the reaction until the solution was turned clear and transparent.

S stock solution (0.11 mM): Sulfur precursor solution was prepared by solubilizing elemental 10.677 mg of S (0.33 mmol) in DDT (2.0 mL) and OLA (1.0 mL) under vigorous magnetic stirring at ambient temperature for 30 min. The corresponding solution was partitioned into three equal volumes for the surface passivation of 1ML, 2MLs, and 3MLs of ZnS.

3.5.2.1. Synthesis of CdS/ZnS core-shell QDs

The as-prepared 48 mg of purified CdS QDs were added to ODE (3 mL) and re-dispersed by ultra-sonication. The suspension of CdS QDs was loaded into a syringe and injected into the Zn-oleate solution at 190 °C. After the 2 min of an interval, the S precursor solution was introduced in a dropwise fashion (~1 drop/3s) into the above solution. Subsequently, the post 20 min interval was set to grow the ZnS shell. Similarly, other injections were performed sequentially and periodically under the same reaction conditions followed by a 20 min post-injection interval. Finally, the temperature was adjusted to 130 °C, and the reaction was allowed to proceed for an additional 1h to maximize the epitaxial growth of the ZnS shell. Then, the temperature was lowered to 70 °C and added three times by the volume of ethanol to obtain the flocculant precipitate of CdS/ZnS QDs. The core-shell QDs were isolated and purified by the same approach as adopted for the core CdS. A similar procedure was applied to grow the surface coatings of 4 to 6 MLs of ZnS, by increasing the amount of reagents, accordingly. The obtained CdS/ZnS core-shell QDs were soluble in various organic solvents, such as chloroform, dichloromethane (DCM), hexane, toluene, etc.

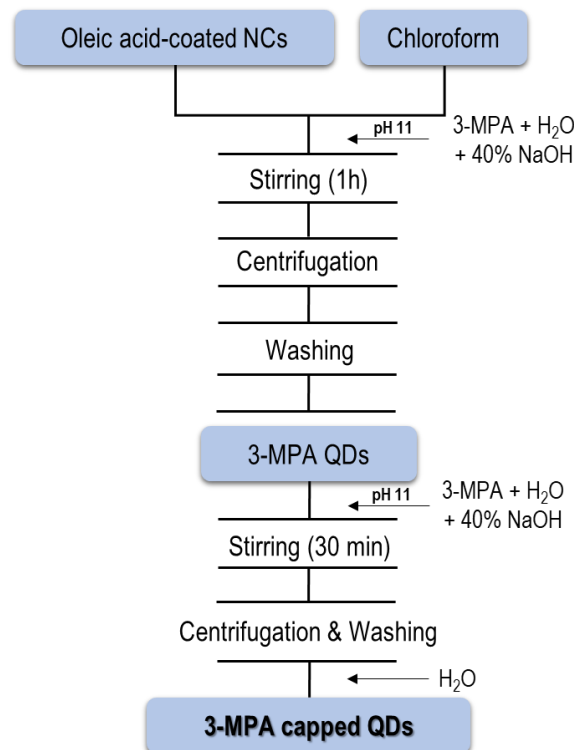
Figure 3.4 - Flow chart diagrams of core CdS (left) and CdS/ZnS core-shell (right) QDs preparation.



3.6. Aqueous solubilization of QDs *via* a ligand exchange reaction

The as-prepared organic solvent-soluble OA/OLA/DDT capped QDs were transformed into an aqueous soluble (**Figure 3.5**) by replacing OA/OLA/DDT with a hydrophilic 3-MPA organic compound through ligand exchange reaction approach, as previously reported in the literature [102], [103]. Two separate homogenous solutions A and B were prepared by mixing 0.0128 mg of QDs in 9 mL chloroform, and 1.8 mL 3-MPA in 6 mL deionized water, respectively. Solution B was adjusted to pH ~11 by dropwise addition of aqueous NaOH solution (40%) and then added to solution A. The resulting biphasic mixture was stirred vigorously for 1h at room temperature. Eventually, the underlying organic phase was discarded, and the remaining QDs containing aqueous phase was added acetone in excess. The solution was centrifuged at 14000 rpm×3 min, and the supernatants were decanted to remove the excess 3-MPA and isolate QDs functionalized with 3-MPA. The obtained QDs were further resuspended in 3 mL of aqueous 3-MPA (0.9 mL) solution, adjusted the pH to ~11, and stirred for an additional 30 min. Thereafter, 3-MPA capped QDs were isolated and dissolved in water to obtain a clear, transparent, and highly stable aqueous colloidal solution for further use in biological study.

Figure 3.5 - Flow chart diagram of aqueous solubilization of QDs *via* ligand exchange reaction.



3.7. Materials characterization

3.7.1. X-ray Diffraction (XRD)

XRD patterns were measured to determine the phase structure of QDs employing RIGAKU MINIFLEX-II diffractometer, operating at Cu K α ($\lambda = 1.5406 \text{ \AA}$) in the 2θ range of 10-90 degree. The facility was provided by Laboratório de Nanotecnologia Molecular e Marcadores Integrados Centro de Química e Meio Ambiente (CQMA) at the Nuclear and Energy Institute (IPEN).

3.7.2. Transmission Electron Microscope (TEM)

The size and morphology of QDs were determined by transmission electron microscopy, JEOL JEM 2100F TEM-FEG (acceleration voltage 200 kV, Spot Size 1, Alpha Selector 3). Samples were prepared by gently adding a drop of QDs dispersion in chloroform/Milli-Q water on a carbon-coated copper grid (ultrathin carbon/holey carbon, 400 mesh, Ted Pella, Inc). Single-tilt sample holder was used, and images were acquired with Gatan 831.J45M0 camera, using Gatan Digital Micrograph and EMMENU programs. The analyses were performed in Brazilian Nanotechnology National Laboratory (LNNano), Centro Nacional de Pesquisa em Energia em Materiais (CNPEM), Campinas-SP, and the Analytical Center of Institute of Chemistry, University of Sao Paulo (IQ-USP).

3.7.3. Dynamic Light Scattering (DLS)

The colloidal stability, including hydrodynamic size and polydispersity index (PDI), of the as-prepared aqueous soluble QDs was assessed in the ultrapure Milli-Q water, RPMI supplemented with 10% FBS, and pure FBS (100%) at the dilute concentration (100 $\mu\text{g/mL}$), using dynamic light scattering (DLS). The surface charge (ζ -potential) of the QDs was determined *via* electrophoretic light scattering (ELS), using a Zetasizer Nano ZS90 instrument (Malvern Instruments, UK) installed in Laboratório de Nanotecnologia Supramolecular, Instituto de Química, Universidade de São Paulo (IQ-USP).

3.7.4. Atomic Force Microscope (AFM)

Average height (Z-dimension) of QDs and respective aggregates in Milli-Q water (50 mg L $^{-1}$) was investigated by air drying of 5 μL solution of QDs (50 $\mu\text{g/mL}$) over mecca surface (Ted Pella Inc). AFM images were obtained utilizing Flex AFM (Nanosurf) integrated C3000 controller,

operating on TAP190-AI-G cantilever (Budget Sensors). The facility was provided by Laboratório de Nanotecnologia Supramolecular, Instituto de Química, Universidade de São Paulo (IQ-USP).

3.7.5. X-ray Photoelectron Spectrometer (XPS)

The surface elemental compositions of the QDs were determined with K-Alpha X-ray Photoelectron Spectrometer from Thermo Fisher Scientific Inc., using a monochromatic Al K_{α} X-rays (λ : 1486.6 eV) of 300 μm spot size. The survey spectrum was recorded in the energy range of 0–1350 eV by scanning three specific regions in the sample at pass energy of 200 eV and 400 μm spatial resolution. High-resolution spectra in the binding energy ranges of Zn 2p, Se 3d, S 2p, Mn 2p, O 1s, and C 1s were measured at pass energy of 50 eV and incremental step size of 0.1 eV. The deconvolution of peaks and subtraction of background were performed using Avantage 5.89 software from Thermo Scientific. The facility was extended by Brazilian Nanotechnology National Laboratory (LNNano), Centro Nacional de Pesquisa em Energia em Materiais (CNPEM), Campinas-SP.

3.7.6. Photoluminescent Spectroscopy

The luminescence spectra and decay curves of QDs were recorded in chloroform solution (100 mg L⁻¹) at room temperature, using HORIBA Jobin Yvon Fluorolog-3 spectrofluorometer. This equipment contains 450 W xenon lamp and pulsed Xenon flash lamp as excitation sources, double grating monochromators, CCD detector, and phosphorimeter accessory. The luminescence data can be processed in FluorEssence software that merges the acquisition of data from the spectrofluorometer directly to the Origin software. This facility is available at the laboratory of *f*-block elements, Institute of Chemistry, University of Sao Paulo-USP.

3.7.7. UV-visible Absorption Spectroscopy

UV-visible absorption spectra of QDs were acquired in chloroform by UV-2600 UV-vis spectrophotometer, Shimadzu, covering a wavelength range from 285 nm to 1400 nm. This facility is available at the laboratory of *f*-block elements, Institute of Chemistry, University of Sao Paulo-USP.

3 Experimental Part B

3.8. Cell Culture Growth

Raw 264.7 cells were purchased from Sigma-Aldrich and were used without any treatment. In a typical procedure, took 1 mL of Raw 264.7 cells (macrophages) suspension and suspended in RPMI 1640 (15 mL) cell culture media (Sigma-Aldrich) in 50 mL polypropylene tube. Subsequently, centrifuged the cells at 1500 rpm (450*g) for 5 min and discarded the extra DMSO. The cells were resuspended in 15 mL of RPMI 1640 medium supplemented by FBS (10%), gentamycin (10 µg/ml), penicillin (100 IU/ml), L-glutamine (2 mM), and Hepes (10 mM) and maintained at 37 °C in CO₂ (5%) and humidified ambiance. The old medium was replaced by fresh medium after each successive 3 days.

3.8.1. Cells counting

RAW cells were trypsinized or scraped gently and vigilantly and subsequently pelleted by centrifuging at 1500 rpm for 5 min. The pellets were redispersed in 1 mL RPMI medium and gently swirled to ensure that the cells are distributed evenly and individually. Before the cells precipitate, draw out 10 µL of cell suspension in eppendorf tube and diluted up to 1% by the addition of 990 µL trypan blue. Placed the glass coverslip gently over the counting chambers, vertex the trypan blue-treated cell suspension applied 10 µl into the hemacytometer at the edge of the coverslip and let to run under it. The hemacytometer grids were visualized under the microscope and counted the live and dead cells, respectively. The cells that appeared colorless and bright (refractile) under phase contrast were considered live cells, and the stained blue and non-refractile were counted dead cells. The number of cells that were touching boundaries of squares were counted in half of the total squares. The total concentration of cells was calculated by dividing the total cell concentration with the number of corner squares and multiplying it with the dilution factor and 10⁴.

$$\text{Total concentration of live cells (cells/ml)} = \text{live cells count/no of squares} \times \text{dilution factor} \times 10^4$$

$$\text{Viability (\%)} = \text{live cells count/live + dead cells count} \times 100$$

3.9. Toxicity Assessment of QDs in RAW Macrophages

The biocompatibility and toxicity of the as-prepared different types of ZnSe:Mn²⁺, ZnSe:Eu²⁺/Mn²⁺@ZnS, CdSe/ZnS, and CdS/ZnS QDs were assessed in RWA macrophages *via*

trypan blue-exclusion assay, MTT assay, and Annexin V/Propidium iodide (PI) staining assay. It was used just cellular medium as a negative control in all assays.

3.9.1. Trypan blue exclusion assay

Briefly, Raw 264.7 cells were seeded in 24-well plates at a density of 1×10^5 cells/well in RPMI medium containing 10% FBS and were allowed to adhere to the plates for 30 min by storing in a humidified atmosphere with an afflux of 5% CO₂ at 37 °C. Thereafter, the wells-plate was washed with PBS, resuspended in RPMI medium supplemented by FBS (10%), and subsequently added each well stock solution of QDs (100 µg/mL) already prepared in PBS. The cells were incubated for various time intervals: 15 and 30 min, 1, 2, 4 h, and 6 h, respectively. Finally, all the wells were washed with PBS to remove the excess QDs and added trypan blue. The cell viability was determined by counting the live and dead cells using the following formula.

$$\text{Viability (\%)} = \text{live cells count} / (\text{live} + \text{dead cells count}) \times 100$$

3.9.2. MTT and Griess assay

RAW 264.7 cells (1×10^5) were seeded in 96-well plates and let to adhere to plate bottom for 24 h. Next day, the medium was aspirated, and the cells were exposed to various QDs dispersion of 25, 50, and 100 µg/mL prepared in DMEM media supplemented with 10% FBS for 24 and 48 hours. After the desired time, the cells were washed with PBS and added each well 25 µL of tetrazolium solution prepared by dissolving 5 mg tetrazolium salt in 1 mL water. Placed the plate in the dark and waited for 2 hours. Subsequently, the MTT solution was aspirated vigilantly and meticulously to avoid the sucking of floating dead cells containing formazan crystals. The remaining formazan crystals were dissolved by adding 100 µL of DMSO, obtaining the purple solution of formazan. The quantity of formazan produced is tantamount to the cell viability. The absorbance of the formazan solution was measured by the ELISA microplate reader at 570 nm, and the intensity was correlated to cell viability or cytotoxicity.

Potential macrophage activation by QDs uptake was assessed by quantifying nitric oxide (NO) production via Griess reaction. 100 µL of cellular medium supernatants of QDs treated cells for MTT assay were collected and mixed with equal volume (100 µL) of Griess reagent, a mixture of phosphoric acid, sulfanilamide (1%), and N-(1-naphthyl)ethylenediamine hydrochloride (0,01%). The optical density of each well was measured at 595 nm. Cells treated with cell medium

(D10) were used as negative control and the cells stimulated with lipopolysaccharides (LPS) (1 ug/mL) were used as positive control. The quantification was performed immediately after incubation to avoid loss of signal, using a calibration curve prepared with sodium nitrite. It is worth mentioning that NO is very reactive so that, soon after it is formed inside cells by iNOS and released in the extracellular medium, it is converted into nitrite by reaction with oxygen gas.

3.9.3. Annexin V/Propidium (PI) staining assay

Cells preparation: In a typical approach, seeded 2×10^5 cells/well of RAW 264.7 cells in 24-wells plate containing DMEM medium supplemented with 10% FBS and stored in a humidified atmosphere with an afflux of 5% CO₂ at 37 °C for 24 h. The next day, aspirated the medium and added 100 µg/ml of ZnSe:Mn²⁺ (15 mol%) QDs suspended in DMEM medium fortified with 10% FBS. The cells were incubated over different periods: 15 and 30 min, 1, 2, 4, and 6 hours. After the desired time, the medium was sucked out, and the cells were harvested by adding trypsin (100 µl/well), storing at 37 °C for 5 min. Each sample was transferred to a separate tube and centrifuged at 300 rpm for 4 min to remove the trypsin solution. The cells were washed two times by adding PBS (50 µl), followed by subsequent centrifugation and decantation.

Annexin V/PI application: The supernatant was discarded by inverting and taping the tube on absorbent paper and resuspended the cells in 50 µl/tube of Annexin V solution for 20 min in a dark place. The Annexin V solution was prepared by dissolving Annexin V in Annexin-binding buffer (1:50). Similarly, prepared the solution of PI in Annexin-binding buffer (0.5:200) and added each sample 200 µl of the PI solution, obtaining a final volume of 250 µl.

Control cell preparation: Induced cell death by placing in thermomixer at 65 °C for 5 min and stained by Annexin V/PI markers.

- Positive for Annexin V without PI for the detection of apoptosis.
- Positive for PI without Annexin V for the detection of necrosis.
- Positive for both Annexin V and PI.
- And untreated negative control cells.

FACS analysis: Cell viability was measured by acquiring 10,000 events in a flow cytometer Accuri C6 (BD Biosciences, San Jose, USA).

3.9.4. Quantitative PCR for the expression of pro- and anti-apoptotic macrophage genes

To evaluate the expressions of pro- and anti-apoptotic macrophage genes, total RNA was extracted from 2×10^5 cells/mL using TRIzol (Invitrogen, USA), following the manufacturer's protocol (RNA integrity was determined as an OD 260/280 absorption ratio from 1.8 to 2.1). The purified RNA was used as a template to synthesize cDNA. Briefly, 1 μ g of RNA was mixed with 10 μ l of a solution consisting of a basic buffer (100 mM Tris-HCl, pH 8.3, containing 500 mM of KCl and 15 mM of MgCl₂ Invitrogen, USA), dNTP (10 mM; Fermentas, USA), random primers (Invitrogen, USA), OligoDT primers (Invitrogen, USA), RNaseOUT recombinant ribonuclease inhibitor (40 U μ l⁻¹; Invitrogen, USA), M-MLV reverse transcriptase (100 U μ l⁻¹). The reactions were incubated at 37°C for 50 min and were denatured at 70°C for 15 min.

For real-time quantitative RT-PCR, the following primers set were designed: murine Bax gene (GenBank Accession No. NM007527), forward: 5'-GGC CTT TTT GCT ACA GGG TTTCAT-3' and reverse: 5'-TGC TGT CCA GTT CAT CTC CAA TTC-3' and for murine Bcl-2 gene, forward: 5'-GAC TGA GTA CCT GAACCG GCA TCT-3' and reverse: 3'-AAG CCC AGA CTC ATT CAACCA GAC-3' (GenBank Accession No. NM009741). The β -Actin gene (GenBank Accession No. NM00739) was used as a constitutively expressed control gene for normalization (primers: forward, 5'-GCC TTC CTT CTT GGGTAT GGA ATC-3' and reverse, 5'-ACG GAT GTC AAC GTC ACACTT CAT-3'). The reactions included master mix Syber Green(2 \times) (Applied Biosystems, USA) and 1 μ L cDNA (1 μ g) template and were run in triplicate on a real-time PCR system (StepOne; Applied Biosystems, USA). The PCR conditions were the same for all primer combinations: 95 °C for 10 min, 40 cycles of 92 °C for 2 min, 57.5 °C for 30 s and 70 °C for 30 s. After PCR amplification, a melting curve was generated to confirm the specificity of the products. The data were presented as relative quantification and were calculated using $2^{-\Delta\Delta C_t}$ (Pfaffl, 2001).

3.10. Time-dependent Uptake and Imaging of QDs in RAW Macrophages

Preparation of cells: RAW 264.7 cells (2×10^5 cells/well) were seeded in 24-well plates containing DMEM medium fortified with 10% FBS. The cells were allowed to adhere to the coverslip in a humidified incubator at 37 °C and 5% CO₂ for 24 hours. Thereafter, the medium was aspirated, and the cells were washed several times with PBS solution. Quantum dots were then introduced to cells at a final concentration of 100 μ g/ml. To prepare the 100-ppm solution, 1 mg of QDs was dispersed in 1 ml Mill-Q water and further diluted by taking 100 μ l QDs solution and mixing with

900 μ l culture medium. Each well was then applied 500 μ l QDs solution and incubated for 15 and 30 min and 1 h, respectively. Cells were fixed on coverslip by the application of 60 μ L/well of 4% Para Formaldehyde (PFA) for 8 min. Washed the cells several times with 60 μ L/well of 1x PBS solution, removed the coverslip gently from well, and fixed on to the slide upside down.

3.10.1. CytoViva hyperspectral microscopy imaging and mapping

CytoViva® (CytoViva, Inc., AL, USA) enhanced darkfield hyperspectral ultramicroscopy system was used to evaluate the cellular uptake of QDs over different incubation time. Darkfield hyperspectral images were acquired with enhanced dark-field transmission optical microscope Olympus BX-41 (Melville, New York, USA) integrated with hyperspectral imaging spectrophotometer (CytoViva Inc., Auburn, Alabama, USA). All the images were measured with 60x objective, and hyperspectral data collection and mapping were performed using ENVI 4.8 software. Spectral library of the pure QDs aggregates ($n \geq 50$) was collected in 400-1000 nm spectral region and then matched with hyperspectral images of macrophages incubated with QDs at a different time (15 min, 30 min, and 1h). The spectral match between the image pixels in the hyperspectral image of each cell against the spectral library of QDs was performed using the internal spectral mapping algorithm. The hyperspectral mapping images were further processed and inserted scale bar using free ImageJ software. Live cells fluorescence images were measured without fixing the cells and exciting the QDs at 380 nm, using the CytoViva dual-mode fluorescence module.

CytoViva Dual Mode Fluorescence (DMF) imaging of live cells: Seeded RAW 264.7 cells (2×10^5 cells/well) in 24-wells plate containing DMEM medium supplemented with 10% FBS. The cells were allowed to adhere to the coverslips in a humidified incubator at 37 °C and 5% CO₂ for 24 hours. The next day, aspirated the medium and added 100 μ g/ml of QDs suspended in DMEM medium fortified with 10% FBS and incubated for 30 min and 1 hour. Subsequently, the coverslips were removed gently, mounted on a slide, and the images were acquired under CytoViva Dual Mode Fluorescence (DMF) microscopy.

3.10.3. Transmission electron microscopy imaging

The detailed study of QDs internalization and localization in cells was performed using transmission electron microscopy (TEM). For TEM images measurements, cells were grown on

24-well plates at a density of 2×10^6 cells/well and incubated with QDs (10 $\mu\text{g}/\text{mL}$) for 15 min, 30 min, and 1 hour. Cells were scraped, washed with PBS and immediately fixed in Karnovsky fixative solution: 2.5% glutaraldehyde (Electron Microscopy Sciences) and 1% paraformaldehyde (Sigma), in 0.1 M sodium cacodylate buffer (pH 7.2) (Serva). Cells were subsequently dehydrated in alcohol, encased in epoxy resin (Polybed), thinly sectioned with a Sorvall MT6000 ultramicrotome, and mounted on a copper grid. TEM images were acquired with LEO 906E Zeiss TEM (Leo Electron Microscopy Ltd Corporation Zeiss Leica, Cambridge, England), operating at 60 kV.

3.11. Uptake Mechanism of QDs in RAW Macrophages

Raw 264.5 cells (2×10^5 cells/well) were plated in 24-wells plate containing 500 μL of DMEM medium supplemented with 10% FBS and let to adhere to plate for 24 hours. To elucidate the uptake pattern, the cells were suspended in 250 μL of fresh FBS free DMEM medium and preincubated for 1 h with different types of endocytosis inhibitors i.e., 0.5 M sucrose (clathrin-mediated endocytosis inhibitor), 5 mM methyl- β -cyclodextrin (M β CD) (caveolae-mediated endocytosis inhibitor), 4 μM cytochalasin D (Cyto D) (phagocytosis inhibitor), and on ice (general inhibitor of all energy-dependent uptake mechanism). Subsequently, the cells were added 50 $\mu\text{g}/\text{mL}$ of QDs without discarding the old medium and granted an additional 3 h (except, ZnSeMn²⁺ was given 1h) incubation time. Each study was categorized into negative control (without QDs and inhibitors), positive control (with QDs without inhibitors), and cells with QDs and inhibitors.

3.11.1. Microplate reader analysis

Eventually, all the cells were washed two times with PBS to remove the noninternalized and passively adhered quantum dots. Subsequently, added 0.1% Triton-X-100 (200 $\mu\text{L}/\text{well}$), and the cells were mechanically lysed by gentle sonication for 1 min and additional pipetting (up-down process). Finally, 100 μL of the obtained cellular lysate was transferred to a black 96-well plate, added 100 $\mu\text{L}/\text{well}$ of Milli-Q water and recorded for quantitative uptake of QDs by TECAN microplate reader (TECAN, Infinite M200, Austria GmgH, Grödig, Austria) utilizing the fluorescence intensity of QDs.

3.11.2. Flow cytometry (FACS) analysis

After the desired time, the medium was sucked out, and the cells were harvested by adding 200 μ L/well of trypsin followed by incubating at 37 °C for 5 min. The enzymatic reaction was quenched by adding FBS (10%) fortified PBS and transferred each sample to an individual tube and subsequently centrifuged at 3000 rpm for 4 min. The cells were washed two times by dispersing in PBS (50 μ l) and subsequent centrifuging. Resuspended the cells in PBS (400 μ l) and analyzed by flow cytometry FACS LSRFortessa (BD Biosciences) exciting the QDs by violet (405 nm), blue (488 nm), green-yellow (561 nm), and red (633-640 nm) lasers. The obtained data were further processed by Flowjo software (TreeStar, Ashland, OR, USA).

3.4.10. Statistical analysis

Student's t-test, ANOVA, and Dunn's Multiple Comparison tests were used to determine the mean differences among groups. All statistical analyses were performed using the GraphPad Prism 8.0.1 (244) software. The values are expressed as the mean \pm standard deviation of at least three independent assays. A p-value of ≤ 0.05 was considered statistically significant.

Chapter 4

CHARACTERIZATION OF QDs

4 CHARACTERIZATION OF QDs

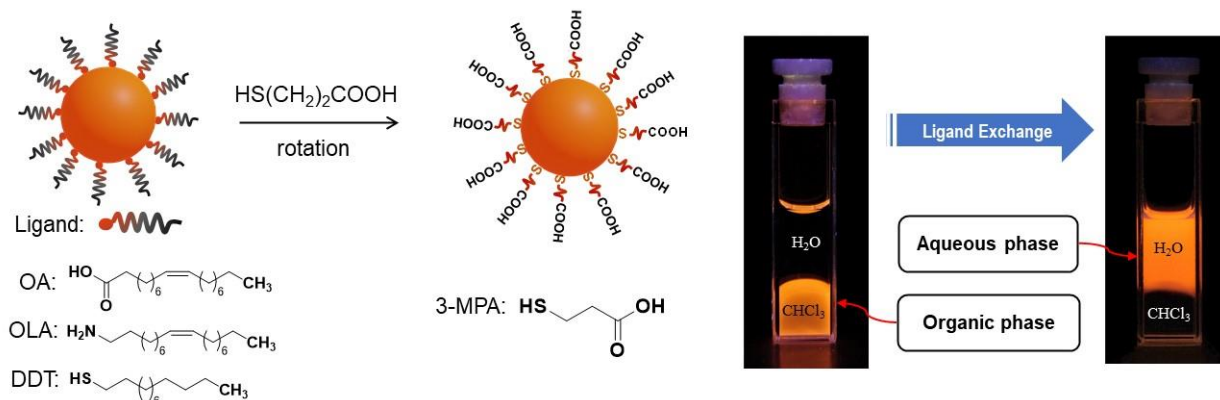
4.1 Color-tunable fluorescent quantum dots

Semiconductor nanocrystals of quantum confinement size have gained substantial research interest since the last decade due to having intrinsic potentialities for use in nanomedicine: These include the fluorescent label for cell tracking, bioimaging, biosensing, therapeutics, and theranostics. The QDs exhibit considerable photo-stability, high quantum yield and molar extinction coefficient, long fluorescence lifetime, and size-dependent tunable emission from UV-visible to near-IR region. Therefore, multiple color-tunable fluorescent QDs were designed and prepared to explore for the development of a bionanoprobe, exploiting in the medical and clinical diagnostics.

4.2. Orange-emitting ZnSe: x Mn²⁺ ($x = 5, 10, \text{ and } 15 \text{ mol}\%$) QDs

Orange color fluorescence ultra-small Mn²⁺ doped ZnSe QDs were prepared by a high-temperature organo-metals method in a noncoordinating ODE and coordinating OA/OLA/DDT solvents, using zinc oxide, manganese (II) chloride and selenium powder as precursors. The as-prepared OA/OLA/DDT coated QDs were only soluble in organic solvents, and the aqueous solubility is the prerequisite for the study *in vivo* and *in vitro*.

Figure 4.2.1 - Schematic illustration of the ligand exchange reaction of OA/OLA/DDT capped ZnSe:Mn²⁺ QDs with 3-MPA organic ligand to become aqueous soluble.



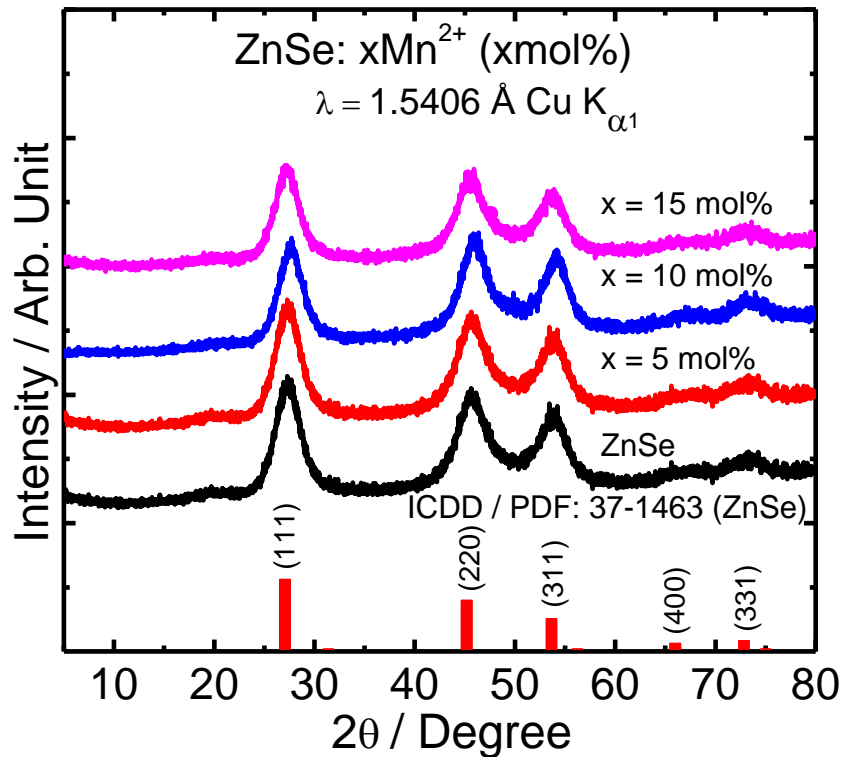
Digital photographs show the transformation of QDs from the organic phase to the water phase after capping with 3-MPA, irradiating by UV lamp ($\lambda = 365 \text{ nm}$).

Therefore, ZnSe:Mn²⁺ QDs were functionalized with hydrophilic 3-MPA organic moiety, through ligand exchange reaction, which turned them soluble in aqueous and cell culture media, as schematically shown in **Figure 4.2.1**.

4.2.1. Physicochemical characterization

X-ray diffraction: XRD patterns of the ZnSe and ZnSe:xMn²⁺ (x = 5, 10, and 15 mol%) QDs (**Figure 4.2.2**) exhibited characteristic three major diffraction peaks at 2θ values of 27.28°, 45.63° and 53.85°, corresponding to (111), (220) and (311) lattice planes of cubic zinc-blende phase of ZnSe (ICDD/PDF 37-1463) [104]. XRD patterns reveal no predominant phase transformation in the cubic zinc-blende structure of ZnSe after doping with Mn²⁺, and no extra diffraction peaks from Mn or MnSe phases were observed.

Figure 4.2.2 - XRD patterns of ZnSe and ZnSe:xMn²⁺ (x = 5, 10, and 15 mol%) QDs.



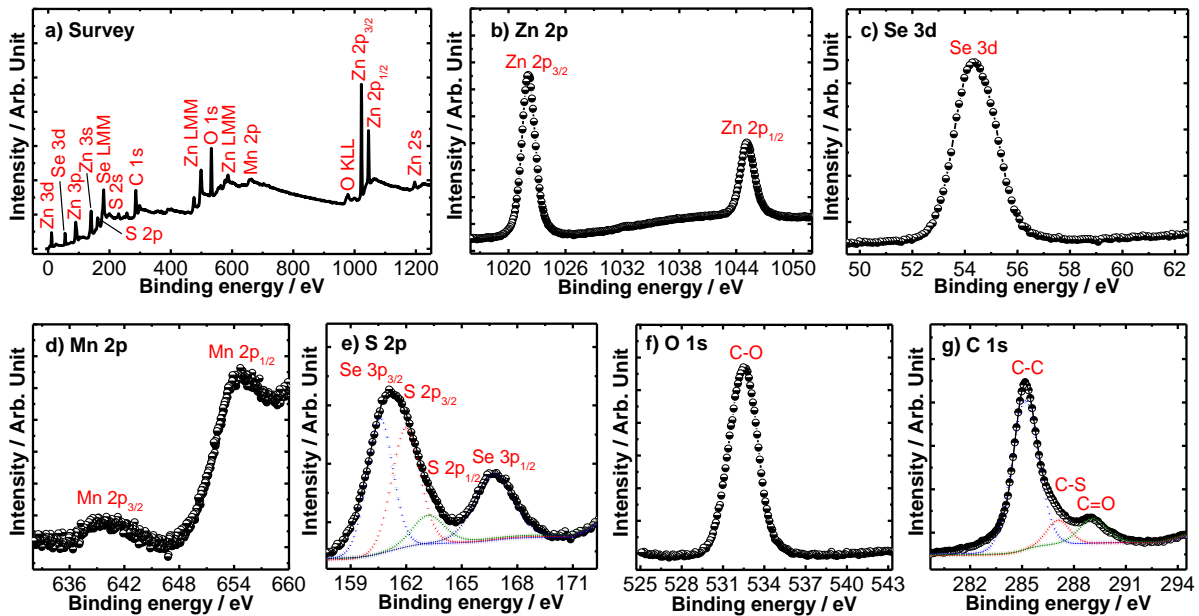
However, a slight shift in the diffraction peaks of ZnSe:Mn²⁺, when compared to the ZnSe matrix (**Figure 4.2.2**), is attributed to the larger ionic radius of Mn²⁺ (0.80 Å) than that of Zn (0.74

Å). Additionally, the broadened XRD peaks represent the ultrasmall nanocrystalline nature of the ZnSe and Mn²⁺ doped ZnSe quantum dots.

X-ray photoelectron spectroscopy: The surface elemental composition of water-soluble QDs was studied by X-ray photoelectron spectrometry (XPS), as shown in **Figure 4.2.3**. The survey spectrum of the ZnSe:Mn²⁺ QDs shows the Zn and Se as the most abundant elements and traces of Mn dopant well as, suggesting the formation of ZnSe:Mn²⁺ quantum dots. The peaks in the binding energies range of C 1s, O 1s, and S 2p signals are originated from the surface hydrocarbon. The deconvoluted C 1s core high-resolution spectrum (**Figure 4.2.3**) exhibits the peaks that are attributed to the C-C (BE = 285 eV), C-S (BE = 287 eV) and O-C=O (BE = 289 eV) bonds, indicating the presence of surface 3-MPA organic moiety. The high-resolution XPS spectrum in the Se 3d region manifests the presence of the Zn-Se and Mn-Se bond.

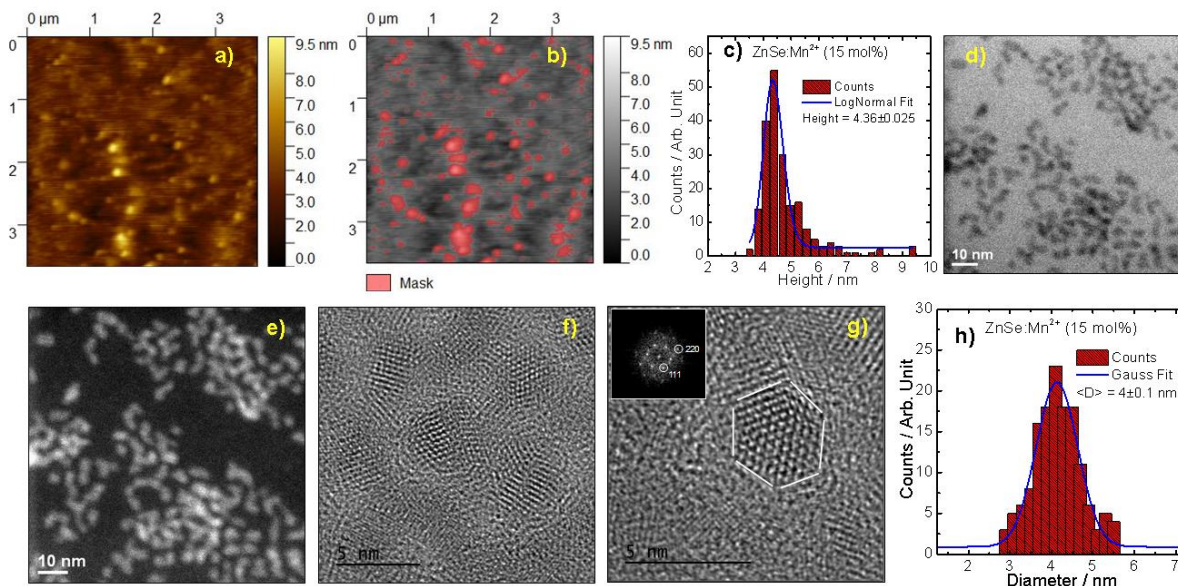
The Se 3d peak is usually doublet (Se 3d_{5/2} and Se 3d_{3/2}) because of the spin-orbit coupling with a branching ratio of 1.5 and a binding energy separation of 0.9 eV [105]. However, a single broadened peak at a binding energy of ~ 54.4 eV (Se 3d_{3/2}) was assigned to the Se bonded to either Zn or Mn, as shown in **Figure 4.2.3**. It is noteworthy that the high-resolution Se 3d spectrum exhibits no peaks for the elemental Se⁰, which is usually observed as a doublet at higher binding energies of 54.9 eV (Se 3d_{5/2}) and 55.8 eV (Se 3d_{3/2}) as reported in the literature [105], negating the presence of free elemental selenium in the 3-MPA capped Mn²⁺ doped ZnSe QDs. Besides, the characteristic Mn 2P_{3/2} peak at bonding energy of 641.8 eV is consistent with MnSe, manifesting that the Mn dopant is bonded to the Se [106]. The overall XPS results confirm the formation of Mn²⁺ doped ZnSe QDs capped with 3-MPA.

Figure 4.2.3 - XPS spectra, including wide-scan or survey (a), high resolution spectra measured in bonding energy ranges of Zn 2p (b), Se 3d (c), Mn 2p (c), S 2p (e), O 1s (f) and C 1s (g) signals for the 3-Mercaptopropionic acid capped Mn^{2+} doped ZnSe QDs.



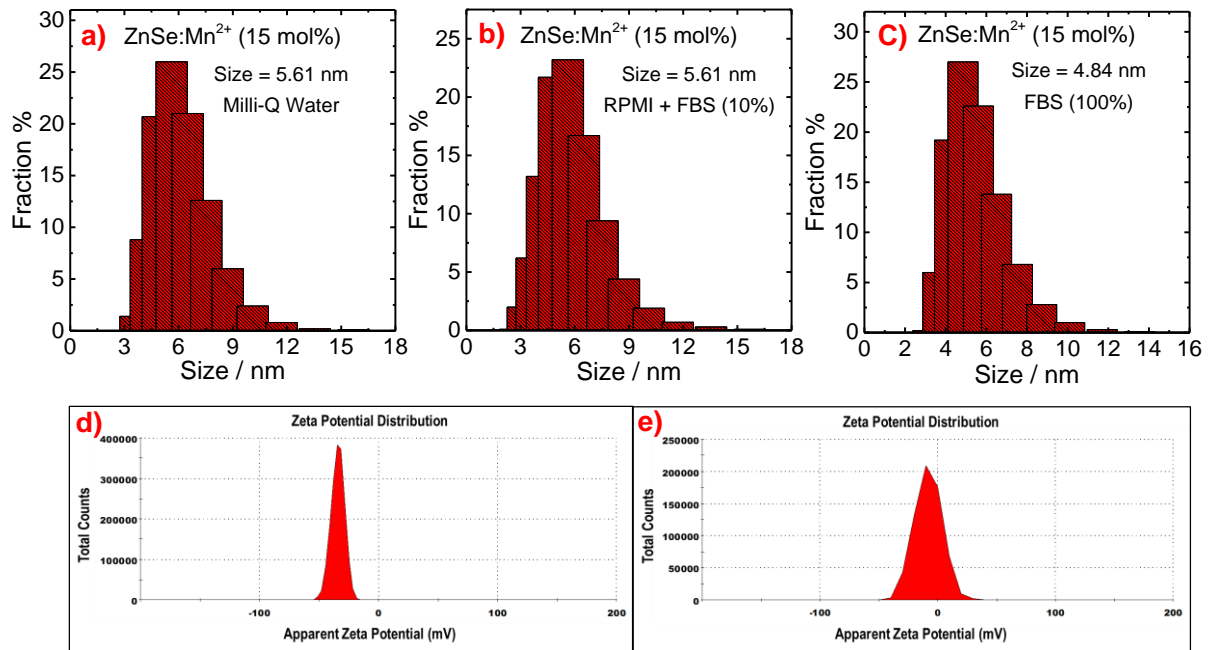
AFM and TEM images: Atomic force microscopy (AFM) was used to provide corroborative evidence on the shape, morphology, and average height (Z-dimension) of Mn^{2+} doped ZnSe QDs. AFM images of 3-MPA capped QDs showed an average height (Z-dimension) of ~ 4.3 nm (**Figure 4.2.4**) closely consistent with the TEM measured size distribution of OA/OLA/DDT capped QDs. TEM images of the QDs (**Figure 4.2.4d-g**) show ultra-small cubic and ellipse shapes nanocrystals with narrow size distribution and dominant average diameter of ~ 4 nm, as deduced from the histogram of the particles size distribution (**Figure 4.2.4h**). The average diameter was obtained by counting more than one hundred of QDs, using image J free software and nonlinearly curve fitting (Gauss fit) in origin 8.5. The FFT pattern shows the diffraction spots of 111 and 220 that correspond to the 3.29 and 2.0 Å interplanar spacings, respectively, confirming the presence of the cubic zinc-blende ZnSe crystalline structure, corroborating through the XRD pattern (**Figure 4.2.4**).

Figure 4.2.4 - AFM topography (a), phase contrast images (b) and height profile (Z-dimension) histogram (c) of 3-MPA capped ZnSe:Mn²⁺ QDs, bright-field (BF) (d), high-angle annular dark-field (HAADF) (e), HRTEM images (f-g) and histogram of particle size distribution (h) of OLA capped ZnSe:Mn²⁺ QDs.



Hydrodynamic size and zeta potential: The 3-MPA capped ZnSe:Mn²⁺ QDs exhibited considerable colloidal stability in water, cell culture media (RPMI fortified with 10% FBS), and pure FBS (100%) at the dilute concentration (100 mg/L), as indicated by the DLS analysis in **Figure 4.2.5**. However, the QDs presented a slightly larger hydrodynamic size when compared to the TEM measured size, such as the average diameter of 5.61 nm (PdI = 0.382) in Milli-Q water, 5.61 nm (PdI = 0.433) in cell culture medium (RPMI fortified with 10% FBS) and 4.84 nm (PdI = 0.497) in pure FBS (100%). Besides, different zeta potentials of -34.2 mV and -8 mV (**Figure 4.2.5**) were obtained in Milli-Q water and RPMI+10% FBS, respectively, for these QDs. This shift in ζ -potential toward neutral value in RPMI fortified with 10% FBS is attributed to the adsorption of metal ions present in cell culture medium on the surface of 3-MPA capped ZnSe:Mn²⁺ QDs.

Figure 4.2.5 - Particles size distribution histogram of ZnSe:Mn²⁺ QDs suspension in Milli-Q water (a), RPMI+ FBS (10%) cell culture medium (b), FBS (100%) (c), and Zeta potential in Milli-Q water (d) and RPMI+ FBS (10%) (e).



4.2.2. Photoluminescence study

The UV-visible absorption spectra (**Figure 4.2.6a**) of ZnSe host and ZnSe: x Mn²⁺ ($x = 5, 10, \text{ and } 15 \text{ mol\%}$) QDs show maximum absorption bands at around 402 (3.1 eV), 378 (3.8 eV), 382 (3.25 eV) and 391 nm (3.17 eV), respectively, corresponding to the first exciton transition, indicating the blue shift when compared to bulk ZnSe bandgap (460 nm (2.70 eV)) [107]. An obvious hypsochromic shift in the maximum exciton absorption band of the ZnSe matrix was observed after doping it with Mn²⁺. Additionally, a subtle bathochromic shift was observed in the transition exciton with increasing the concentration of dopant Mn²⁺ ions, manifesting the size-dependent quantum confinement effect in ZnSe after doping with Mn²⁺ ions. The excitation spectra (**Figure 4.2.6b**) of Mn²⁺ doped ZnSe were measured in chloroform at room temperature, monitoring emission at 584 nm from the ⁴T₁→⁶A₁ transition of Mn²⁺, which display high-intensity absorption band at 380 nm, attributing to the bandgap transition of ZnSe matrix.

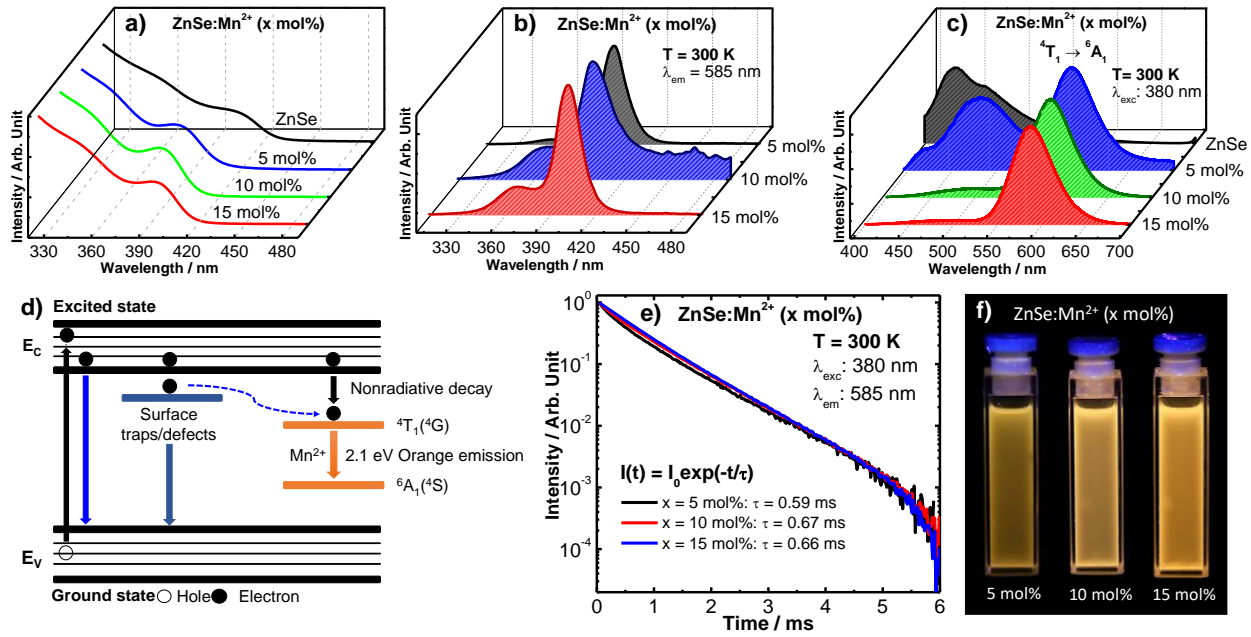
The emission spectra of Mn²⁺ doped ZnSe were measured in chloroform solution at room temperature while monitoring the excitation at 380 nm. The spectra (**Figure 4.2.6c**) exhibited three broad emission bands centered at 428 nm (2.9 eV), 465 nm (2.6 eV), and 584 nm (2.1 eV). The

emission band at 428 nm was attributed to the recombination of electron-hole pair at the bandgap of ZnSe host lattice [108], and the band centered at 465 nm was assigned to the radiative recombination of photogenerated charge carriers at the trap states due to the zinc-vacancy/surface defects [106], [109]. The high-intensity broad emission band centered at 584 nm was attributed to the pseudo-tetrahedral ${}^4T_1({}^4G) \rightarrow {}^6A_1({}^6S)$ radiative $3d^5$ -intraconfigurational transition of Mn^{2+} ion.

By exciting the ZnSe: Mn^{2+} QDs at 380 nm, in the bandgap of ZnSe, an exciton is generated. Recombination of this photogenerated exciton results in radiative decay (bandgap emission) while partly transfers energy to the $3d^5$ -intraconfigurational energy levels of Mn^{2+} ion (**Figure 4.2.6d**) that radiatively decay to the 6A_1 ground level. The $d-d$ transitions are usually spin-forbidden, presenting long luminescence lifetime (**Figure 4.2.6e**). However, it is highly sensitive to the surrounding chemical environment due to the strong ligand field effect. Accordingly, the emission band (from ${}^4T_1 \rightarrow {}^6A_1$ transition) varies from green to red region, depending upon the crystal field, size, and geometry of the host matrix. Thus, a slight redshift was observed from 584 to 587 nm when the concentration of dopant Mn^{2+} ions was increased from 5 to 15 mol%, due to the particle size-dependent crystal field effect [104], [108].

Nevertheless, the QDs with 10 and 15 mol% of Mn^{2+} concentrations showed an efficient bright yellow emission, as displayed by their aqueous solutions under UV irradiation lamp at $\lambda = 365$ nm (**Figure 4.2.1 and 4.2.6f**), suggesting them interesting candidates for the applications as nanomedicine. It is noteworthy that the intensity of the emission band assigned to the ${}^4T_1({}^4G) \rightarrow {}^6A_1({}^4S)$ transition was significantly enhanced when the molar concentration of the dopant Mn^{2+} ion was increased from 5 to 15 mol%. In contrast, the bandgap and trap-state emissions were considerably quenched. This result suggests efficient energy transfer from the ZnSe host lattice to the dopant Mn^{2+} ions [108] which is a signature of the incorporation of Mn^{2+} into the ZnSe matrix.

Figure 4.2.6 - UV-Visible absorption spectra (a), excitation spectra (b), emission spectra (c), partial energy level diagrams, blue color dashed arrow denotes energy transfer, and the blue, dark bluish, and yellow color downward wide arrows represent the radiative decays from bandgap, surface traps, and dopant Mn^{2+} ion, respectively (d), luminescence decay curves (e) and digital photograph (f) of $ZnSe:xMn^{2+}$ QDs under UV irradiation lamp ($\lambda = 365$ nm).



Luminescence decay curves: The radiative lifetime (τ) of ⁴T₁ metastable excited state of the Mn^{2+} ion (Figure 3e) was measured under bandgap excitation of ZnSe at 380 nm and emission at 584 nm from the ⁴T₁(⁴G) → ⁶A₁(⁴S) transition, to evaluate the effect of Mn^{2+} concentration on luminescence and corroboration of incorporation of dopant Mn^{2+} in ZnSe host lattice. The decay curves were subsequently well fitted with a mono-exponential function of $I(t) = I_0 \exp(-t/\tau)$, where $I(t)$ and I_0 are the luminescent intensities at a time, t and 0, respectively, and τ is the fluorescence lifetime. The effective lifetimes (τ) of $ZnSe:xMn^{2+}$ ($x = 5, 10,$ and 15 mol%) QDs (Figure 4.2.6e) were calculated to be approximately 0.59, 0.67, and 0.66 millisecond (ms), respectively. The observed longer lifetime (τ) for these QDs can be assigned to the radiative decay from the ⁴T₁ excited state to the ⁶A₁ fundamental energy level of the dopant Mn^{2+} ion, as reported earlier in the literature [110], [111]. This result confirmed the incorporation of Mn^{2+} in the ZnSe host lattice.

The QDs with 5 mol% of Mn^{2+} concentration exhibited the shortest luminescence lifetime (Figure 4.2.6e), probably due to the efficient emission at 465 nm from zinc-vacancy or surface

traps/defects that acts as trapping sites for photogenerated carriers which reduce the lifetime [112]. However, the emission from (${}^4T_1 \rightarrow {}^6A_1$) transition, in the QDs with 10 mol% of Mn^{2+} , is dominated considerably over the trap states emission (**Figure 4.2.3c**), indicating the efficient energy transfer from the ZnSe host to Mn^{2+} and hence the longer lifetime (0.67 ms) was observed. The partially shorter lifetime for the higher molar concentration of Mn^{2+} (15 mol%) displays the concentration-driven quenching. The exchange interaction between neighboring exchange-couple, Mn^{2+} pairs causes the partial relaxation of spin selection rule, the electric dipole transition is allowed, and hence the lifetime of Mn^{2+} is reduced [108].

4.3. Multicolor-tunable ZnSe:Eu²⁺/Mn²⁺@ZnS Core-Shell QDs

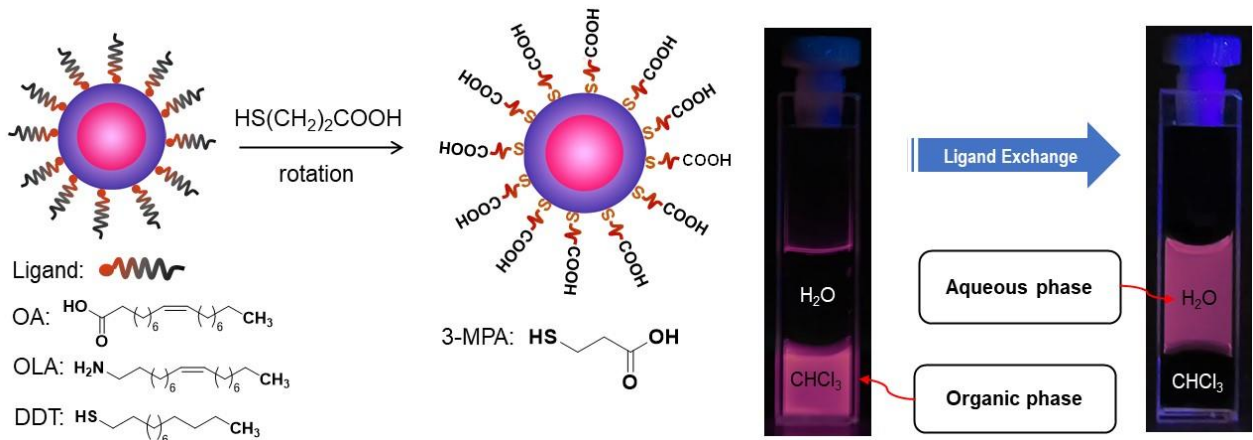
A series of unpassivated ZnSe:*x*Eu²⁺/*y*Mn²⁺ (*x* = 4, 8, and 12; *y* = 12 mol%) QDs and ZnS monolayers (ML) passivated ZnSe:*x*Eu²⁺/*y*Mn²⁺ (*x*, *y* = 12 mol%) and ZnSe:Eu²⁺ (4 mol%) core-shell QDs were prepared *via* organo-metals synthetic approach in non-coordinating solvent ODE and coordinating solvent/stabilizing agents OA/OLA/DDT under inert atmosphere, as schematically shown in **Figure 4.3.1**. The QDs presented color-tunable emission ranging from blue to red region of electromagnetic spectrum, depending on the relative concentration of Eu²⁺ to Mn²⁺ ion.

Figure 4.3.1 - Schematic illustration of cores ZnSe:*x*Eu²⁺/*y*Mn²⁺ (*x* = 4, 8, and 12; *y* = 0 and 12 mol%) core and ZnSe:*x*Eu²⁺/*y*Mn²⁺@ZnS core-shell QDs preparation.



However, the as-prepared ZnS passivated ZnSe:Eu²⁺/Mn²⁺ QDs were non aqueous soluble, as shown in **Figure 4.3.2**, and the colloidal stability of nanoscale materials in aqueous and biological media is a prerequisite for study *in vitro* and *in vivo* purposes. Therefore, the ZnS coated ZnSe:*x*Eu²⁺/*y*Mn²⁺ (*x*, *y* = 12 mol%) QDs were made water-soluble *via* surface functionalization with 3-MPA organic moiety through ligand exchange reaction, as schematically shown in **Figure 4.3.2**.

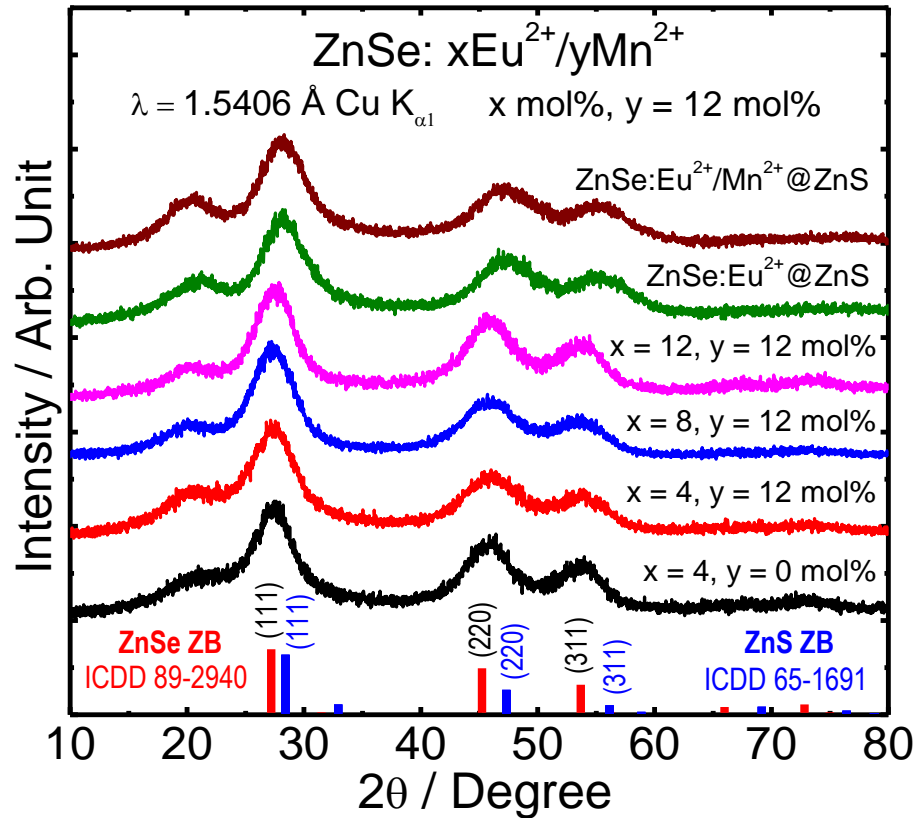
Figure 4.3.2 - Schematic illustration and digital photographs of phase transfer of ZnS passivated ZnSe: x Eu $^{2+}$, y Mn $^{2+}$ ($x, y = 12$ mol%) core-shell QDs solution from chloroform layer to water layer after ligand exchange reaction, under UV irradiation lamp ($\lambda = 365$ nm).



4.3.1. Physicochemical characterization

X-ray Diffraction: The XRD patterns of unpassivated ZnSe: x Eu $^{2+}$ / y Mn $^{2+}$ ($x = 4, 8,$ and $12; y = 12$ mol%) and ZnS passivated ZnSe: x Eu $^{2+}$, y Mn $^{2+}$ ($x, y = 12$ mol%) and ZnSe:Eu $^{2+}$ (4 mol%) core-shell QDs have been shown in **Figure 4.3.3**. The XRD patterns show diffraction peaks corresponding to the 2θ : (111) $\sim 27^\circ$, (220) $\sim 46^\circ$, and (311) $\sim 53^\circ$ of the ZnSe matrix and ZnSe: x Eu $^{2+}$ / y Mn $^{2+}$ ($x = 4, 8,$ and $12; y = 12$ mol%) QDs as well as core-shell ones, which are consistent with XRD pattern of cubic-zinc-blende crystalline phase of ZnSe (ICDD/PDF No: 89-2940) [113]. The XRD patterns of Eu $^{2+}$ /Mn $^{2+}$ doped ZnSe show no obvious phase change, traces of impurity phases or shift in peaks positions when compared to the diffraction peaks of ZnSe, indicating that Eu $^{2+}$ /Mn $^{2+}$ dopants are successfully incorporated without causing any significant change in the ZnSe host lattice.

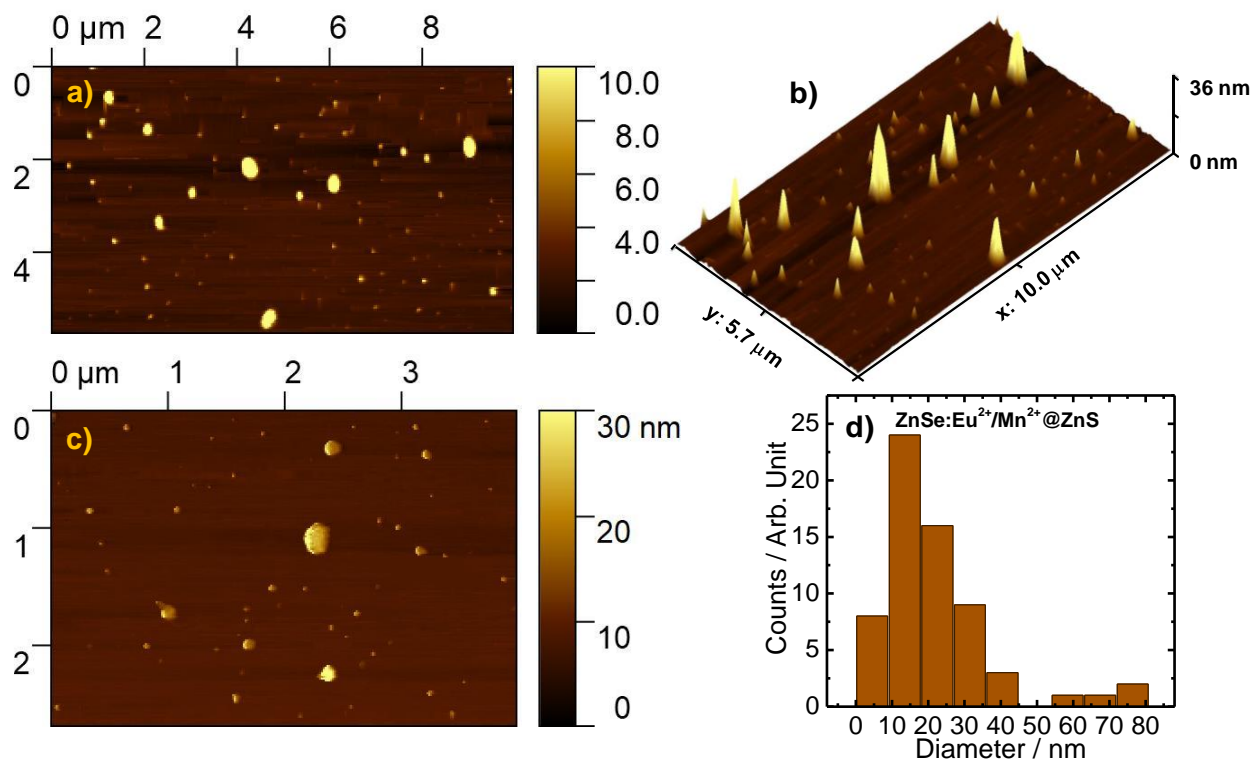
Figure 4.3.3 - X-ray diffraction patterns of ZnSe: $x\text{Eu}^{2+}/y\text{Mn}^{2+}$ ($x = 4, 8,$ and 12 ; $y = 0$ and 12 mol%) and ZnS passivated ZnSe: $x\text{Eu}^{2+},y\text{Mn}^{2+}$ ($x, y = 12$ mol%) and ZnSe: Eu^{2+} (4 mol%) and core-shell QDs.



The diffraction peaks exhibited substantial shift towards higher angle, closely to the values corresponding to cubic zinc-blende ZnS crystalline structure (ICDD/PDF No: 65-1691) [114], after passivating by ZnS shell, substantiating the effective coating of ZnSe: Eu^{2+} (4 mol%) and ZnSe: $x\text{Eu}^{2+},y\text{Mn}^{2+}$ ($x, y = 12$ mol%) QDs with ZnS monolayers. The broadening of diffraction peaks in all the XRD patterns is the clear manifestation that the QDs are ultra-small-sized nanocrystals.

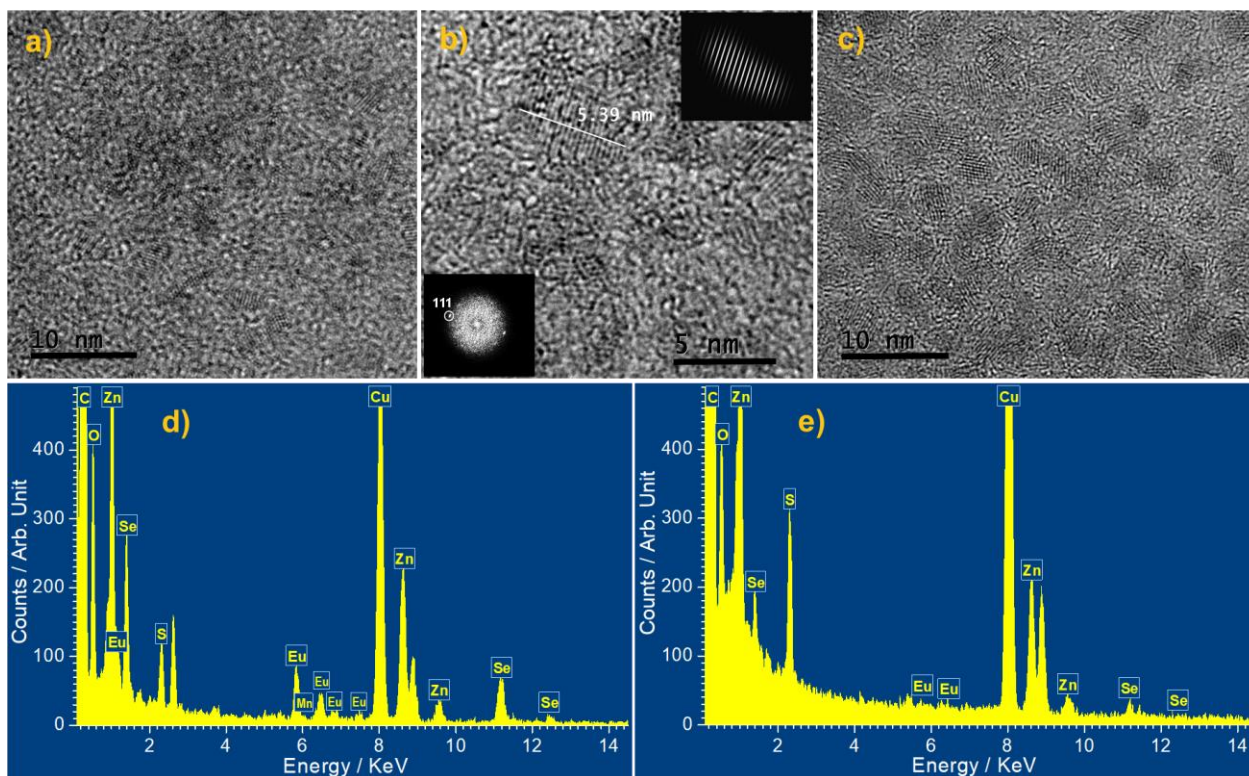
AFM and TEM images: Atomic force microscopy 2 and 3-dimensional (2 and 3D) images were obtained to determine the shape, morphology, average height, grain size distribution, and colloidal behavior of 3-MPA capped ZnSe: $x\text{Eu}^{2+},y\text{Mn}^{2+}$ @ZnS ($x, y = 12$ mol%) core-shell QDs in dilute aqueous dispersion (**Figure 4.3.4a-c**).

Figure 4.3.4 - AFM topography 2 and 3-dimensional images (a-c) and histogram of grain size distribution of ZnS passivated ZnSe: x Eu $^{2+}$, y Mn $^{2+}$ @ZnS ($x, y = 12$ mol%) core-shell QDs.



The images showed broad average height (Z-dimension) and size distribution of QDs predominantly in the range of >5 and <36 nm, as shown in **Figure 4.3.4b,d**. The average grain size of the majority of particles was found higher than that of the crystalline size measured by transmission microscopy images and dynamic light scattering (**Figure 4.3.5 and 4.3.6**), suggesting the aggregation of ultra-small nanocrystals of QDs to a certain extent in aqueous solution.

Figure 4.3.5 - HRTEM images and EDS spectra of $\text{ZnSe}:\text{xEu}^{2+},\text{yMn}^{2+}$ (a,b,d), and ZnS passivated $\text{ZnSe}:\text{xEu}^{2+},\text{yMn}^{2+}$ ($\text{x}, \text{y} = 12 \text{ mol}\%$) (c,e) QDs.



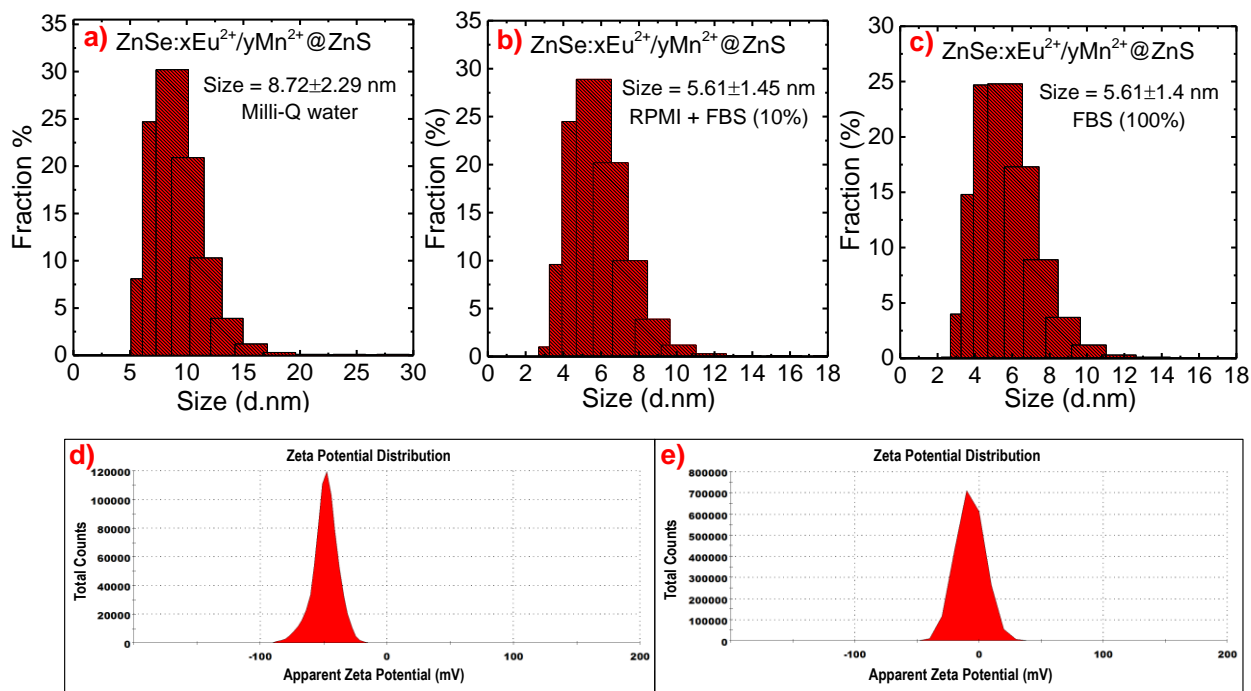
High-resolution TEM images of $\text{ZnSe}:\text{xEu}^{2+},\text{yMn}^{2+}$ ($\text{x}, \text{y} = 12 \text{ mol}\%$) QDs (**Figure 4.3.5a,b**) show ultra-small ellipse and non-spherical shapes nanocrystals with narrow size distribution and diameter of $\sim 5.3 \text{ nm}$, as depicted in **Figure 4.3.5b**. The diameter of the single nanocrystal was approximately measured in digital micrograph Gatan microscopy suite software, Gatan, Inc. The FFT pattern shows the diffraction spots of 111 that correspond to the 3.24 \AA interplanar spacing, confirming the presence of the cubic zinc-blende ZnSe crystalline structure, as depicted by the XRD pattern (**Figure 4.3.3**). In addition, HRTEM images of $\text{ZnSe}:\text{xEu}^{2+},\text{yMn}^{2+}@\text{ZnS}$ ($\text{x}, \text{y} = 12 \text{ mol}\%$) QDs (**Figure 4.3.5c**) exhibits roughly spherical shape nanocrystals, suggesting the coating of core $\text{ZnSe}:\text{xEu}^{2+}/\text{yMn}^{2+}$ with ZnS monolayers. To unravel the chemical composition and confirm the successful incorporation of $\text{Eu}^{2+}/\text{Mn}^{2+}$ dopants in ZnSe host lattice, energy-dispersive X-ray spectroscopy (EDS) analyses were carried out for both the $\text{ZnSe}:\text{xEu}^{2+},\text{yMn}^{2+}$ core and $\text{ZnSe}:\text{xEu}^{2+},\text{yMn}^{2+}@\text{ZnS}$ core-shell QDs. The EDS spectra (**Figure 4.3.5d and e**) clearly show the presence of Eu, Se, and Zn elements in core and appearance of dominant S element in core-shell nanocrystals when compared to the Se one in core-shell

nanoparticles, confirming the successful coating of $\text{ZnSe:xEu}^{2+},\text{yMn}^{2+}$ with ZnS monolayers (MLs). However, the Mn element was not apparently visualized in the EDS spectra to the overlapping of Mn $\text{K}_{\alpha 1-3}$ (5769.9-5900.3 eV) emission peaks with the high fluorescence intensity Eu $\text{L}_{\alpha 1,2}$ (5818.4-5849.5 eV) lines.

Hydrodynamic size and zeta potential: The dynamic light scattering (DLS) data of the ZnS coated $\text{ZnSe:xEu}^{2+},\text{yMn}^{2+}$ ($x, y = 12$ mol%) QDs were acquired in Milli-Q water, RPMI supplemented by FBS (10%), and pure FBS (100%) at a QDs concentration of 50 $\mu\text{g/mL}$, as shown in **Figure 4.3.6**. The DLS data presented good colloidal stability in all of the above media. However, the hydrodynamic size of QDs exhibited slightly large Z-average diameter of 8.721 nm ($\text{PdI} = 0.432$) in Milli-Q water when compared to that of 5.615 nm ($\text{PdI} = 0.845$) in RPMI supplemented with FBS (10%) and 5.612 nm ($\text{PdI} = 0.634$) in pure FBS (100%). This discrepancy can be explained by agglomeration and aggregation of ultra-small sized QDs in Milli-Q water whereas stabilization by protein corona formation in RPMI supplemented by FBS (10%) and pure FBS (100%), consequently enhancing their colloidal stability in biological media.

The zeta potential measurements demonstrated values of -48.4 ± 10.0 mV in water and -6.93 ± 11.6 mV in RPMI supplemented by FBS (10%) at QDs concentration of 50 $\mu\text{g/mL}$, as depicted in **Figure 4.3.6d and e**. This change in zeta-potential value from negative to neutral in cell culture medium suggests the adsorption of proteins and cations of salts to the negatively charged surface QDs.

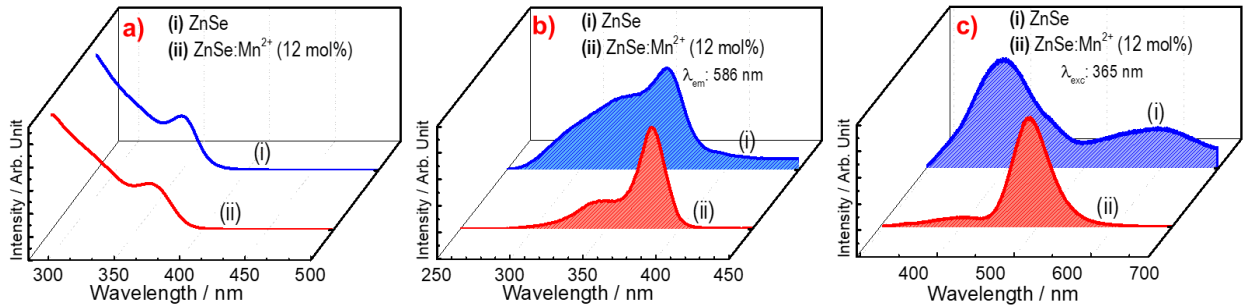
Figure 4.3.6 - Size-distribution histogram (by number) of ZnSe:xEu²⁺,yMn²⁺@ZnS (x, y = 12 mol%) core-shell QDs in (a-c) Milli-Q water, FBS (10%) supplemented RPMI, and pure FBS (100%) media and (d and e) zeta potential in water and FBS (10%) supplemented RPMI media, respectively.



4.3.2. Photoluminescence study

UV-visible absorption and luminescence spectra of ZnSe:xEu²⁺/yMn²⁺ (x = 4, 8, and 12; y = 12 mol%) and ZnS coated ZnSe:xEu²⁺/yMn²⁺ core-shell QDs are shown in **Figure 4.3.7-4.3.9**. The first excitonic peak positioned at 344 nm for the ZnSe: Eu²⁺ (4 mol%) QDs is slightly blue-shifted when compared to the absorption spectrum of non-doped ZnSe centered at 350 nm (**Figure 4.3.7a**), which can be explained by quantum confinement effect. However, the absorption edge peaked at 343, 347, and 349 nm (**Figure 4.3.8a**) presented consistently and slightly red-shift after co-doping with fixed amount of Mn²⁺ (12 mol%) and gradually increasing concentration of Eu²⁺ in ZnSe:xEu²⁺,yMn²⁺ (x = 4, 8, and 12; y = 12 mol%) QDs, respectively. The sharper absorption bands exhibited by unpassivated QDs suggest the formation of narrower particle size distribution.

Figure 4.3.7 - UV-visible absorption spectra (a), excitation (b), and emission spectra (c) of ZnSe and ZnSe:Mn²⁺ (12 mol%) QDs.

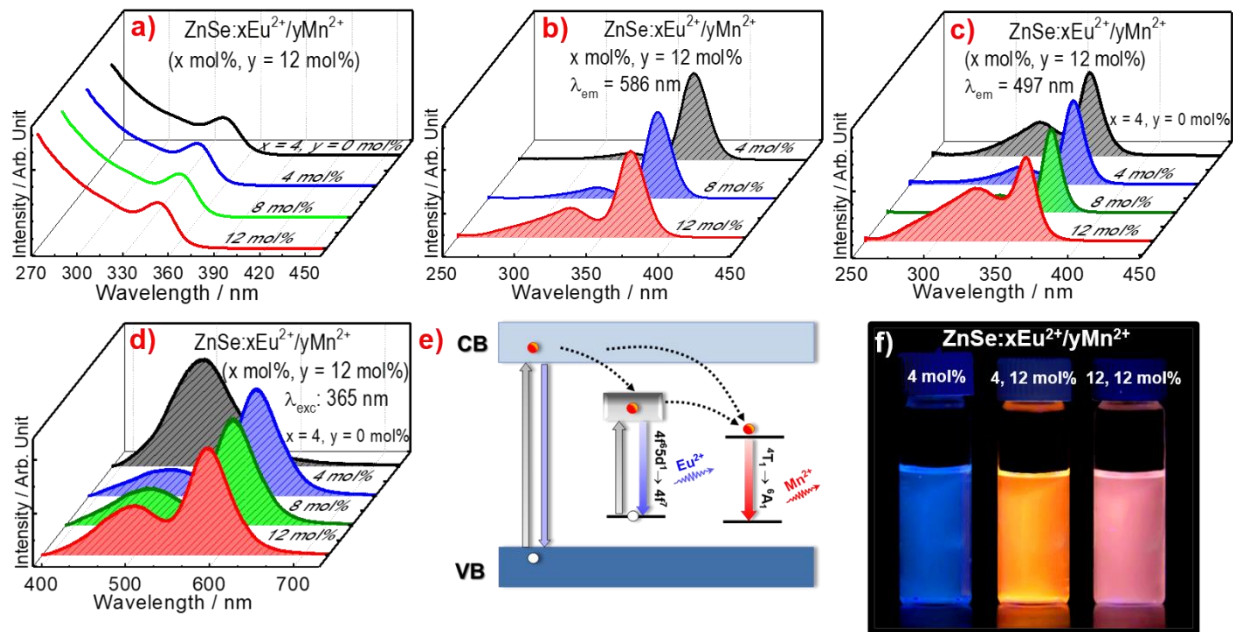


The luminescence spectra (**Figures 4.2.6b and c**) of Mn²⁺ doped ZnSe have already explained in **section 4.2.2**. The excitation spectra of Eu²⁺/Mn²⁺ doped ZnSe show a broad absorption band at 365 nm, assigned to the bandgap transition of the ZnSe matrix (**Figure 4.3.8b and c**). Monitoring the emission at 497 nm, the excitation spectra presented a similar profile to that of excitation spectra recorded by monitoring the emission at 586 nm, as shown in **Figure 4.3.8b-c**. However, the excitation band showed a slight difference in the intensity and broadness towards lower wavelength for the Eu²⁺/Mn²⁺ doped ZnSe QDs when compared to the individually Mn²⁺ doped one, manifesting the possibility of interconfigurational transition between 4f⁷ ground state and crystal-field split 4f⁶5d configuration of Eu²⁺ ion.

By exciting at 365 nm, the emission spectrum of non-doped ZnSe (**Figure 4.3.7c**) exhibited asymmetric and irregular broadband extending from 390 to 774 nm. The prominent emission band positioned at 497 nm can be assigned to the photo-generated electron-hole pair recombination, and the low-intensity broad emission can be attributed to the radiative recombination of surface traps/defects. However, the emission spectrum of ZnSe QDs (**Figure 4.3.8a**) exhibited a blue-green broad emission band peaked at 499 nm after co-doping with Eu²⁺ (4 mol%), corresponding to the parity and spin-allowed 4f⁶5d¹→4f⁷ transition state of Eu²⁺ ions. Similarly, only Mn²⁺ doped presented symmetric orange-emitting peak centered at 586 nm originating from the spin-forbidden ⁴T₁(⁴G) →⁶A₁(⁶S) transition of tetrahedrally coordinated Mn²⁺ ion (**Figure 4.3.7c**). However, a significant impact was noticed on the mutual emission intensity of Eu²⁺ and Mn²⁺ ions when they were incorporated together into ZnSe lattice. The emission intensity of Mn²⁺ dramatically enhanced while that of Eu²⁺ reduced concurrently. The emission spectra (**Figure 4.3.8d**) of ZnSe:xEu²⁺,yMn²⁺ (x = 4; y = 12 mol%) presented two distinct emission bands: a weak blue-green

emission band positioned at around 499 nm and a high-intensity orange emission band centered at 586 nm.

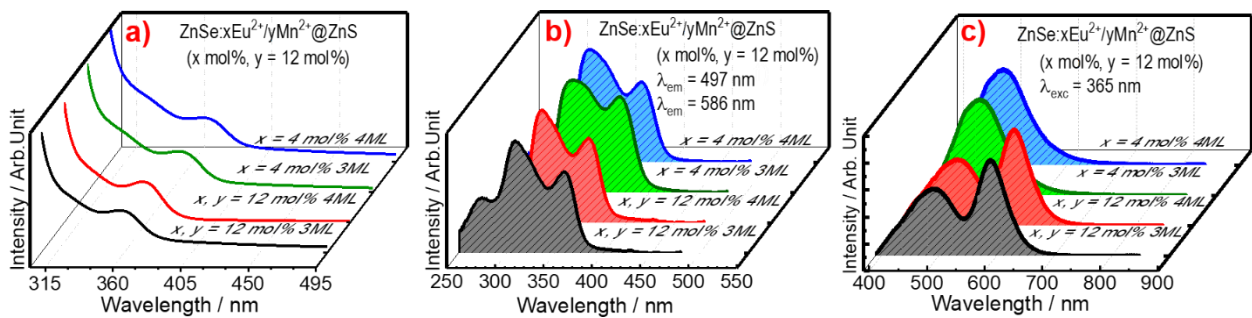
Figure 4.3.8 - UV-visible absorption spectra (a), excitation spectra (b-c), emission spectra (d), schematic representation of energy level diagram, grey arrow denotes photogenerated electron-hole pair (exciton), right blue arrow represents radiative recombination of exciton, second right black denotes interconfigurational transition from $4f^7$ ground level to the $4f^65d^1$ state of the Eu^{2+} ion, black dashed arrows indicate energy transfer to dopant impurities, second right blue and red arrows illustrate the radiative decays for Eu^{2+} and Mn^{2+} ions, respectively (e), and digital photographs of $\text{ZnSe}:\text{Eu}^{2+}$ (4mol%) and $\text{ZnSe}:\text{xEu}^{2+},\text{yMn}^{2+}$ ($x = 4$ and 12 ; $y = 12$ mol%) QDs, under UV irradiation lamp at $\lambda = 365$ nm (f).



The emission intensity of Eu^{2+} enhanced consistently and proportionally when its concentration was gradually increased while maintaining the content of Mn^{2+} (12 mol%) unchanged, as shown in **Figure 4.3.8d**. However, the fluorescence emission of QDs was quenched significantly when the amount of Eu^{2+} exceeded 12 mol%. Ironically, at the same concentrations 12 mol% of each Eu^{2+} and Mn^{2+} , the blue-green emission around 499 nm was found comparatively much weaker than that of orange emission located at 586 nm, indicating the energy transfer from Eu^{2+} to Mn^{2+} or some non-radiative pathway. Noteworthy, no additional emission peaks arising from 4f-intraconfigurational transitions of Eu^{3+} ions were observed in the emission spectra of all the respective QDs, confirming the successful reduction of $\text{Eu}^{3+} \rightarrow \text{Eu}^{2+}$.

The excitation spectra of all QDs, whether co-doped separately or jointly with $\text{Eu}^{2+}/\text{Mn}^{2+}$, presented a similar profile of the dominant absorption band extending between 360-370 nm assigned to the bandgap transition of ZnSe, which suggests that the excitation of Eu^{2+} and Mn^{2+} impurities occur *via* efficient energy transfer from the ZnSe host lattice. The emission spectra of all $\text{Eu}^{2+}/\text{Mn}^{2+}$ doped ZnSe QDs presented dominant emission band centered at 586 nm when compared to the emission band located at 499 nm, suggesting an efficient energy transfer (**Figure 4.3.8e**) from Eu^{2+} ion *via* non-radiative decay to the excited energy levels of Mn^{2+} ion. Nevertheless, the $\text{Eu}^{2+}/\text{Mn}^{2+}$ doped ZnSe QDs showed tunable emission by varying the concentration of dopant Eu^{2+} ion, as shown in **Figure 4.3.8f**.

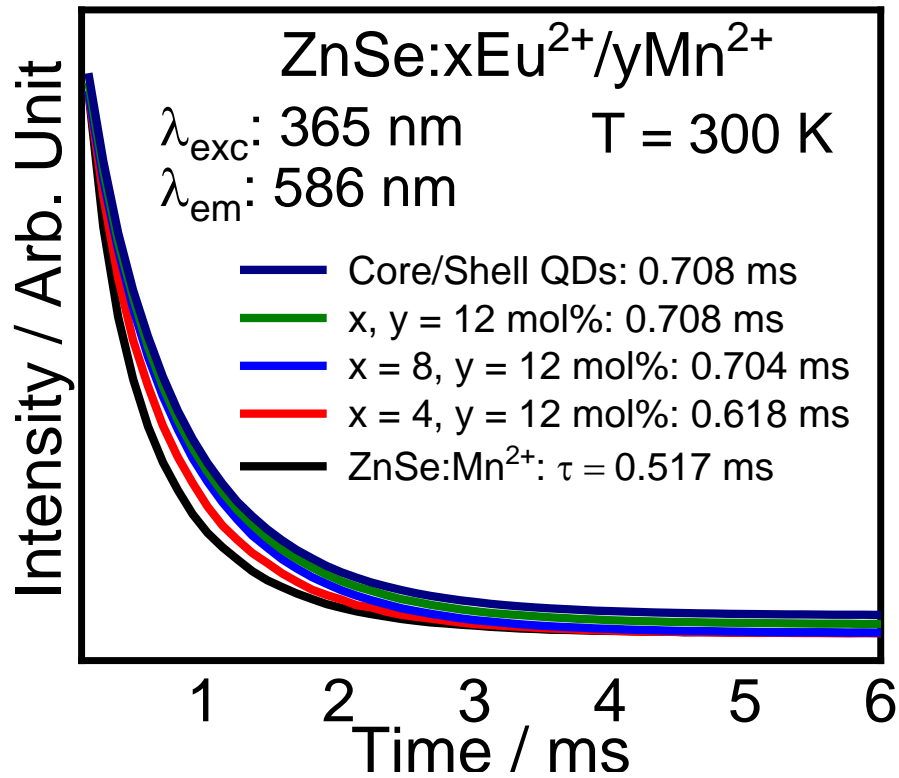
Figure 4.3.9 - UV-visible absorption spectra (a), excitation spectra (b), and emission spectra of ZnS (3 and 4 MLs) passivated ZnSe: Eu^{2+} (4 mol%) and ZnSe: $x\text{Eu}^{2+},y\text{Mn}^{2+}$ ($x, y = 12$ mol%) core-shell QDs (c). The abbreviation “ML” in the inset stands for the monolayers of ZnS shell materials.



However, after passivating with ZnS, the absorption spectra of Eu^{2+} (4mol%), and $x\text{Eu}^{2+}$ and $y\text{Mn}^{2+}$ ($x, y = 12$ mol%) co-doped ZnSe QDs (**Figure 4.3.9a**) exhibited significant red-shift, which can be explained by strain-induced partial leakage of exciton into ZnS shell caused by the lattice mismatch (ca. 5%) [115] between ZnSe and ZnS. The emission spectrum of ZnSe: Eu^{2+} @ZnS (4 mol%) core-shell QDs (**Figure 4.3.9c**) presented a slight blue-shift that can be interpreted by crystal field splitting generated in the local environment due to the lattice mismatch between ZnSe core and ZnS shell. Additionally, emission spectra of the ZnS passivated ZnSe: $x\text{Eu}^{2+},y\text{Mn}^{2+}$ ($x, y = 12$ mol%) QDs show similar profiles, as observed for un-passivated ones, with dominant orange emission band from the ${}^4\text{T}_1({}^4\text{G}) \rightarrow {}^6\text{A}_1({}^4\text{S})$ transition of Mn^{2+} ion.

Luminescence decay curves: The decays curves (**Figure 4.3.10**) show the effect of Eu^{2+} ion concentration on the radiative lifetime (τ) of ${}^4\text{T}_1$ metastable excited state of the Mn^{2+} ions. The decay curves were measured while monitoring the excitation at 365 nm and emission at 584 nm assigned to the ${}^4\text{T}_1({}^4\text{G}) \rightarrow {}^6\text{A}_1({}^4\text{S})$ transition state of Mn^{2+} . They were subsequently well fitted with a mono-exponential function of $I(t) = I_0 \exp(-t/\tau)$, where $I(t)$ and I_0 are the luminescent intensities at time t and 0, respectively, and τ is the fluorescence lifetime. The effective lifetime (τ) of ZnSe:Mn^{2+} (12 mol%) was calculated to be 0.517 millisecond (ms). However, after codoping with Eu^{2+} , the lifetime of Mn^{2+} at the same concentration increased with increasing the content of Eu^{2+} and was recorded to be approximately 0.618, 0.704 and 0.708 ms for the $\text{ZnSe:xEu}^{2+},y\text{Mn}^{2+}$ ($x = 4, 8, \text{ and } 12; y = 12 \text{ mol\%}$) QDs, respectively, (**Figure 14.3.0**). Besides, no obvious change was observed in the lifetime (0.70 ms) of $\text{ZnSe:xEu}^{2+},y\text{Mn}^{2+}$ ($x, y = 12 \text{ mol\%}$) after coating by ZnS, suggesting the successful passivation of QDs without causing stress-induced nonradiative recombination. The observed longer lifetime (τ) for the QDs can be due to the energy transfer from Eu^{2+} ion acting as activators to Mn^{2+} sensitizer based on the spectral overlap of the broad emission band of Eu^{2+} and excitation spectra of Mn^{2+} in ZnSe lattice [116], [117]. Additionally, the substantial depreciation in the intensity of Eu^{2+} emission compared to the emission of Mn^{2+} at the same concentration of each 12 mol% further corroborates the energy transfer (**Figure 4.3.8**) from Eu^{2+} to Mn^{2+} ions.

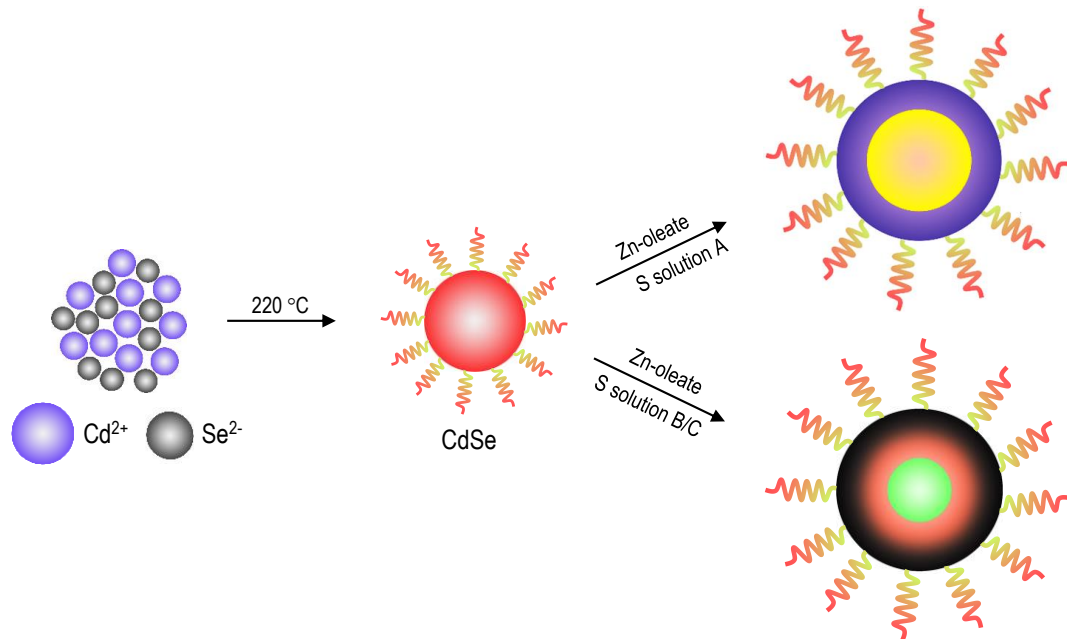
Figure 4.3.10 - Luminescence decay curves and lifetimes of representative $\text{ZnSe}:x\text{Eu}^{2+},y\text{Mn}^{2+}$ ($x = 4, 8, \text{ and } 12; y = 12 \text{ mol}\%$) and $\text{ZnSe}:x\text{Eu}^{2+},y\text{Mn}^{2+}@\text{ZnS}$ ($x, y = 12 \text{ mol}\%$) samples monitored by excitation at 365 nm and emission at 586 nm. The inset shows the variation of lifetime of Mn^{2+} based on increasing the content of Eu^{2+} .



4.4. Color-tuning *via* interfacial alloying in CdSe/ZnS nanocrystals

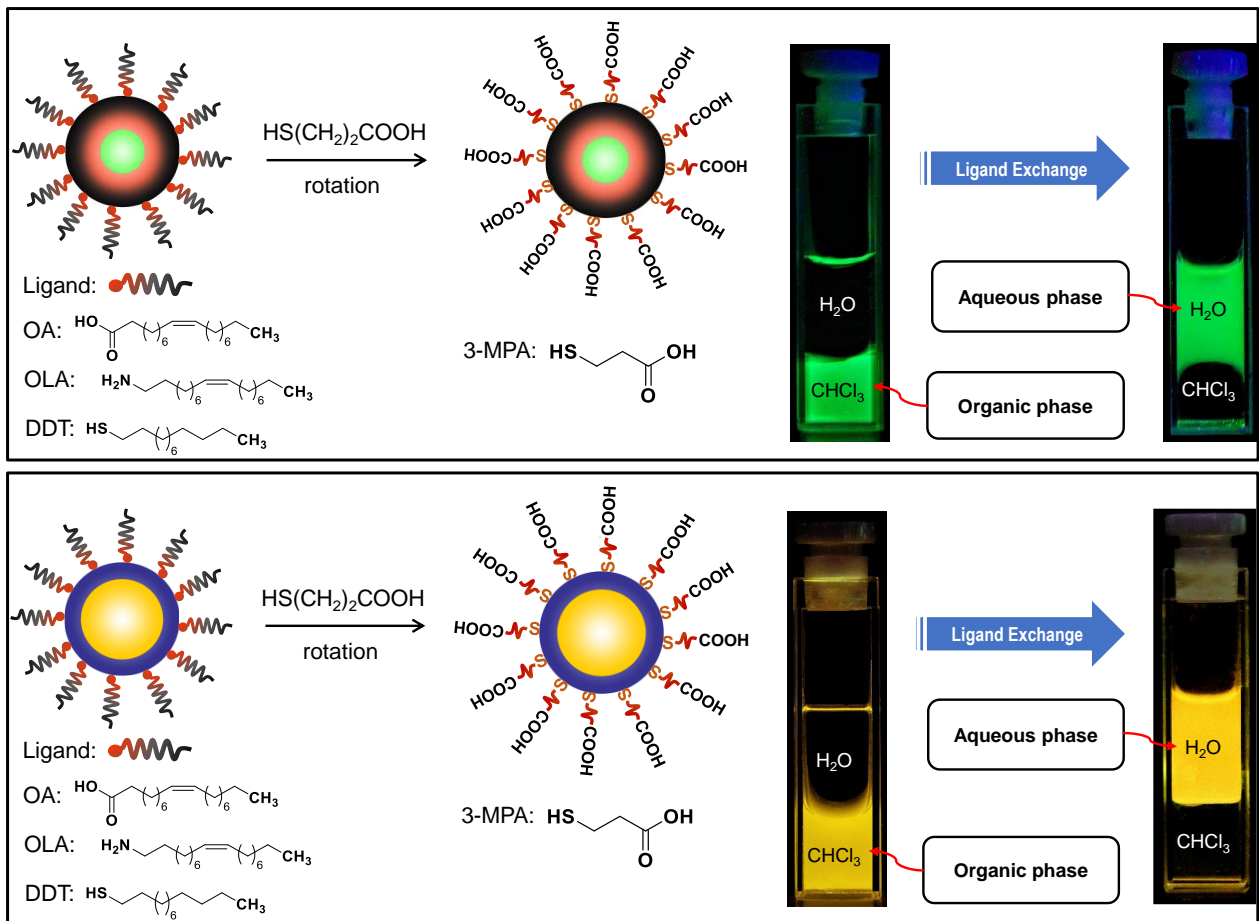
A series of different types of orange-emitting (CdSe/ZnS)_A, green-emitting, (CdSe/ZnS)_B, and blue-emitting (CdSe/ZnS)_C core-shell QDs were synthesized *via* the organo-metals procedure in a non-coordinating solvent ODE and coordinating solvent/stabilizing agents OA/OLA/DDT, as shown in **Figure 4.4.1**. It should be noted that the prepared (CdSe/ZnS)_A, (CdSe/ZnS)_B, and (CdSe/ZnS)_C core-shell QDs were named after sulfur precursor solutions A, B, and D used in syntheses of these quantum dots.

Figure 4.4.1 - Schematic illustration of nucleation processes of core CdSe and preparation of (CdSe/ZnS)_A, (CdSe/ZnS)_B, and (CdSe/ZnS)_C core-shell QDs.



As usual, the prepared quantum dots were soluble in an organic solvent, according to the adopted synthesis method, and were non-biocompatible to investigate for biological applications. Therefore, the (CdSe/ZnS)_A and (CdSe/ZnS)_B core-shell QDs were functionalized with 3-MPA through ligand exchange procedure, rendering them aqueous soluble. The representative scheme and digital photographs of the QDs before and after treatment with hydrophilic 3-MPA ligand have been shown in **Figure 4.4.2**.

Figure 4.4.2 - Schematic illustration and digital photographs of $(\text{CdSe/ZnS})_A$ (top) and $(\text{CdSe/ZnS})_B$ (bottom) core-shell QDs solutions phase transfer from chloroform layer to water layer after treatment with 3-MPA ($\text{HS}(\text{CH}_2)_2\text{COOH}$) ligand, under irradiation of UV lamp ($\lambda = 365 \text{ nm}$).

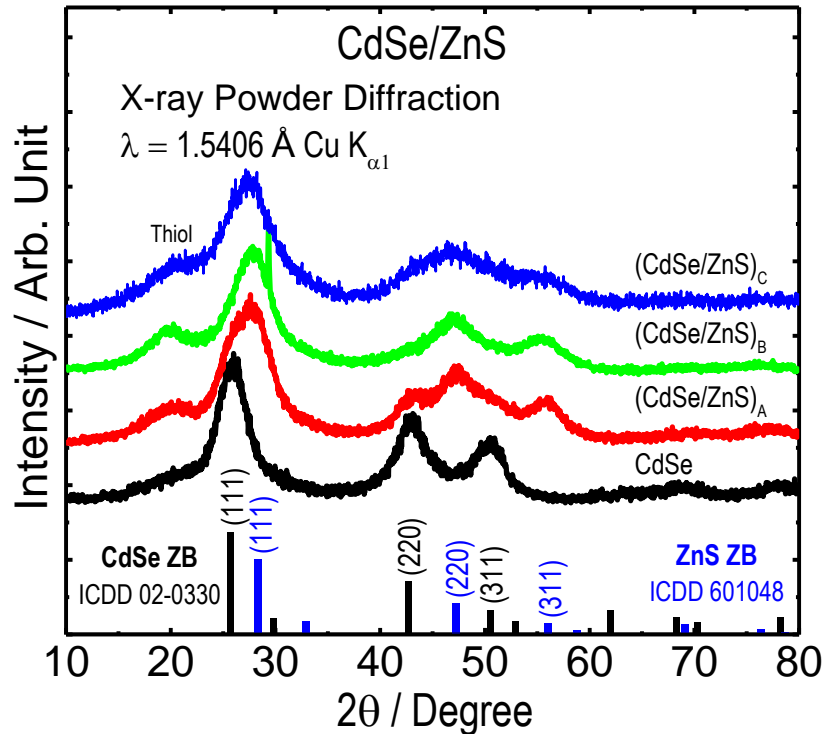


4.4.1. Physicochemical characterization

X-ray Diffraction: The XRD patterns of an un-passivated CdSe [113] display characteristic diffraction peaks predominantly at 2θ : (111) $\sim 26^\circ$, (220) $\sim 43^\circ$ and (311) $\sim 50^\circ$, corresponding to the zinc-blende crystal lattice of CdSe (ICDD/PDF No. 02-0330), as shown in **Figure 4.4.3**. After passivating with ZnS, the reflections for CdSe lattice were attenuated significantly in the three different diffractograms of $(\text{CdSe/CdS})_A$, $(\text{CdSe/ZnS})_B$, and $(\text{CdSe/ZnS})_C$, and the diffraction peaks were distinctly shifted towards larger 2θ angles, almost consistent with the diffraction peaks of zinc-blende [114] crystal lattice of ZnS (ICDD/PDF No. 65-1691). The CdSe in $(\text{CdSe/ZnS})_A$ presented broad diffraction peak at 2θ of $\sim 26^\circ$ and slightly resolved peak at 2θ value of $\sim 43^\circ$, indicating the intactness and consistency of core CdSe lattice in the core-shell QDs. The broadening

of diffraction peaks in core-shell QDs reveals the convolution of reflections originating from CdSe and ZnS, as previously reported for CdSe/ZnS core-shell QDs [118].

Figure 4.4.3 - XRD patterns of unpassivated CdSe and 3MLs of ZnS passivated orange-emitting (CdSe/ZnS)_A, green-emitting (CdSe/ZnS)_B, and blue-emitting (CdSe/ZnS)_C core-shell QDs.

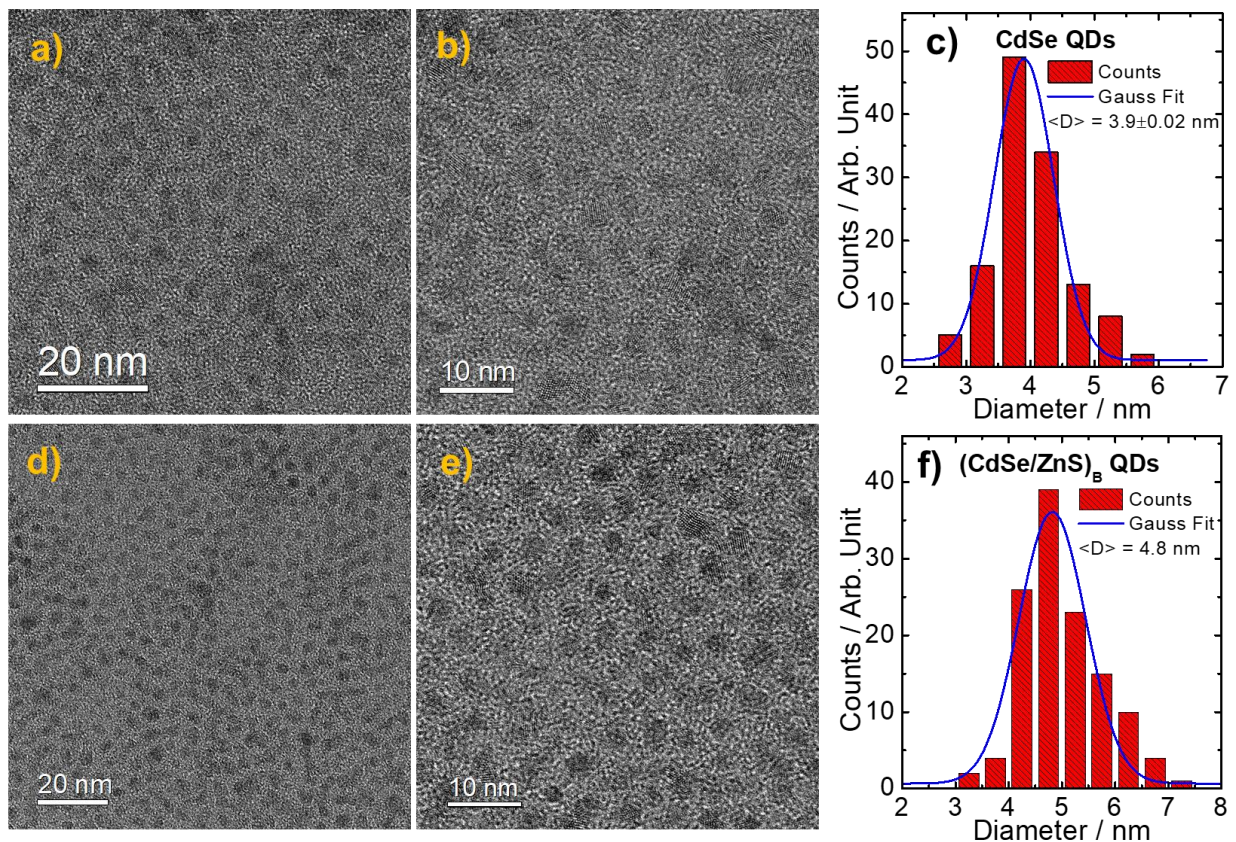


However, all the diffractions peaks of the (CdSe/ZnS)_B QDs were observed consistent with the zinc-blend ZnS with slight broadening towards that of CdSe lattice, suggesting the compression or core/alloy formation and considerable concomitant passivation by ZnS, as it is evident from the substantial blue-shift in the fluorescence (**section 4.4.2**). In contrast, the (CdSe/ZnS)_C exhibited broad peaks related to the diffraction pattern of ZnS. No distinguishable reflections from CdSe lattice were observed, suggesting the formation of interfacial alloy in core-shell QDs. This can be further corroborated by the extensive blue-shift (**section 4.4.2**) and the appearance of two excitonic and two emission peaks in the UV-visible absorption and emission spectra, corresponding to interfacial alloy and the remaining core. Conclusively, the apparent difference in the features of diffraction peaks for different samples is the hallmark of different QDs formation by varying the relative volumes of DDT:OLA, which can be further explored by photoluminescence spectroscopy.

It is noteworthy that the apparent increase in FWHM of diffraction peaks and the pronounced shift towards larger 2θ angles for CdSe/ZnS indicate the epitaxial growth of ZnS on CdSe. After passivation, the X-ray diffraction patterns exhibit distinct transformation from CdSe towards zinc-blend crystal structure of ZnS, substantiating the formation of ZnS during CdSe/ZnS synthesis.

TEM images: High-resolution TEM images of the core CdSe quantum dots (**Figure 4.4.4a,b**) show ultra-small roughly spherical shapes nanocrystals with narrow size distribution and dominant average diameter of ~ 3.9 nm, as deduced from the histogram of the particles size distribution (**Figure 4.4.4c**). In addition, the TEM images of the green-emitting core-shell (CdSe/ZnS)_B QDs manifested roughly spherical shape nanocrystals with an average diameter of ~ 4.8 nm (**Figure 4.4.4d-f**), suggesting the epitaxial growth of ZnS on the surface of CdSe with an approximate thickness of ~ 0.9 nm. The average diameters for both the CdSe and (CdSe/ZnS)_B were obtained by counting more than one hundred and twenty nanoparticles, using image J free software and nonlinearly curve fitting (Gauss fit) in origin 8.5.

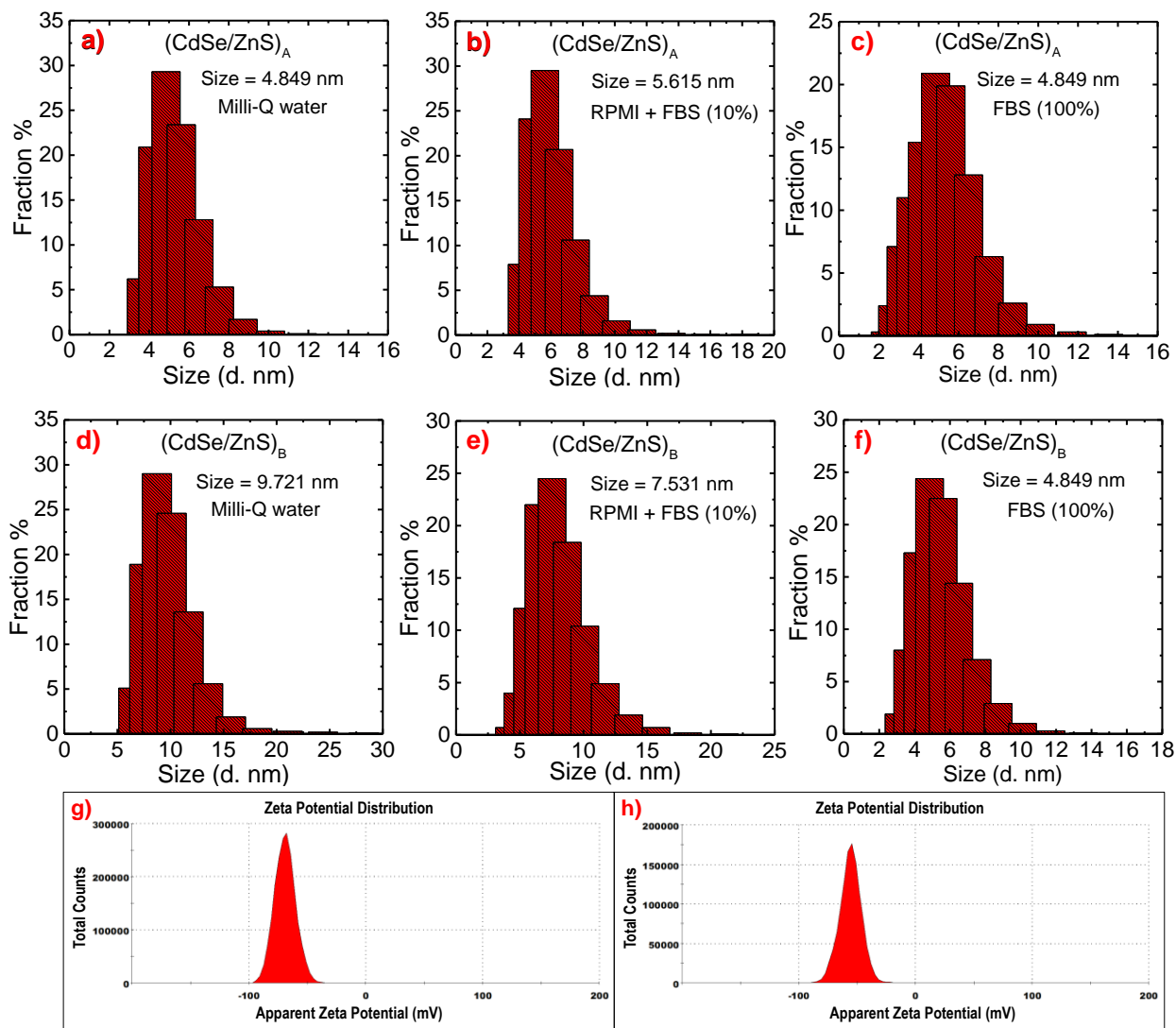
Figure 4.4.4 - HRTEM images (different magnifications) and histogram of particles size distributions of the core CdSe (a-c) and green-emitting core-shell (CdSe/ZnS)_B (d-f) QDs.



Hydrodynamic size and zeta potential: The dynamic light scattering data of orange-emitting (CdSe/ZnS)_A and green-emitting (CdSe/ZnS)_B core-shell QDs (**Figure 4.4.5**) was acquired in various media at a final concentration of 50 µg/mL. The QDs showed different hydrodynamic size in different solvent systems. The average diameter for the (CdSe/ZnS)_A QDs was found to be 4.849 nm (PdI = 1.00) in Milli-Q water, 5.615 nm (PdI = 0.571) in FBS (10%) supplemented RPMI, and 4.849 nm (PdI = 0.613) in pure FBS (100%), as shown in **Figure 4.4.5a-c**. Similarly, green-emitting (CdSe/ZnS)_B (**Figure 4.4.5d-f**) presented hydrodynamic size of 9.721 nm (PdI = 0.375) in Milli-Q water, 7.531 nm (PdI = 0.491) in FBS (10%) supplemented RPMI, and 4.849 nm (PdI 0.655) in pure FBS (100%).

The Z-average diameter of orange-emitting and green-emitting QDs exhibited a spontaneous reduction in FBS (10%) supplemented RPMI and pure FBS (100%) media, respectively, as compared to that of acquired in Milli-Q water medium. This propensity to shrinkage can be explained by QDs stabilization and shielding against the aggregation and agglomeration by the proteins adsorbed on the surface of QDs. The zeta potential for both QDs was measured in Milli-Q water at a final concentration of 50 µg/mL. The (CdSe/ZnS)_A showed zeta potential value of -68.9 ± 8.92 mV and (CdSe/ZnS)_B -55.8 ± 9.22 mV, respectively, as depicted in **Figure 4.4.5a-b**.

Figure 4.4.5 - Size-distribution histogram of orange-emitting $(\text{CdSe/ZnS})_A$ (a-c) and green-emitting $(\text{CdSe/ZnS})_B$ (d-f) core-shell QDs in Milli-Q water, FBS (10%) supplemented RPMI, and pure FBS (100%) media (a-c). Zeta potential of $(\text{CdSe/ZnS})_A$ (g) and $(\text{ZnSe/ZnS})_B$ (h) core-shell QDs in Milli-Q water.



4.4.2. Photoluminescence study

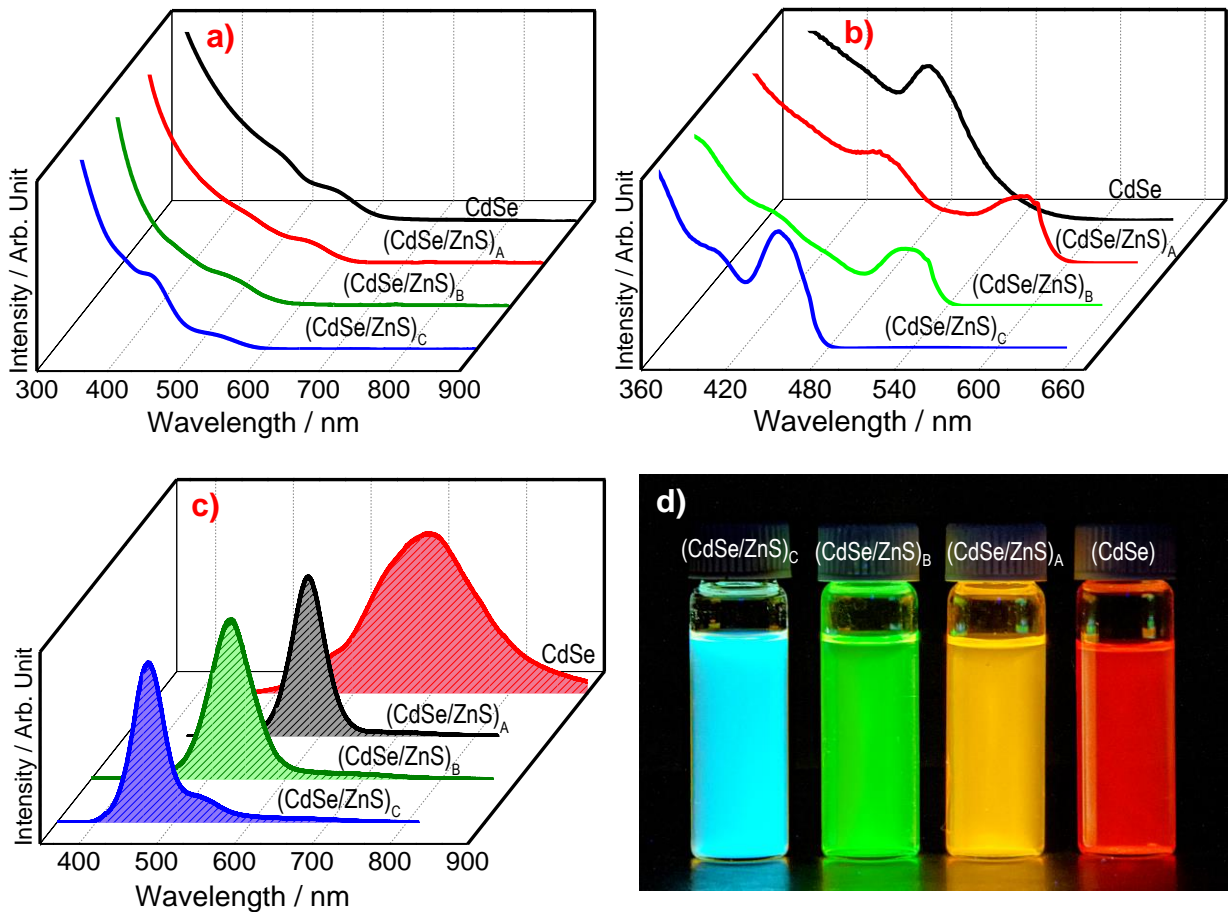
The UV-visible absorption and luminescence spectra of $(\text{CdSe/ZnS})_A$, $(\text{CdSe/ZnS})_B$, and $(\text{CdSe/ZnS})_C$ core-shell QDs are shown in **Figure 4.4.6**. The UV-visible absorption spectrum of CdSe exhibited the first excitonic absorption peak at 552 nm, as shown in **Figure 4.4.6a**. The luminescent spectra presented two emission bands: less intense bandgap emission positioned at 576 nm and a highly intense nonsymmetric broad emission band around 695 nm (**Figure 4.4.6c**), originating from the lattice defects/traps. However, post-passivation by ZnS shell, the broad

emission band from the defects of CdSe was vanished, accompanying a dramatic enhancement in the band-edge emission. Interestingly, by varying the relative ratios of DDT:OLA from 1:0 to 1:1 and 0:1, designated as solutions A, B, and C, the first excitonic peak and the emission band of $(\text{CdSe/ZnS})_A$ is red-shifted and then significantly blue-shifted in $(\text{CdSe/ZnS})_B$ and $(\text{CdSe/ZnS})_C$ core-shell QDs.

The UV-visible absorption and emission spectra of $(\text{CdSe/ZnS})_A$ (**Figure 4.4.6a-c**) slightly red-shifted, such as ~ 564 nm (band-edge absorption) and ~ 585 nm (emission), compared to that of CdSe after using solution A as S precursor for the epitaxial growth of 3 MLs of ZnS. The concomitant redshift is a signature of successful epitaxial growth of ZnS without alloying or at least not complete alloying between core and shell. Additionally, the band-edge emission enhanced significantly while the broad emission band vanished completely, indicating that most of the vacancies and trap sites are passivated after being overcoated by ZnS. The slight bathochromic shift in the absorption spectrum can be explained by partial leakage of the electronic wave function into ZnS over-coating [119] due to interfacial strain induced by the large lattice mismatch (ca. 12%) between CdSe and ZnS lattice parameters.

Contrary, the absorption and emission spectra of $(\text{CdSe/ZnS})_B$ (**Figure 4.4.6a-c**) exhibited considerable blue-shift, corresponding to the first excitonic absorption peak around 505 nm and emission centered at 530 nm, which are not consistent with either core or shell materials. This extensive blue-shift in the absorption and emission spectra can be attributed to the shrinking of the core induced as a result of interfacial alloying $(\text{Cd}_1\text{Zn}_{1-x}\text{Se})$ at the heterointerface (**Figure 4.4.1**) due to the interionic diffusion between CdSe and ZnS phases [120]. The alloy formation is usually embodied because of high temperature during synthesis that causes interdiffusion or rapid cations exchange of Cd^{2+} and Zn^{2+} at the core-shell interface and replace the Cd by Zn to form a structure, usually characterized as $(\text{Cd}_x\text{Zn}_{1-x})\text{Se}_x\text{S}_{1-x}$ [121]–[123]. However, $(\text{CdSe/ZnS})_C$ presented two absorption bands: the first unresolved excitonic peak positioned around 530 nm, extending towards lower energy, and another prominent excitonic absorption peak around 440 nm.

Figure 4.4.6 - UV-visible absorption spectra (a), excitation spectra (b), emission spectra (c), and photographs under UV light (d) of CdSe, orange-emitting (CdSe/ZnS)_A, green-emitting (CdSe/ZnS)_B, and blue-emitting (CdSe/ZnS)_C core-shell QDs.



Similarly, the emission spectrum of (CdSe/ZnS)_C QDs consists of two emission bands centered at 468 and 534 nm, as shown in **Figure 4.4.6a-c**. The prominent excitonic absorption and blue emission bands can be assigned to the exciton localized in the interfacial alloy. It is known that an intermediate bandgap is fashioned when two semiconductor materials of different bandgaps are intermixed to form an alloy. Therefore, the extensive blue-shift can occur as a result of the formation of a larger intermediate bandgap between wide-bandgap ZnS (3.7 eV) and smaller bandgap CdSe (1.75 eV) materials.

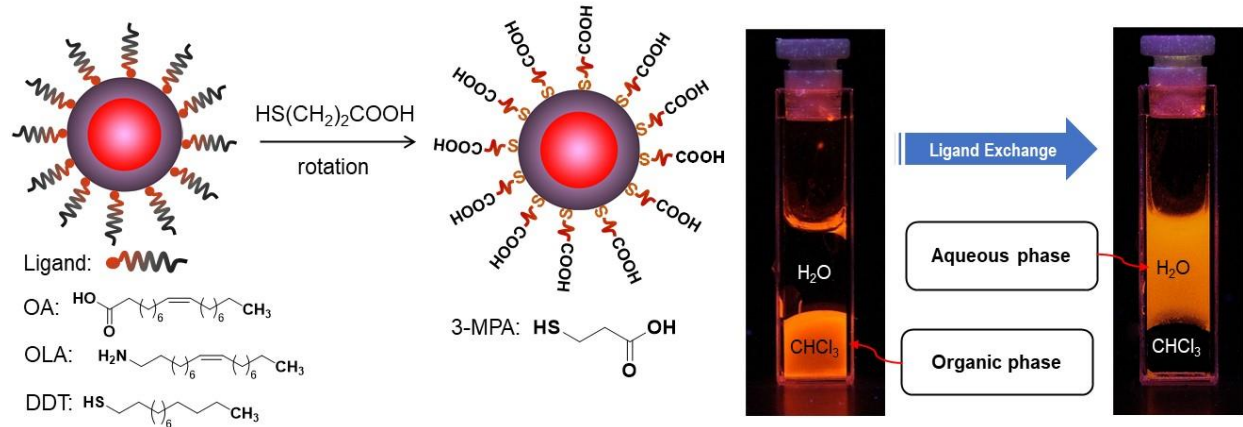
The first excitonic absorption peak at around 530 nm and emission band centered at 534 nm seem remnants of the absorption band at 505 nm and emission positioned at 529 nm, consistent with the green-emitting (CdSe/ZnS)_B core-shell QDs. The slight broadening of the first excitonic peak towards lower energy can be attributed to intercrossing of exciton between two bandgaps,

corresponding to the interfacial alloy and the resulting shrink core CdSe size. The current findings suggest that the S precursor solution plays a critical role in determining the fate of QDs alloying and tunability in the emission color within a wide spectral range, which can be achieved by systematic tuning the relative amount of DDT and OLA.

4.5. Red-emitting CdS Core and CdS/ZnS Core-Shell QDs

The core CdS and series of ZnS monolayers (MLs) passivated CdS core-shell QDs were prepared in non-coordinating ODE and coordinating/stabilizing agents OA/OLA/DDT *via* organometals procedure at high temperature in N₂ atmosphere. The as-prepared QDs were not aqueous soluble, though their colloidal stability in an aqueous medium is necessary for biological applications. Therefore, they were functionalized with 3-mercaptopropionic acid *via* ligand-exchange reaction to render water-soluble, as shown in **Figure 4.5.1**.

Figure 4.5.1 - Schematic illustration and digital photographs of CdS/ZnS core-shell QDs solutions phase transfer from the chloroform layer to water layer after ligand exchange reaction, under irradiation of UV lamp ($\lambda = 365$ nm).

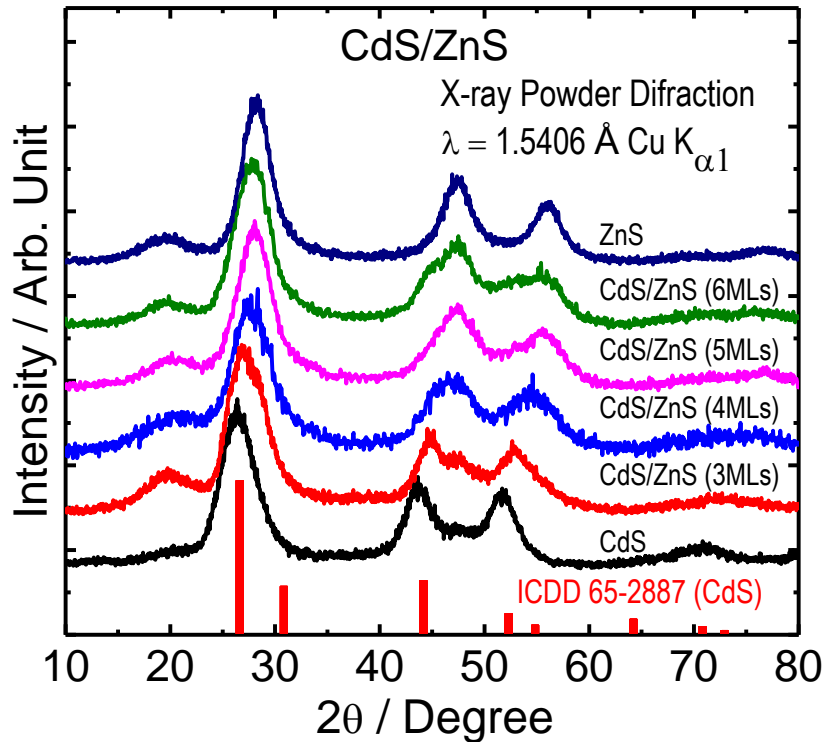


4.5.1. Physicochemical characterization

X-ray diffraction: XRD patterns of uncoated CdS (core material), epitaxial ZnS (shell material), and series of epitaxially ZnS-coated CdS of different monolayers (MLs) are shown in **Figure 4.5.2**. The XRD patterns of both CdS core and ZnS shell separately and in CdS/ZnS core-shell QDs revealed zinc-blende (cubic) phase structures, as previously reported in the literature (ICDD card No. 65-2887 and 01-071-5976, respectively) [124], [125]. The same trend has been reported previously for CdS/ZnS core-shell QDs with six MLs of ZnS [126]. The X-ray reflections of the uncoated CdS core QDs exhibited prominent peaks at scattering angle (2θ) of 26.37°, 43.56°, 51.69° and 71.04° that were indexed to (111), (220), (311) and (331) crystalline planes, respectively, of cubic zinc blend structure consistent to the bulk structure of CdS. No phase change

or alteration in the crystal structure of CdS/ZnS core-shell QDs was observed after the passivation with ZnS monolayers.

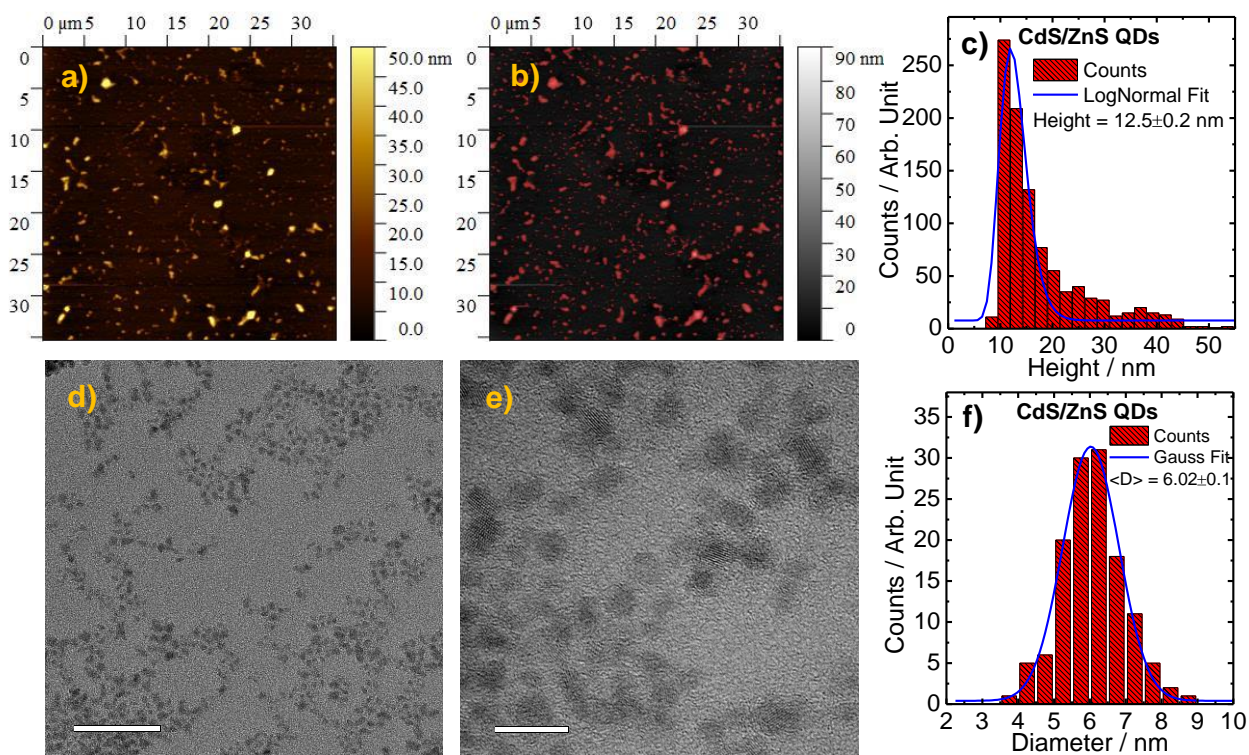
Figure 4.5.2 - XRD patterns of ZnS, unpassivated CdSe and 3-6MLs of ZnS passivated CdS core-shell QDs.



The diffraction peaks of the ZnS lattice are usually merged with the reflection from the highly crystalline CdS creating broad diffraction peaks, which make it difficult to distinguish the independent peaks from core and shell in core-shell nanostructures. This broadening of diffraction peaks and irregular shifts towards a higher angle can be attributed to the existence of stress and strain induced by the lattice mismatch of CdS and ZnS across their interface. It is noteworthy that the diffraction peaks corresponding to CdS QDs were gradually shifted toward higher 2θ values, after coating with ZnS monolayers (MLs), consistent with the zinc-blende (cubic) phase structure of ZnS, confirming the formation of CdS/ZnS core-shell nanocrystals. Additionally, no diffraction peaks were observed from the CdS core in CdS/ZnS due to the high thickness of the ZnS shell, as previously reported in the literature [127].

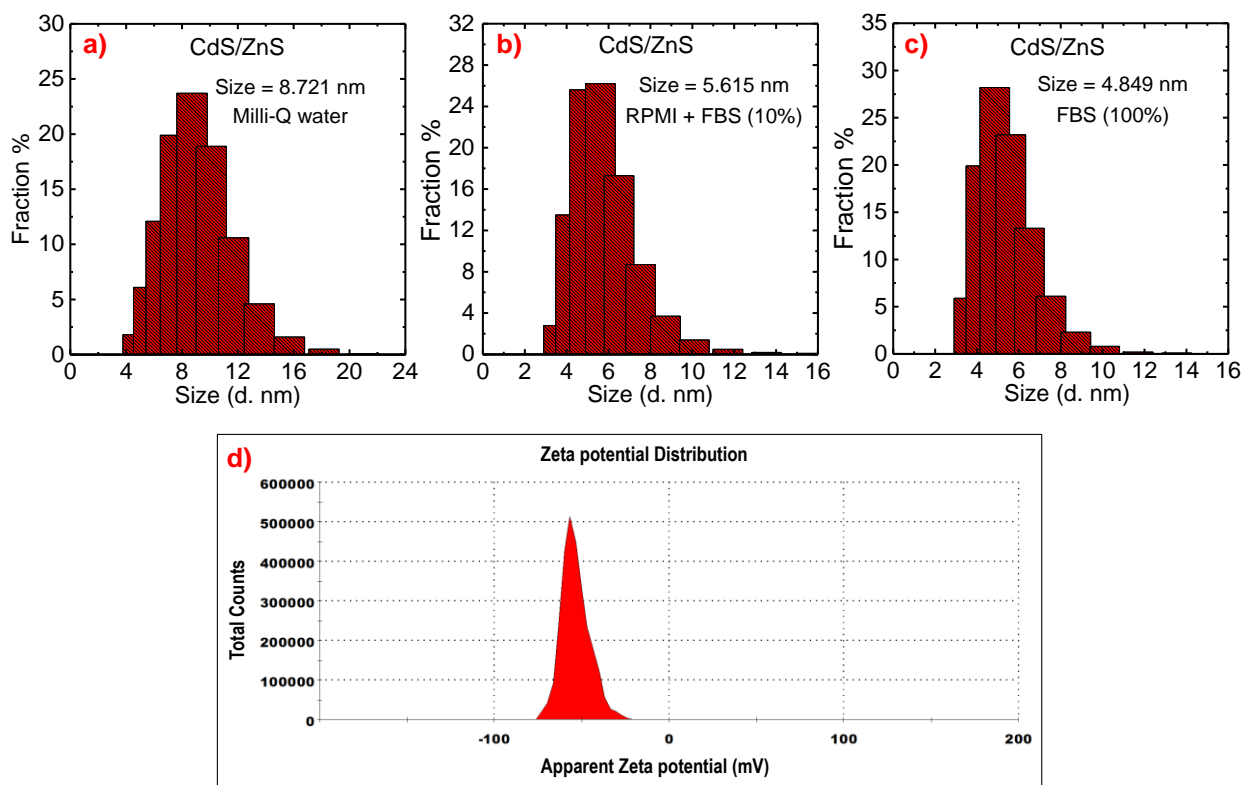
AFM and TEM images: Atomic force microscopy was used to determine the shape, morphology, and average height of 3-MPA capped CdS@ZnS QDs in dilute aqueous dispersion (**Figure 4.5.3a-c**). AFM images of these QDs showed roughly semi-spherical nanoparticles with average height (Z-dimension) of ~ 12.5 nm, as shown in **Figure 4.5.3c**. The average height of the majority of particles was found higher than that of the crystalline size, displayed by transmission microscopy images and hydrodynamic size obtained *via* dynamic light scattering (**Figure 4.5.3 and 4.5.4**). HRTEM images of the core-shell CdSe/ZnS (3MLs) QDs (**Figure 4.5.3a,b**) show ultra-small oval and roughly spherical shapes nanocrystals with narrow size distribution and dominant average diameter of ~ 6 nm, as deduced from the histogram of the particles size distribution (**Figure 4.5.3c**). The average diameter for the CdS/ZnS nanocrystals were obtained by counting more than one hundred and twenty nanoparticles, using imageJ free software and nonlinearly curve fitting (Gauss fit) in origin 8.5.

Figure 4.5.3 - AFM topography (a), phase contrast images (b), height profile (Z-dimension) histogram (c), HRTEM images (different magnifications) (d,e) and histogram of particles size distributions (f) of 3-MPA capped CdS/ZnS QDs.



Hydrodynamic size and zeta potential: The dynamic light scattering data of red-emitting CdS/ZnS QDs exhibited different hydrodynamic size in different aqueous and biological media at a final concentration of 50 $\mu\text{g/mL}$. The obtained results showed an average diameter of 8.721 nm (PDI 0.476) in Milli-Q water, 5.615 nm (PDI 0.558) in RPMI supplemented with FBS (10%), and 4.849 nm (PDI 0.622) in pure FBS (100%). The Z-average diameter of QDs exhibited a gradual reduction in RPMI and FBS (10%) and pure FBS (100%) media, respectively, as compared to that of acquired in the water medium. This propensity to shrinkage can be explained by QDs stabilization and shielding against aggregation and agglomeration due to the surface passivation by adsorbing proteins. The zeta potential of QDs measured in Milli-Q water (50 $\mu\text{g/mL}$) presented negative value (-53.5 mV), as depicted in **figure 4.5.4**.

Figure 4.5.4 - Size-distribution histogram of CdS/ZnS core-shell QDs in Milli-Q water (a), FBS (10%) supplemented RPMI (b), pure FBS (100%) (c), and zeta-potential in Milli-Q water.



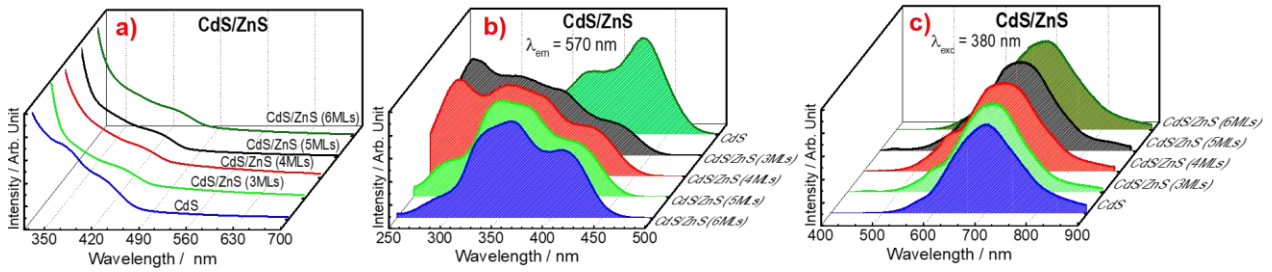
4.5.2. Photoluminescence study

The UV-visible absorption and luminescence spectra of bare CdS core and series of CdS/ZnS core-shell QDs with different shell thickness have been shown in **Figure 4.5.5a-c**. The absorption spectra of uncoated CdS QDs show band centered at 425 nm, which is considerably blue-shifted relative to the bulk band gap (2.42 eV) of CdS, demonstrating the quantum confinement effect [128]. UV-visible absorption spectra (**Figure 4.5.5a**) of CdS QDs passivated by series of ZnS monolayers (3-6MLs) reveal insignificant but slightly noticeable redshift after each shell growth that could be ascribed to the partial leakage of excitons to shell matrix [129]. The slight red-shift in the absorption edge is the spectroscopic signature of epitaxial growth instead of alloy formation or substantiates the incomplete alloying between the core and shell [126]. Interestingly, the same spectral feature was maintained in the UV-visible absorption spectra of all the 3-6ML ZnS passivated CdS QDs.

The emission spectra (**Figure 4.5.5c**) of uncoated CdS and CdS/ZnS core-shell QDs were recorded, by exciting at 380 nm. The emission spectrum of bare CdS QDs presents emission band of lower intensity centered at 581 nm and broad emission bands higher intensity around 697 nm, extending towards lower energy. The energy band positioned at 581 nm originates from excitonic emission *via* the valence band-conduction band recombination process, and the lower energy emission peak could be attributed as the product of surface donor-acceptor pair recombination in deep traps of surface-defects states or surface dangling bonds [126].

The photoluminescence of QDs, besides quantum confinement of exciton, is also strongly governed by the surface states [130] due to the involvement of large percentage of surface atoms in these systems. Consequently, their emission is reduced with increasing the surface to volume ratio, i.e., decreasing the size of nanocrystals, because the surface-trap states are expanded accordingly [131]. The photoluminescence properties can be improved or modified by passivating the surface states *via* organic encapsulation/coating or inorganic epitaxial shell. Therefore, the ZnS epitaxial shell of a wide bandgap was grown on to the targeted core CdS QDs to improve the chemical/photochemical stability, photoluminescence properties, and quantum yield. In CdS/ZnS core-shell QDs, additional emission band at ~ 435 nm (**Figure 4.5.5c**) was observed arising from the near-band-edge recombination of free excitons of ZnS, and it was slightly red-shifted with increasing the shell thickness, suggesting the successful passivation of core CdS with ZnS monolayers.

Figure 4.5.5 - UV-visible absorption spectra (a), excitation spectra (b) and emission spectra (c) of 6MLs ZnS passivated CdS core-shell QDs.



The intensity of intrinsic emission of CdS was increased significantly, without changing the position of emission band, after passivating by ZnS MLs. This is because the CdS/ZnS system is a Type I core-shell material, where the bulk bandgap of ZnS shell (high bandgap material) is larger than the bulk bandgap of CdS core (mid-band gap material) [132]. Thus, the large band offset hinders the tunneling of the photoexcited charge carriers in the conduction band to surface-trap states and confine effectively the photogenerated electron-hole pairs inside the core CdS [127]. In addition, overcoating suppresses the surface nonradiative recombination by passivating the vacancies and deep trap sites on the crystallite surface, resulting in higher luminescence quantum efficiency [132], [133]. However, no noticeable change was observed in the intensity of trap states emission after each ZnS shell growth (**Figure 4.5.5c**), which can be explained by radiative recombination of carriers in the trap-states generated at the core-shell interface, resulting from lattice mismatches (8% between CdS and ZnS), dislocations, and roughening of the surface or due to incomplete passivation of core surface states. The enhancement of photoluminescence intensity and little redshift in both the absorption and emission spectra of CdS/ZnS core-shell QDs substantiate the relevant percentage of epitaxial growth of ZnS shell.

Chapter 5

DEVELOPMENT OF BIONANOPROBE

5 DEVELOPMENT OF BIONANOPROBE

Nanomedicine can be defined as the monitoring, repairing, constructing, and controlling of the human biological systems at the molecular level, using nanodevices and engineered nanostructures. Over the past few decades, nanotechnology has revolutionized medicine, especially concerning the diagnosis and treatment of diseases. Among all types of already developed nanomaterials, QDs stand out for their high fluorescence and versatility that can be used as bionanoprobes in site-specific analyses and diagnosis of macrophages-mediated disorders such as atherosclerosis, obesity, autoimmune diseases, etc.

5.1. Orange-emitting ZnSe:Mn²⁺ QDs as a Bionanoprobe for Macrophages

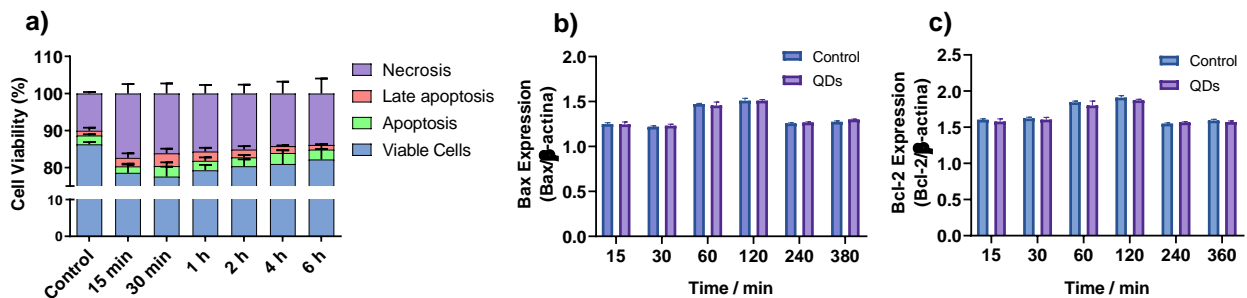
The current work aims to take an insight into the potentialities of orange-emitting ZnSe:Mn²⁺ QDs for clinical and diagnostic purposes. Accordingly, these QDs were synthesized and determined their physicochemical properties, employing various characterization techniques. The biological study was performed in a murine macrophages cell line, RAW 264.7. The QDs were predominantly internalized *via* clathrin-and caveolae-mediated endocytic pathways and showed good biocompatibility in RAW macrophages. The cells accumulated a considerable amount of QDs in a time-dependent manner, which enabled them to give intense fluorescence signals and made them easily visible and detectable with fluorescence microscopy. Nevertheless, the obtained results manifested that these orange-remitting QDs can be an interesting candidate for the development of bionanoprobe used in the site-specific analyses and diagnosis of macrophages-mediated diseases, such as atherosclerosis, obesity, autoimmune diseases, etc.

5.1.1. Assessment of QD Cytotoxicity

The toxicity effect of Mn²⁺ doped ZnSe QDs at a final concentration of 100 µg/mL was assessed in RAW 264.7 macrophages by different toxicity assays, encompassing Annexin V/PI assay, trypan exclusion assays, and analysis of expression of apoptosis-linked genes, for 15 and 30 min and 1, 2, 4, and 6 hours. The viability of RAW 264.7 cells evaluated by Annexin V/PI assay is shown in **Figure 5.1.1a**. The results did not show any significant difference between the treated and untreated cells (negative control), indicating no apparent deleterious effects during incubation for up to 6 h. An additional experiment of expression of apoptosis-linked Bax (proapoptotic) and Bcl2 (antiapoptotic) genes was performed with the same conditions. No significant discrepancy

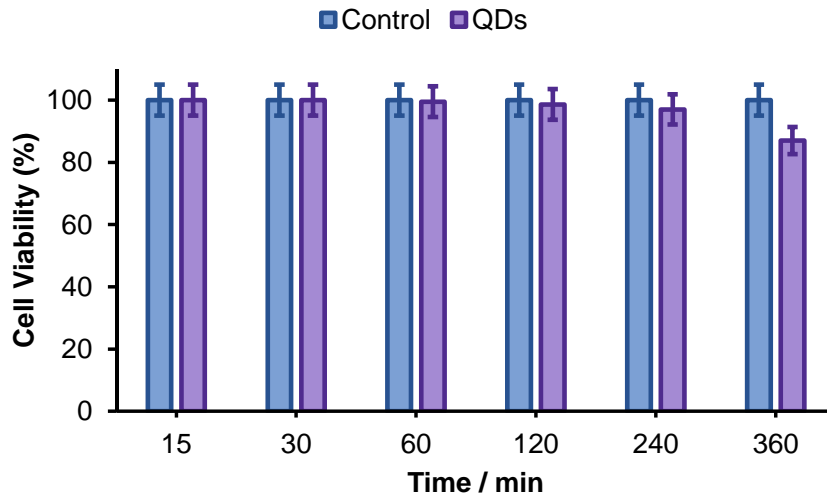
was identified between the findings of treated and untreated cells (negative control), suggesting that the QDs are nontoxic, as shown in **Figure 5.1.1b,c**. The biocompatibility of QDs was further confirmed by the trypan blue exclusion assay, as shown in **Figure 5.1.2**. The obtained findings of different assays were found to be consistent with each other. However, at 6 h interval, there were observed around 80% of viable cells, demonstrating that the ZnSe:Mn²⁺ QDs is biocompatible and has great potential for medical application.

Figure 5.1.1 – Cytotoxicity assessment of ZnSe:Mn²⁺ QDs: annexin V/PI assay (a), apoptosis-linked genes expressed level of mRNA of pro-apoptotic gene Bax (b) and anti-apoptotic gene Bcl-2 (c).



Macrophages were incubated at the indicated time intervals (15 and 30 min, 1, 2, 4, and 6 h) and subsequently analyzed by FACS and by genetic expression of apoptosis-linked genes. For FACS analyses (a), we used the following markers: Propidium Iodide for necrosis, Annexin V for apoptosis, and double labeling for late apoptosis. The QDs treated cells were statistically compared to control: viable cells (^a $p < 0.05$), necrotic cells (^b $p < 0.05$), apoptotic cells (^c $p < 0.05$), and late apoptotic cells (^d $p < 0.05$). Quantitative real-time polymerase chain reaction analysis of mRNA levels of the pro-apoptotic gene Bax (b) and anti-apoptotic gene Bcl-2 (c) were determined after RAW cells exposed to QDs. No significant difference $P < 0.05$ was observed between control versus treated. $n = 3$, ^a $p \leq 0.05$; ^b $p \leq 0.01$; ^c $p \leq 0.001$; ^d $p \leq 0.0001$.

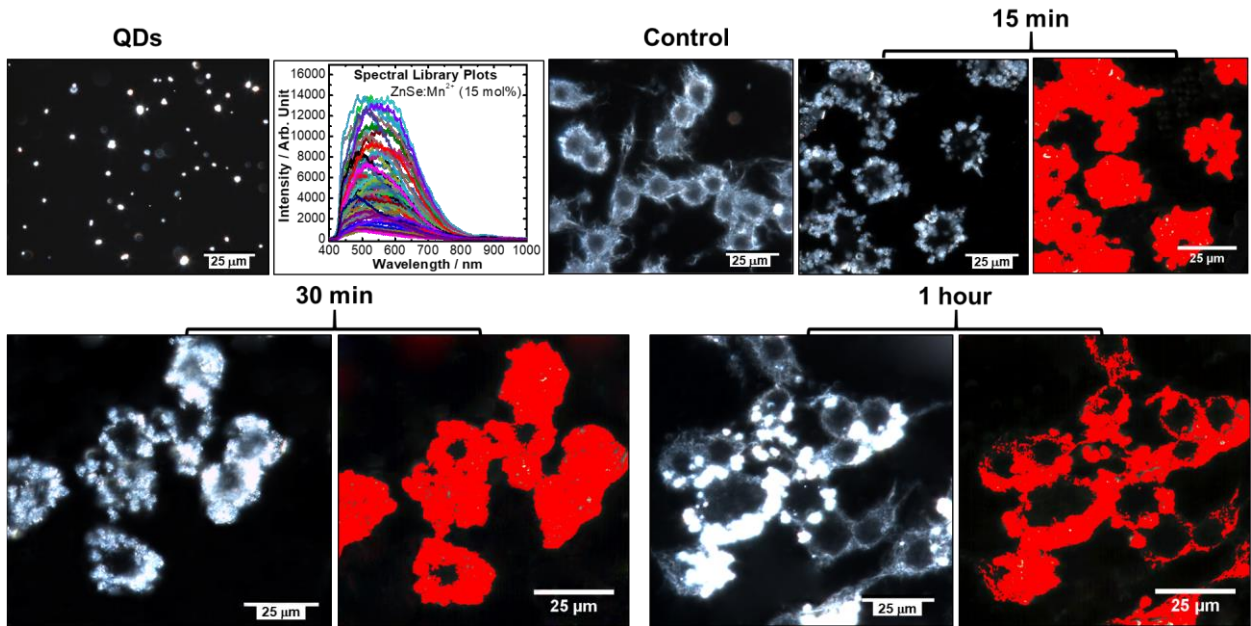
Figure 5.1.2 - Cellular viability assessment of QDs by trypan blue dye exclusion assay .



5.1.2. Time-dependent uptake of QDs

The cellular uptake of orange luminescence Mn^{2+} doped ZnSe QDs was studied in RAW 264.7 macrophages at different incubation times, i.e., 15 min, 30 min, and 1 h, and subsequently analyzed under enhanced dark-field Hyperspectral microscopy (CytoViva®). The cellular uptake was monitored by continuous increasing intracellular background brightness in the dark field images, caused by scattering QDs. Therefore, the dark field hyperspectral images (**Figure 5.1.3**) of cells incubated with QDs (15 min, 30 min, and 1h) show highly bright pixels when compared to the control, confirming the uptake and internalization of QDs by cells. Additionally, all the pixels in images were compared against the spectral library of pure Mn^{2+} doped ZnSe QDs. Each pixel in image matched the QDs spectra that were mapped as red color, showing the location of the spectrally confirmed QDs in the cells.

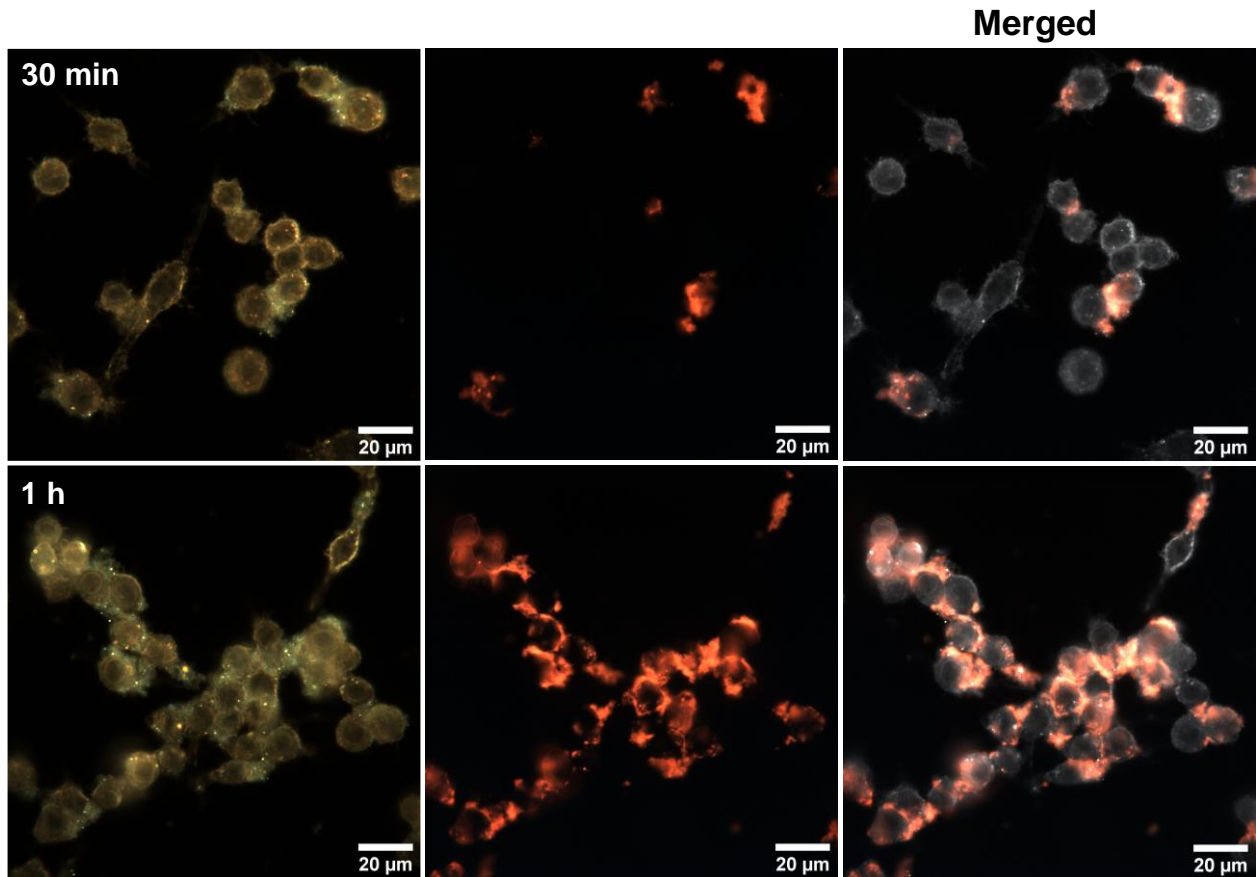
Figure 5.1.3 - CytoViva hyperspectral enhanced dark-field images of ZnSe:Mn²⁺ treated cells obtained at different time intervals.



CytoViva hyperspectral microscopy imaging of ZnSe:Mn²⁺ QDs internalized by macrophages (from left to right). Hyperspectral image of QDs aggregates, spectral profile (spectral library plots) from QDs aggregates ($n \geq 50$), and hyperspectral images of control and cells after 15 min (upper row), and 30 min and 1 h incubation (lower row). The corresponding spectral angle mapping images (red) are indicating the location of the spectrally confirmed QDs in the RAW 264.7 macrophage

These findings were further confirmed by hyperspectral dual-mode fluorescence images of cells incubated with QDs at various times (**Figure 5.1.4**). Highly intense orange emission of Mn²⁺ doped ZnSe was observed in the cells incubated with QDs at 30 min and 1h, when compared to the control, demonstrating the localization of QDs inside the cells.

Figure 5.1.4 - - CytoViva enhanced dark-field and dual-mode fluorescence (DMF) images of live cells treated with ZnSe:Mn²⁺ QDs.



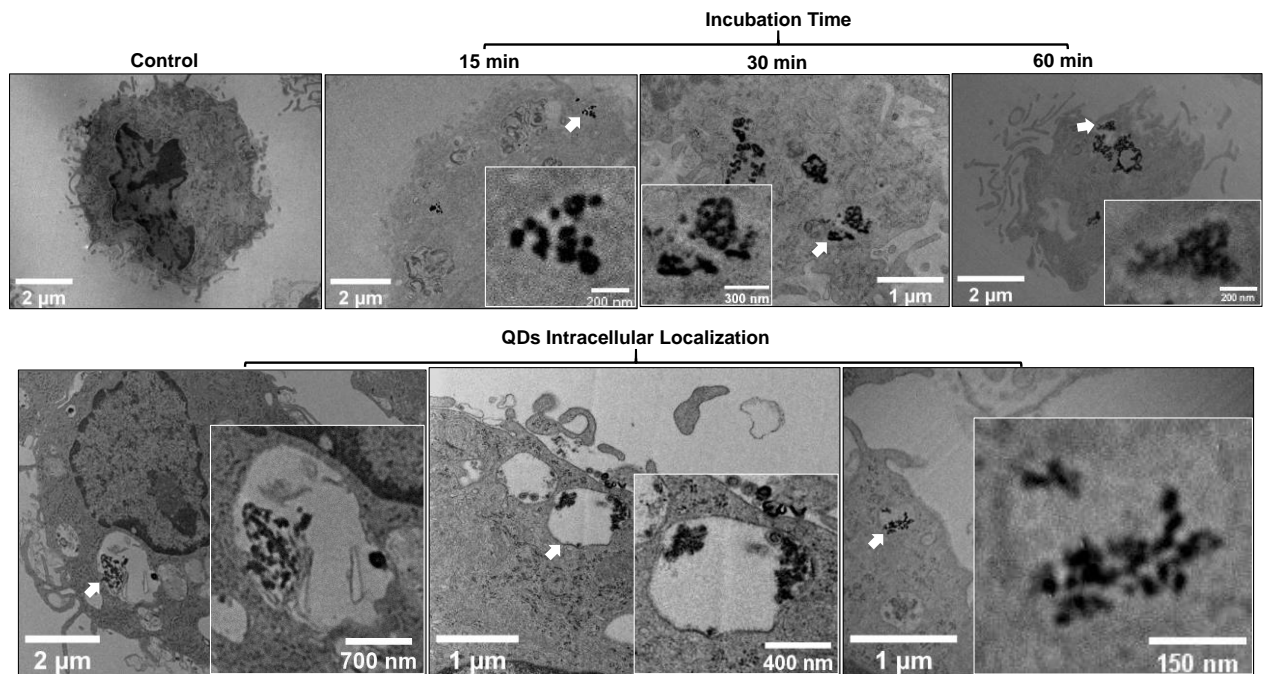
Macrophages were incubated with QDs (10 $\mu\text{g/mL}$) for 30 min and 1 h, mounted on slides, and screened under the microscope, exciting the QDs at 405 nm.

The overall CytoViva results in conjunction with TEM analysis (**Figure 5.1.3** and **5.1.5**) show that the cells analyzed after 15 min demonstrates the smaller amount of QDs in the intracellular regions, indicating the uptake process of cells. However, after exposure for 30 min, the cells reveal an increasing quantity of QDs in the vicinity of the cell membrane and in the intracellular region, comparatively to 15 min incubation, suggesting the consistent cellular uptake process of QDs. For 1 h exposition, a significant change was observed, such as the fraction of QDs in the specific regions of the cell were disappeared, while larger and compact aggregates were appeared in the intracellular region, presumably, in vesicles (endosome/lysosome), corroborated through TEM images (**Figure 5.1.5**). Experimental findings have demonstrated the varying size of

QDs clusters, *i.e.* smaller and larger, which may result from the accumulation of QDs once they are in the intracellular region.

The reported literature studies [134] show that during intracellular trafficking, the smaller organelles containing QDs accumulations merge to form newly larger organelles with the QDs aggregates. The macrophages incubated at various times were also analyzed *via* transmission electron microscopy (TEM) images, to elaborate and confirm the cellular uptake and intracellular localization of QDs, as shown in **Figure 5.1.5**.

Figure 5.1.5 – TEM images of control and ZnSe:Mn²⁺ treated cells obtained after different incubation periods.



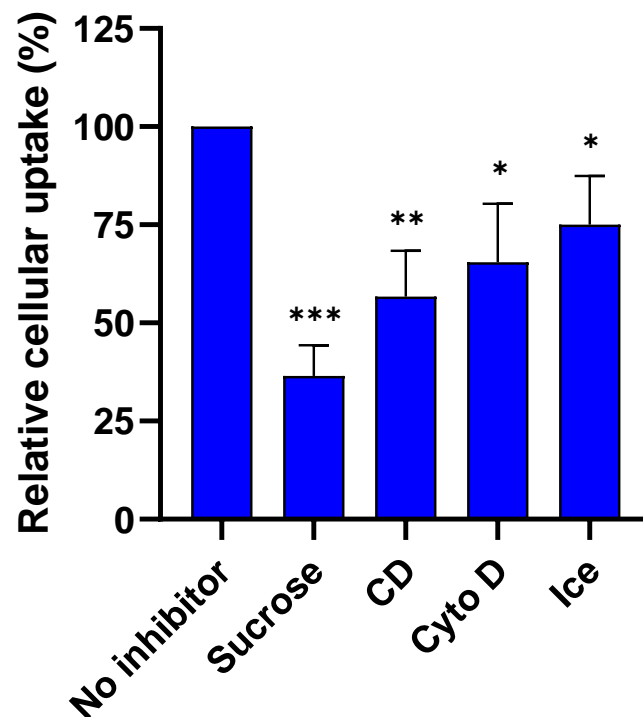
RAW cells were treated with Mn²⁺ doped ZnSe QDs (10 μg/mL) over 15 and 30 min, and 1 h intervals and analyzed by TEM. The micrographs show the control, time-dependent uptake (top panel) and intracellular localization of QDs (bottom panel). The region indicated by arrow has been amplified in the square, manifesting the presence of QDs nanocrystals as high contrast dark-color clusters.

5.1.3. Cellular Uptake Mechanism of QDs

The precise knowledge of endocytosis, intracellular trafficking, and subcellular compartmentalization of cargos is the key determinant to develop new generation bionanoprobe,

achieve site-specific analysis, and selective targeting while evading the off-site problems [89]. However, endocytosis is a complex process dictated by the physicochemical properties of cargos [82]. Therefore, the foremost objective of the study was to identify specific pathways for our 5.61 nm hydrodynamic diameter QDs. Endocytosis proceeds in two major pathways: 1) phagocytosis, actin-driven pseudopodial vesiculation to engulf macromolecules, and relatively larger particles (>500 nm) [135] and 2) pinocytosis, both energy-dependent and nondependent pathway to uptake the liquid and solutes. Pinocytosis can be further subclassified into macropinocytosis, clathrin- and caveolin-mediated endocytosis, and clathrin- and caveolin-independent endocytosis [82], [89], [136], [137]. Clathrin-mediated endocytosis accompanies membrane curvature upon cell-surface and particle interaction followed by the formation of clathrin-coated vesicles that can internalize particles up to ~50 nm [138], [139]. Caveolin-mediated endocytosis is carried out by characteristic flask-shaped invagination formed by cholesterol-rich lipid raft domain and caveolin proteins which has been reported to uptake ~20 nm large particles [138], [139].

Figure 5.1.6 – Effect of pathway-specific inhibitors on ZnSe:Mn²⁺ QDs uptake.



Macrophages were pre-treated with each inhibitor (i.e., sucrose, methyl-beta-cyclodextrin (CD), cytochalasin D (Cyto D) and ice) during 1 h, then incubated with QDs (100 µg/mL) for more 4 h

and subsequently analysed by ELISA microplate reader. Cells not treated with inhibitors were used as positive control. n = 3, *p ≤ 0.05; **p ≤ 0.01; ***p ≤ 0.001; ****p ≤ 0.0001.

To determine the uptake mechanism, various pathway-specific pharmacological inhibitors were utilized: Cyto D (prevents F-actin polymerization), MβCD (depletes cholesterol at cell membrane), hypertonic sucrose (disrupts the clathrin-coated pits), and low temperature (general inhibitor of energy-dependent uptake mechanisms). The quantitative analyses by ELISA microplate reader (**Figure 5.1.6**) show that QDs uptake is extensively declined (64%) by hypertonic sucrose, suggesting that the clathrin-mediated endocytosis is the predominant entry pathway of QDs. MβCD inhibitor dropped the QDs uptake by 43%, which is the signature of the second most used caveolae-mediated endocytosis pathway in the uptake process. In contrast, Cyto D induced relatively weak inhibition of QDs uptake (35%) that can be explained by the incompatibility of QDs size (5.61 nm) to the phagocytic pathway, although phagocytosis is the intrinsic property of RAW macrophages. Noteworthy, low temperature (4 °C) contributed weak inhibition (25%) which suggests energy-independent active uptake process or jointly with QDs adhered to the surface of the cell membrane [135], [140]. These findings indicate that RAW macrophages executed endocytosis predominantly *via* clathrin-and caveolae-mediated endocytic pathway, which are consistent with a previous study in literature [137].

5.2. Wide Visible-Range Activatable Fluorescence ZnSe:Eu²⁺/Mn²⁺@ZnS QDs as Nanoprobe for Bioimaging

The development of bionanoprobe is fundamentally relied upon the precise knowledge of particle-cell behavior, movement of a particle in and out of the cell, and the fate of particle in the course. The present work manifested designing and engineering of water-dispersible Eu²⁺/Mn²⁺ doped ZnSe@ZnS core/shell QDs and their study in macrophages (RAW 264.7), including the biocompatibility, fluorescence imaging, time-dependent uptake, endocytosis, and exocytosis for future application in nanomedicine. The QDs presented high biocompatibility with >85% cell viability and did not induce the cells activation at various concentrations for 48 h. The detailed analyses of QDs treated macrophages by CytoViva microscopy projected systematic color-tunable illumination at different excitation wavelengths and its intensity enhanced as a function of incubation time, maximizing at 24 h. The cells treated for exocytosis, showed efficient intracellular illumination for 24 h. The cellular uptake of QDs measured by FACS presented extensive decline at lower temperature (4 °C), consistent to endocytosis process. The mechanistic investigation of endocytosis process revealed the caveolae-mediated endocytosis and macropinocytosis as the major pathways involved in facilitating the cellular uptake of QDs.

Conclusively, the intrinsic remarkable physicochemical characteristics, unique color tunability and consistent high fluorescence emission over days of QDs would provide the opportunity to use as a multiplex fluorescent nanoprobe for bioimaging in the wide-visible range.

5.2.1. Assessment of QDs Cytotoxicity

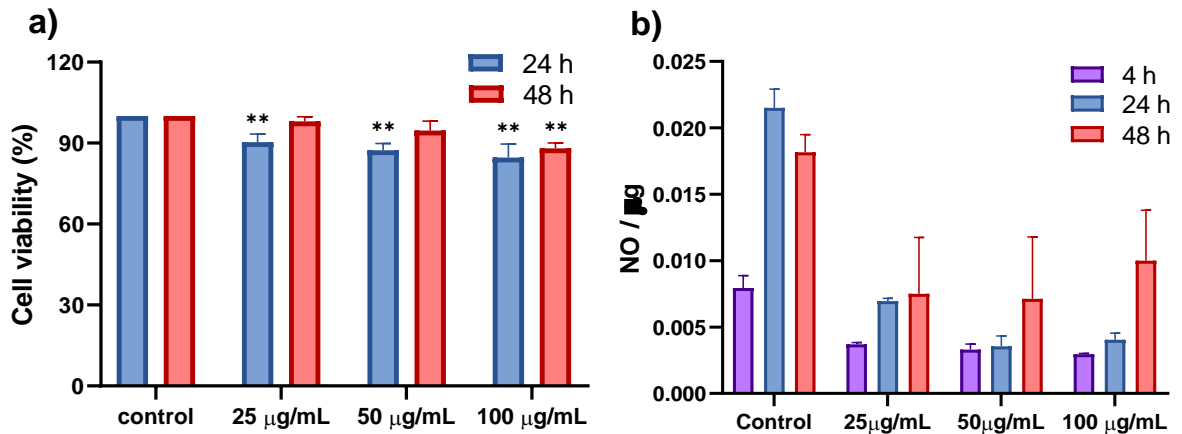
MTT [3-(4,5-dimethylthiazol-2-yl)-2,5-diphenyltetrazolium bromide] staining assay was conducted to analyze the influence of QDs on mitochondrial and non-mitochondrial enzymatic (flavin oxidase, succinate dehydrogenase, NADH reductase, and other oxidoreductases) functionalities and cellular metabolic/energy perturbation in RAW macrophages at a concentration of 25, 50, and 100 µg/mL for 24 and 48 hours. The results were calculated using the following formula.

$$\text{Cellular viability (\%)} = (OD_{\text{treated}} - OD_{\text{blank}} / OD_{\text{control}} - OD_{\text{blank}}) \times 100$$

The obtained findings of treated and untreated cells were found consistent with each other and did not confirm any significant discrepancy for 48 h (**Figure 5.2.1**), revealing that the QDs are highly

biocompatible and applicable to biomedical purposes. Additionally, the QDs did not induce NO production compared to negative control, indicating that cells are not activated by recognizing the QDs as threat and are applicable to cellular labeling., as shown in **Figure 5.2.1**.

Figure 5.2.1 – Effect of ZnSe:xEu²⁺,yMn²⁺@ZnS (x, y = 12 mol%) QDs on cell viability and activation.



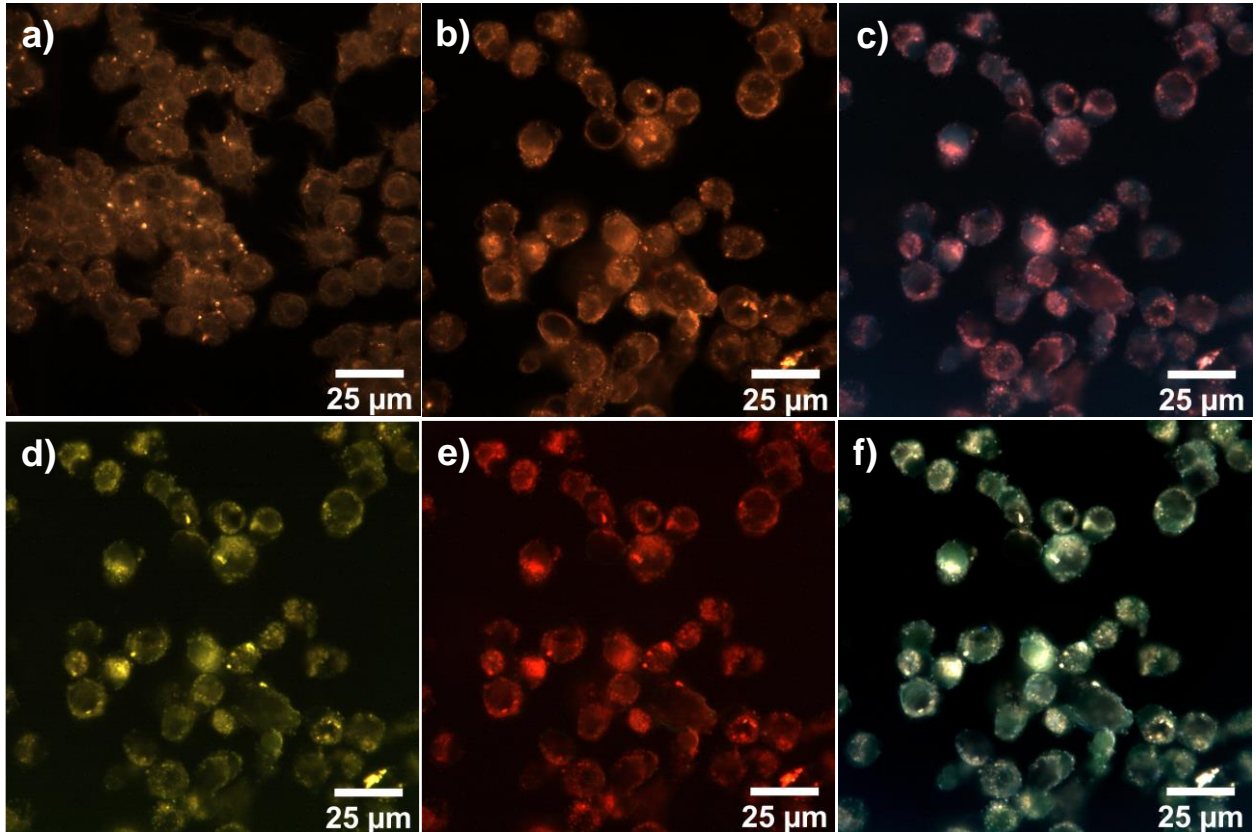
RAW macrophages were incubated with QDs (25, 50, and 100 µg/mL) for 24 and 48 hours and analyzed by MTT (a) and Griess assay (b). Cells not treated with QDs were used as negative control. n = 3, *p ≤ 0.05; **p ≤ 0.01; ***p ≤ 0.001; ****p ≤ 0.0001.

5.2.2. Fluorescence Imaging of QDs in RAW Cells

The study of bio-imaging was conducted in RAW cells treated with QDs at a concentration of 100 µg/mL treated for 24 h. The cells were visualized by CytoViva dual-mode fluorescence imaging system, and fluorescence images of live cells were obtained to evaluate qualitatively the amount of internalized QDs and their intracellular distribution. Multicolor images were acquired by monitoring the QDs photoluminescence emission at different excitation wavelengths: $\lambda_{exc} = 390, 445,$ and 520 nm, as shown in **Figure 5.2.2**. The CytoViva images of QDs without cells have been shown in **figure 5.2.3**. The multi-color fluorescence in images (**Figure 5.2.2**) projects the considerable amount of QDs dispersed non-aggregatively and in granulated clusters in the periphery of cell membrane and cytoplasm, suggesting that the QDs are in the intracellular vesicles. The nearly uniform distribution of illumination throughout the cells rules out the preferential accumulation and confinement of QDs to a specific region. The multi-color emissions at fixed positions in the intracellular regions negate the possibility of autofluorescence. These unique features of QDs will make it unprecedented to reduce the

background noise and enhance the receiving signal by modulating the photoluminescence emission in the biomedical and biological applications.

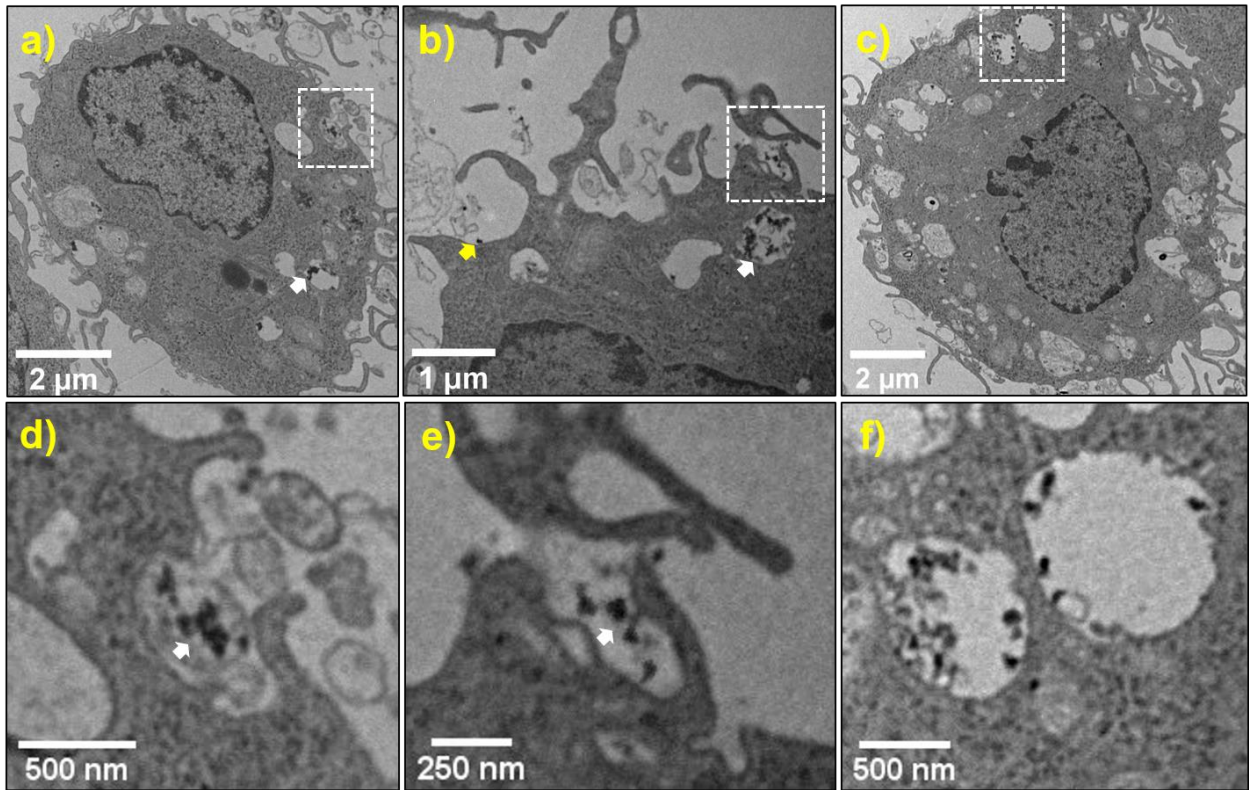
Figure 5.2.2 –CytoViva enhanced dark-field and dual mode fluorescence images of cells treated with ZnSe:xEu²⁺,yMn²⁺@ZnS (x, y = 12 mol%) QDs.



RAW cells were treated with QDs at concentration of 100 μg/mL) for 24 hours, washed several times with PBS, and mounted on the slides. The images were obtained while exciting the QDs at various excitation wavelengths: enhanced dark field images of control and treated cells (a, b, respectively), and dual mode fluorescence images at ($\lambda = 390$ nm) (c), $\lambda = 445$ (d), and $\lambda = 520$ nm (e), and all excitation wavelengths simultaneously (f).

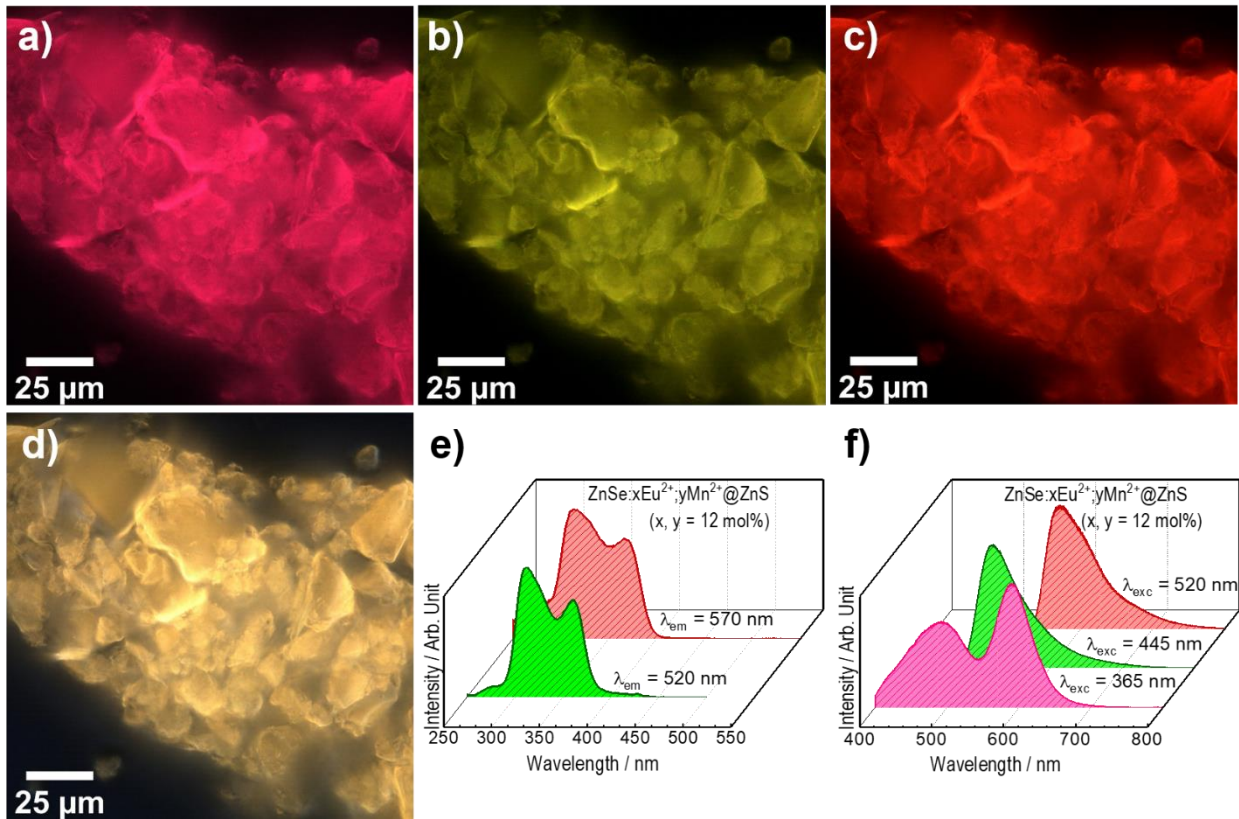
Transmission electron microscopy (TEM) images were acquired to confirm the intracellular distribution of QDs (**Figure 5.2.3**). TEM images manifested the localization of QDs in the vesicles, presumably in the endosome/lysosome. This result is clearly evident from the high-resolution TEM images (**Figure 5.2.3d-f**), which visualized the ZnSe:xEu²⁺,yMn²⁺@ZnS nanocrystals aggregated and dispersed in the vesicular regions, as validated by the contrast difference of the cytoplasm and vesicles intracellular environment.

Figure 5.2.3-TEM images of cellular uptake and colocalization of ZnSe: $x\text{Eu}^{2+},y\text{Mn}^{2+}@ZnS$ ($x, y = 12$ mol%) core-shell QDs.



RAW cells treated with QDs ($100 \mu\text{g}/\text{mL}$) for 2 h and analyzed by TEM. The micrograph show the cellular uptake and colocalization of QDs, indicating as high contrast dark-color clusters (a-c). The images highlighted by squares (top panel) have been magnified in the nearby images (bottom panel), showing the receptor-mediated endocytosis (d), macropinocytosis (e), and colocalization of QDs (e). The yellow arrow (figure b) indicates the phagocytosis.

Figure 5.2.4 – CytoViva enhanced dark-field and dual-mode fluorescence (DMF) images of multicolor-emitting ZnSe:xEu²⁺,yMn²⁺@ZnS (x, y = 12 mol%) core-shell QDs.



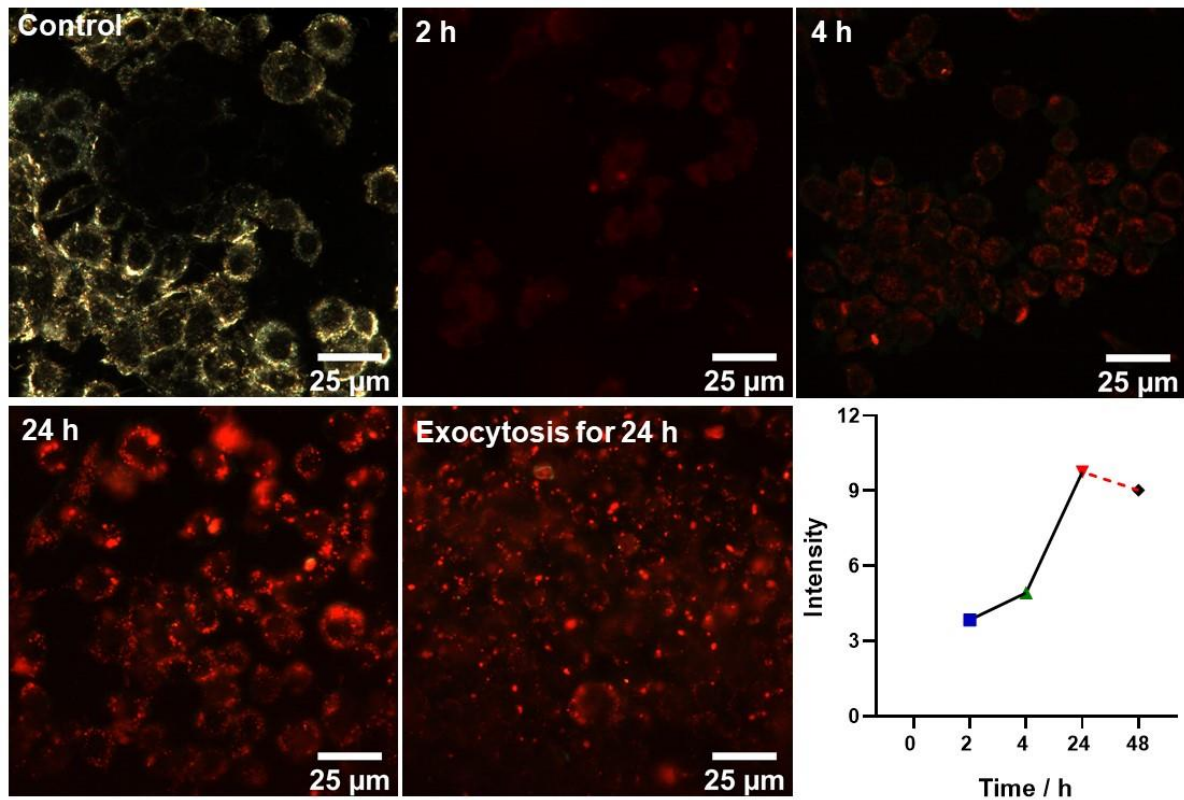
CytoViva dual-mode fluorescence images of aqueous ZnSe:xEu²⁺,yMn²⁺@ZnS (x, y = 12 mol%) QDs dispersion aggregate on slide, under various excitation wavelengths: $\lambda_{\text{exc}} = 390$ nm (a), $\lambda_{\text{exc}} = 445$ nm (b), $\lambda_{\text{exc}} = 520$ nm (c) and white light (d), excitation, (e) and luminescence spectra of the corresponding core/shell QDs recorded under excitations at $\lambda_{\text{exc}} = 365$ nm (b), $\lambda_{\text{exc}} = 445$ nm (c) and $\lambda_{\text{exc}} = 520$ nm.

5.2.3. Time-dependent uptake and exocytosis of QDs

The cellular uptake of QDs as function of time was studied for 2, 4, and 24 h. For exocytosis, the cells were washed after treatment with QDs for 24 and reincubated in QDs free medium for additional 24 h. The images were acquired while monitoring the emission in the red window. The cellular fluorescence intensity steadily enhanced with extending the incubation time and exhibited intense luminosity at 24 h (**Figure 5.2.5**), indicating the continuous feeding process of QDs by macrophages. The cells incubated for exocytosis projected comparatively efficient illumination after 24 h, however, with a slight declivity in the emission intensity, suggesting that small amount of QDs have been excreted by the macrophages. Additionally, the projection of

efficient illumination after 48 h by cells suggest that QDs are photochemically stable in the physiological environment of cells. The retention of large amount of QDs for extended time would be useful to acquire fluorescence images or monitor the bioanalyses for longer time.

Figure 5.2.5- CytoViva enhanced dark-field and dual-mode fluorescence (DMF) images of time-dependent uptake and exocytosis.



RAW cells were treated with QDs for 2, 4, and 24 h to determine cellular uptake of QDs as function of time. For exocytosis, after exposure to QDs for 24 h, the medium was replaced by fresh medium and incubated the cells for additional 24 hours. The graph at the right bottom shows the change in fluorescence intensity as function of time. The red dotted line indicates the change in fluorescence intensity after exocytosis for 24 h.

5.2.4. Cellular Uptake Mechanism of QDs

The cellular uptake pathway of QDs was elucidated at a concentration of 50 $\mu\text{g/mL}$ treated for 3 hours. The uptake of QDs was confirmed by CytoViva dual-mode fluorescence imaging system, and the quantitative analysis was performed by FACS, benefiting from the photoluminescence properties of QDs. The QDs were excited by using three different lasers violet ($\lambda = 405 \text{ nm}$), blue ($\lambda = 488 \text{ nm}$), and yellow-green ($\lambda = 561 \text{ nm}$), and the change in fluorescence

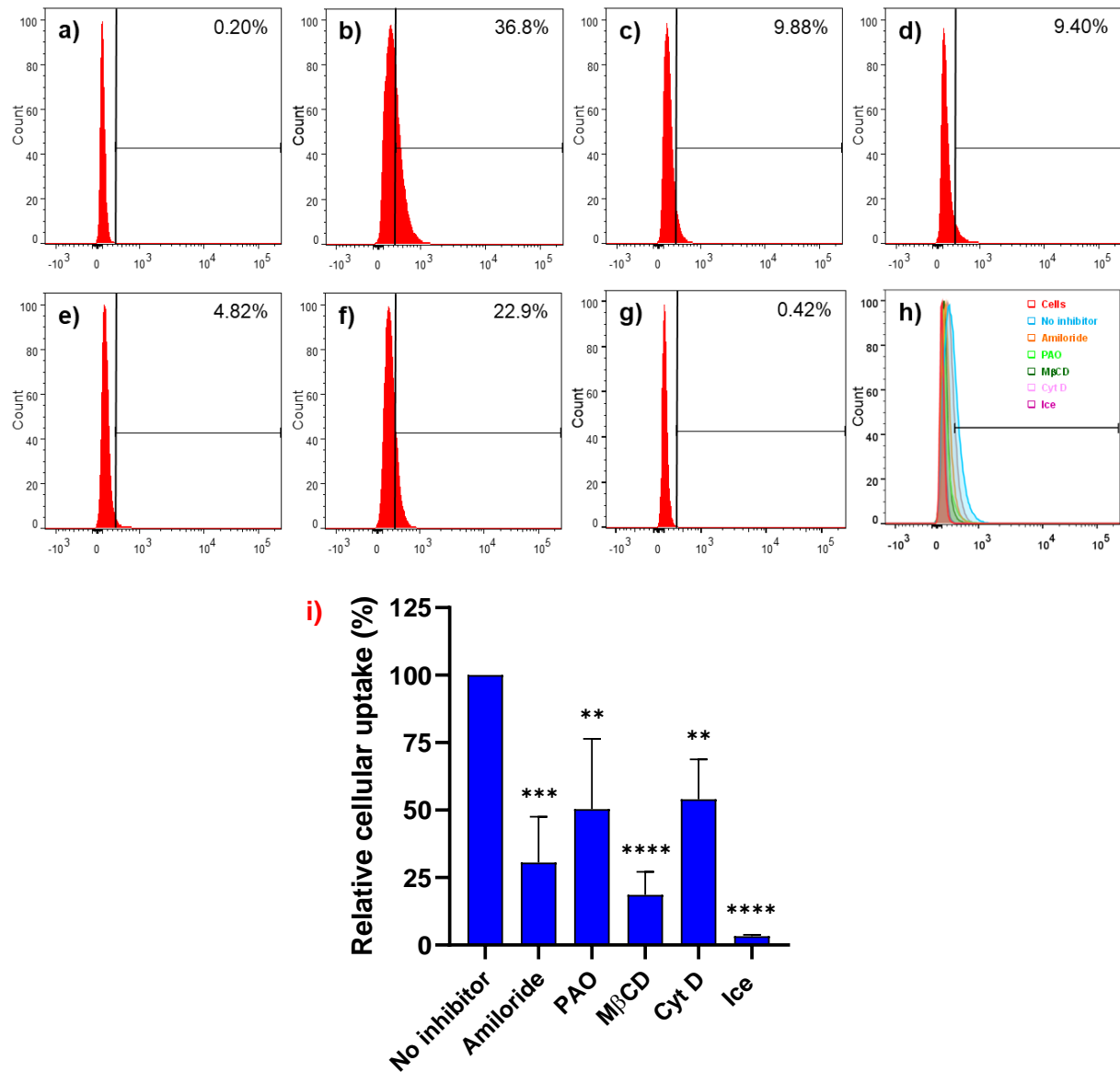
intensity was recorded at PE-Texas Red-A channel. The irregular changes in fluorescence intensity is linearly proportional to the amount of QDs internalized by cells or jointly with QDs, probably attached to cell surfaces. The fluorescence intensity of treated samples was normalized to autofluorescence of untreated control (cells without QDs and inhibitors), and the relative uptake (%) was calculated.

The particle-cellular behavior and the fate of particles in the course are the key factors to consider and understand before developing a new generation bionanoprobe, achieve personalized nanomedicine, and enhance prognostic and selective treatment efficacy. However, the process is strictly governed by the physicochemical features of particles; therefore, the study aims to unravel the uptake mechanism for QDs of 5.6 nm size. Generally, in RAW macrophages, two major pathways are active in the endocytosis of cargos: 1) phagocytosis (cell eating process), particularly, engulf the macromolecules and relatively larger particles (>500 nm) [84] enwrapped in actin-driven pseudopodial vesiculations and 2) pinocytosis (cell drinking process), especially, uptake the liquid and solute. Pinocytosis is executed by four different pathways: namely, macropinocytosis, clathrin-mediated endocytosis, caveolin-mediated endocytosis, and clathrin-and caveolin-independent pathways. The pathways internalize cargos proportional in size to the inner volume of transporting vesicles: macropinocytosis (0.2-5 μm in diameter) [84], [141], clathrin-mediated endocytosis (100-200 nm) [142], caveolae-mediated endocytosis (50-80 nm) [143], clathrin-and caveolae-independent endocytosis (40-50 nm) [89]. Macropinocytosis involves actin-driven circular dorsal ruffles to engulf a large amount of fluid and solute *via* collapsing back on to the plasma membrane to form macropinosomes [84], [141]. The process is accompanied by exchanging Na^+/H^+ in the cell membrane [136], [137]. Clathrin-mediated endocytosis is the major pathway used to uptake the nutrients, biomolecules, and nanomaterials in eukaryotic cells. Clathrin-mediated endocytosis initiates at receptor-ligand interaction that induces assembling of various clathrin and adaptor proteins, driving the membrane curvature and clathrin-coated pits towards the cytosolic side of the plasma membrane [142]. Caveolin-mediated endocytosis involves clustering of cholesterol-enriched lipid rafts on the cytosolic side of the plasma membrane to form flask-shaped invaginations that are architected and stabilized by caveolin proteins [143].

The mechanism of QDs uptake was unraveled by using different pathway-specific inhibitors: Cyt D which inhibits F-actin polymerization; M β CD which extracts cholesterol to prevent the formation of caveolae vesicles; amiloride which blocks Na^+/H^+ exchange across the cell membrane; low temperature which is a general inhibitor of all energy-dependent uptake mechanisms; and PAO

which is not completely known. The quantitative analyses accomplished *via* FACS (**Figure 5.2.4a-h**) show that QDs uptake was significantly blocked by M β CD and amiloride inhibitors, suggesting the major contribution by two predominant pathways in endocytosis: caveolae-mediated endocytosis and macropinocytosis, respectively, as shown in **Figure 5.2.4i**. Amongst them, caveolae-mediated endocytosis executed comparatively lower QDs uptake, which is consistent with the previous study in literature [137]. PAO relatively contributed to the lower inhibition of QDs, indicating that uptake was also facilitated by clathrin-mediated pathway. Contrary, Cyt D didn't induce considerable inhibition of QDs uptake, indicating that the size of QDs (5.61 nm) is not compatible with the phagocytic pathway. Cells treated on ice presented extremely lower QDs uptake which is a signature of energy-dependent endocytosis process rather than diffusion across the cell membrane. None of the inhibitors individually blocked the uptake of QDs completely, implying that QDs are endocytosed concurrently by different endocytic pathways.

Figure 5.2.6 – Quantitative analyses of ZnSe:xEu²⁺,yMn²⁺@ZnS (x, y = 12 mol%) QDs uptake mechanism by FACS.



The cells were pretreated with different inhibitors, such as amiloride, PAO, MBCD, Cyt D, and 4 °C, over a period of 1 h and subsequently exposed to QDs for additional 3 hours. The cells were washed with PBS, harvested by trypsinization and read by FACS, exciting the QDs at three different lasers violet ($\lambda = 405$ nm), blue ($\lambda = 488$ nm), and yellow-green ($\lambda = 561$ nm) and the change in fluorescence intensity was recorded at PE-Texas Red-A channels. The change in fluorescence intensity shows the variation of QDs uptake: negative control (a) and positive control (b); and cells treated in the presence of amiloride (c), PAO (d), M β CD (e), Cyt D (f), 4 °C (g), joint histogram (h), and graphical illustration of QDs uptake inhibition (i). Cells not treated with inhibitors were used as positive control. n = 3, *p \leq 0.05; **p \leq 0.01; ***p \leq 0.001; ****p \leq 0.0001.

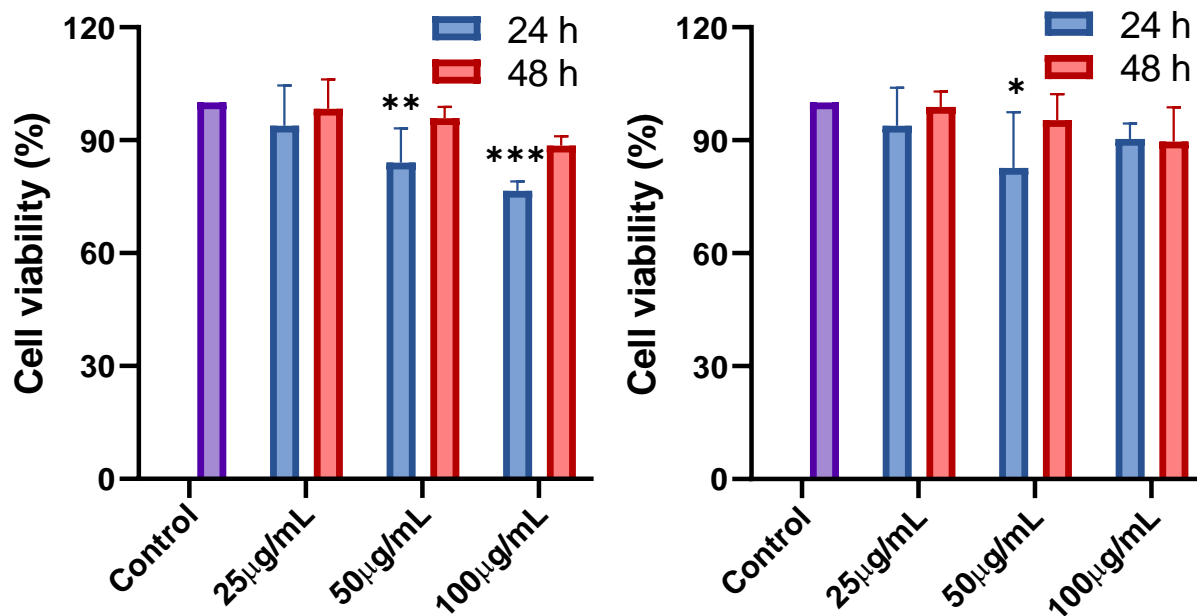
5.3. Exploring the Potentials of Color-tunable CdSe/ZnS QDs as Nanoprobe for Macrophages

The purpose of this work is to explore the intrinsic potentialities of color-tunable and highly photoluminescent orange-emitting (CdSe/ZnS)_A and green-emitting (CdSe/ZnS)_B core-shell QDs for the future development of phagocytosis-based clinical and diagnostic bionanoprobe. The QDs were prepared *via* the organo-metals method, rendered water-soluble, and determined their physicochemical and photoluminescent properties. The biological study including cell viability, fluorescence imaging, and uptake mechanism of QDs was performed in mouse monocyte/macrophage cell line, RAW 264.7. The QDs did not cause any deleterious effects and presented an enhanced fluorescence signal in the intracellular regions of cells. The uptake of (CdSe/ZnS)_A and (CdSe/ZnS)_B QDs were completely blocked at a lower temperature (4 °C), consistent with energy-dependent endocytosis. The cells were identified to execute endocytosis of (CdSe/ZnS)_A QDs predominantly by three major pathways: macropinocytosis and clathrin and caveolae-mediated endocytosis. Nearly similar results were presented by (CdSe/ZnS)_B QD; however, in such cases, the inhibitory drugs blocked the QDs uptake weakly, suggesting that some other pathways are involved in the endocytosis. Nevertheless, the obtained results manifested that these orange-emitting QDs can be an interesting candidate for the development of bionanoprobe used in the site-specific analyses and diagnosis of macrophage-mediated diseases, such as atherosclerosis, obesity, autoimmune diseases, etc.

5.3.1. Assessment of QDs Cytotoxicity

RAW cells were exposed to (CdSe/ZnS)_A and (CdSe/ZnS)_B QDs at concentration of 25, 50, and 100 µg/mL for 24 and 48 h, and MTT assay was conducted to determine the cell viability. The findings did not present any significant difference between the positive control and negative control for 48 h, suggesting that both of the QDs are highly biocompatible, as shown in **Figure 5.3.1**. It is well-known from previous studies that the Cd-based QDs are highly toxic due to leaching out of toxic heavy metal Cd²⁺ ions which interact with biomolecules, disrupt the cellular functions, and induce oxidative stress, leading to cell damage and death. The cytotoxicity of QDs can be reduced by surface-passivation with organic or inorganic non-toxic or less hazardous materials that protect the core from the external environment and impeded the release of Cd²⁺ ions [144]. Therefore, the nontoxicity in our system can be explained by the epitaxial growth of nontoxic ZnS that protects the core from exposure to the environment and hampers the leaching out of Cd²⁺ ions [145].

Figure 5.3.1 - Effects of orange-emitting (CdSe/ZnS)_A (left) and green-emitting (CdSe/ZnS)_A (right) QDs (25, 50, and 100 µg/mL) on cell viability of RAW macrophages incubated for 24 and 48 hours.

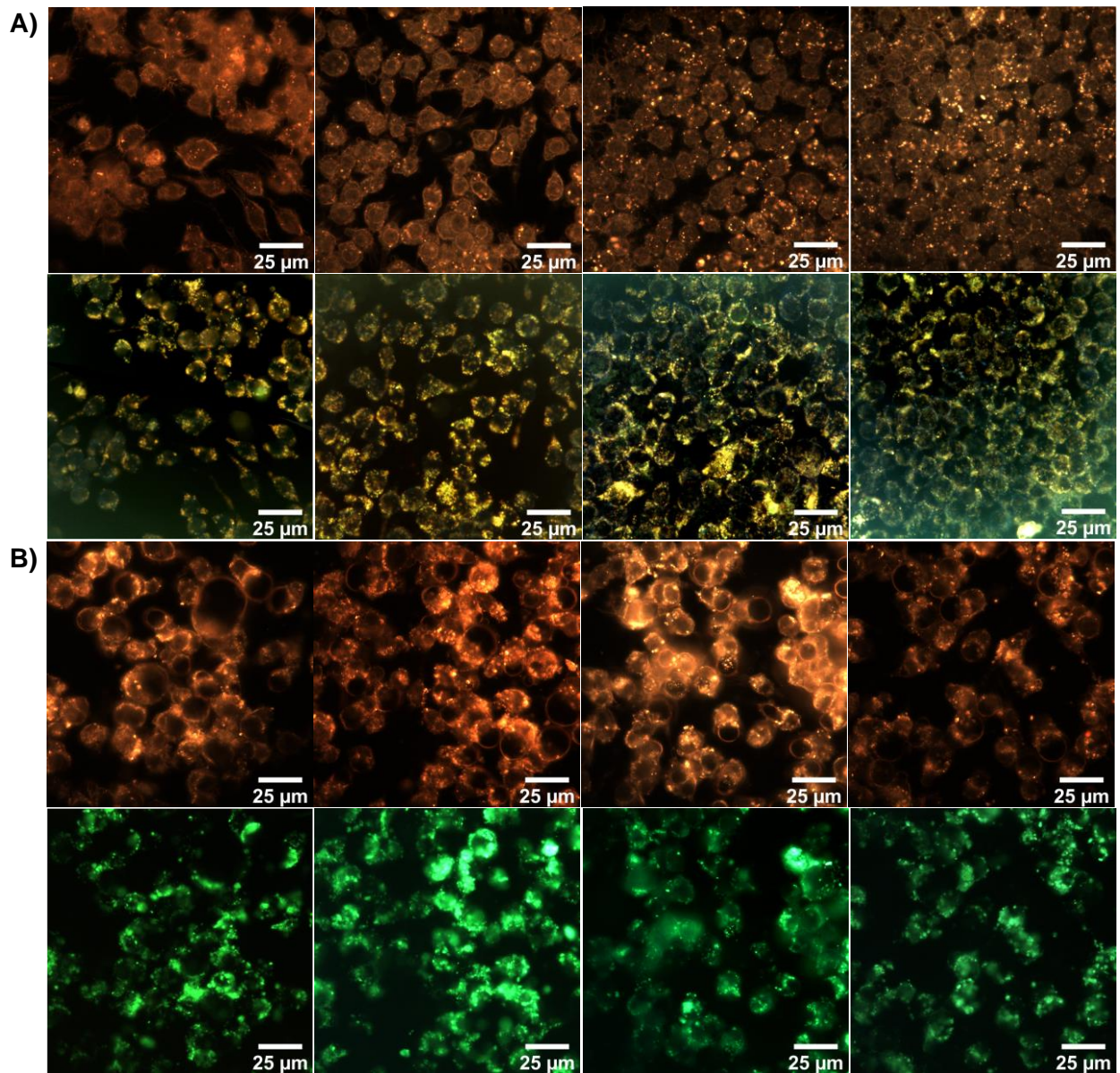


Cells not treated with QDs were used as negative control. $n = 3$, * $p \leq 0.05$; ** $p \leq 0.01$; *** $p \leq 0.001$; **** $p \leq 0.0001$.

5.3.2. Fluorescence Imaging of QDs in RAW Cells

Fluorescence images of live cells were acquired by CytoViva dual-mode fluorescence imaging system to confirm qualitatively the cellular uptake and intracellular distribution of (CdSe/ZnS)_A and (CdSe/ZnS)_B, QDs as shown in **Figure 5.3.2**. The images displayed enhanced orange and green illumination, substantiating that a considerable amount of QDs has been internalized by cells. The fluorescence (**Figure 5.3.2A**) predominantly projected in constellation pattern in the vicinity of the cell membrane and intracellular regions, manifesting the granulated clusters of QDs. It is evident from the background fluorescence of some regions of cells (mostly green-emitting) that the QDs are distributed evenly and singly or in insignificantly small aggregates in the intracellular regions. QDs were also observed scattered, as evident from the background fluorescence of cells. The QDs were observed highly stable and luminescence in the intracellular regions after 24 h of treatment, as it is evident from photoluminescence emission in images.

Figure 5.3.2 - CytoViva enhanced dark-field and dual-mode fluorescent images (DMF) images of live RAW macrophages stained with orange-emitting (CdSe/ZnS)_A (A) and green-emitting (CdSe/ZnS)_B (B) QDs.



RAW cells were treated with QDs for 24 h, washed with PBS, mounted on a slide, and photographed by CytoViva microscope. The upper row in each panel (A) and (B) shows the enhanced dark-field images and the lower panel shows CytoViva dual-mode fluorescence images of cells.

5.3.3. Cellular Uptake Mechanism of QDs

The uptake mechanism of cargos is the prime factor that monitors and determines the accuracy of targeted delivery, efficiency of diagnostics, and therapeutics. As previously discussed, the mechanism

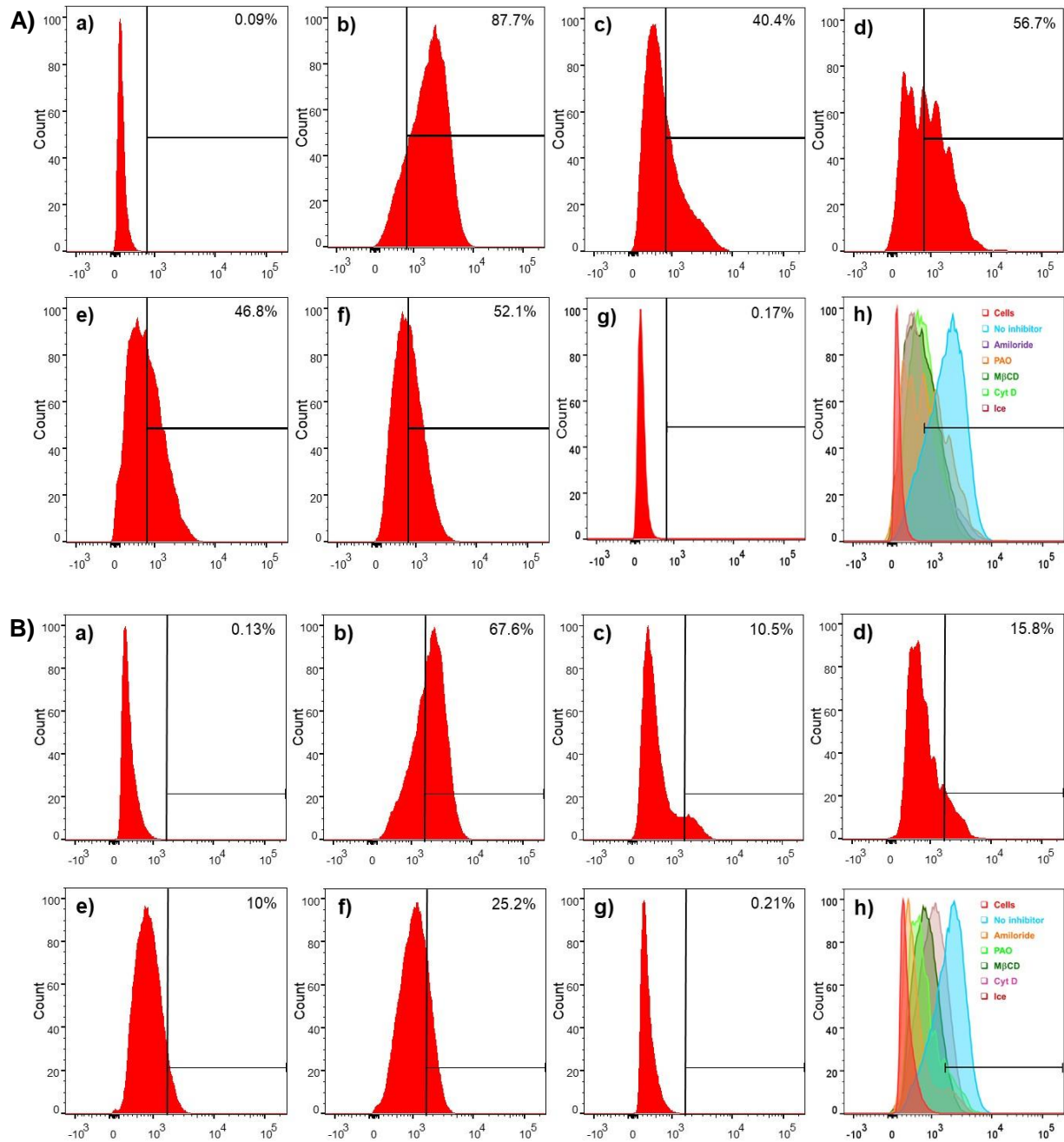
of cellular uptake is strictly governed by the physicochemical properties of particles, especially the size. Therefore, the study aims to elucidate the specific entry pathways for QDs of two different sizes: $(\text{CdSe/ZnS})_A$ of 5.6 nm and $(\text{CdSe/ZnS})_B$ of 7.5 nm. Cellular uptake occurs *via* different energy-dependent pathways consistent to the physicochemical features of cargos, most importantly the size: phagocytosis (>0.5 nm), macropinocytosis (>0.5 nm), clathrin-mediated endocytosis (100-200 nm), caveolae-mediated endocytosis (50-80 nm), and clathrin-and caveolae independent endocytosis (40-50 nm) [82], [89], [136]–[139].

To unravel the specific endocytosis pathway, we used different pathways-specific inhibitory drugs: Cyt D (blocks phagocytosis), M β CD (blocks caveolin-mediated endocytosis), PAO (blocks clathrin-mediated endocytosis), amiloride (blocks macropinocytosis), and low temperature (general inhibitor of energy-dependent uptake mechanisms). And the quantitative inhibition of QDs uptake was monitored by FACS *via* a change in the fluorescence intensity.

The obtained findings by FACS (**Figure 5.3.3**) presented considerable inhibition of $(\text{CdSe/ZnS})_B$ with three different drugs of amiloride, PAO, and M β CD, indicating that the QDs are majorly endocytosed by three predominant pathways, such as macropinocytosis, clathrin-mediated and caveolae-mediated endocytosis, respectively (**Figure 5.3.4**). The amiloride was identified to be the most efficient inhibitor of QDs uptake, which signifies that the endocytosis is comparatively more facilitated by macropinocytosis. The PAO also contributed to extensive fall off QDs uptake, which manifests that clathrin-mediated endocytosis is the second most exploited pathway in the transportation of QDs into cells. Cyt D induced comparatively lower uptake inhibition, probably due to the non-biocompatibility of QDs to the phagocytosis process. At lower temperature (4 °C), the cellular uptake of QDs was reduced extensively, almost to the insignificant level of QDs uptake, which is the hallmark of energy-dependent endocytosis.

The RAW macrophages internalized a large amount of $(\text{CdSe/ZnS})_A$ compared to $(\text{CdSe/ZnS})_B$ with three major inhibitors: amiloride, PAO, and M β CD, representing the inhibition of micropinocytosis, clathrin-mediated endocytosis, and caveolae-mediated endocytosis pathways. Besides, Cyt D also hindered the QDs uptake considerably but slightly lower than other inhibitors, indicating that the internalization is facilitated to a large extent by the phagocytic pathway. The relatively lower inhibition of $(\text{CdSe/ZnS})_A$ suggests that some other energy-dependent pathways are involved in the uptake, probably clathrin-and caveolae-independent pathways.

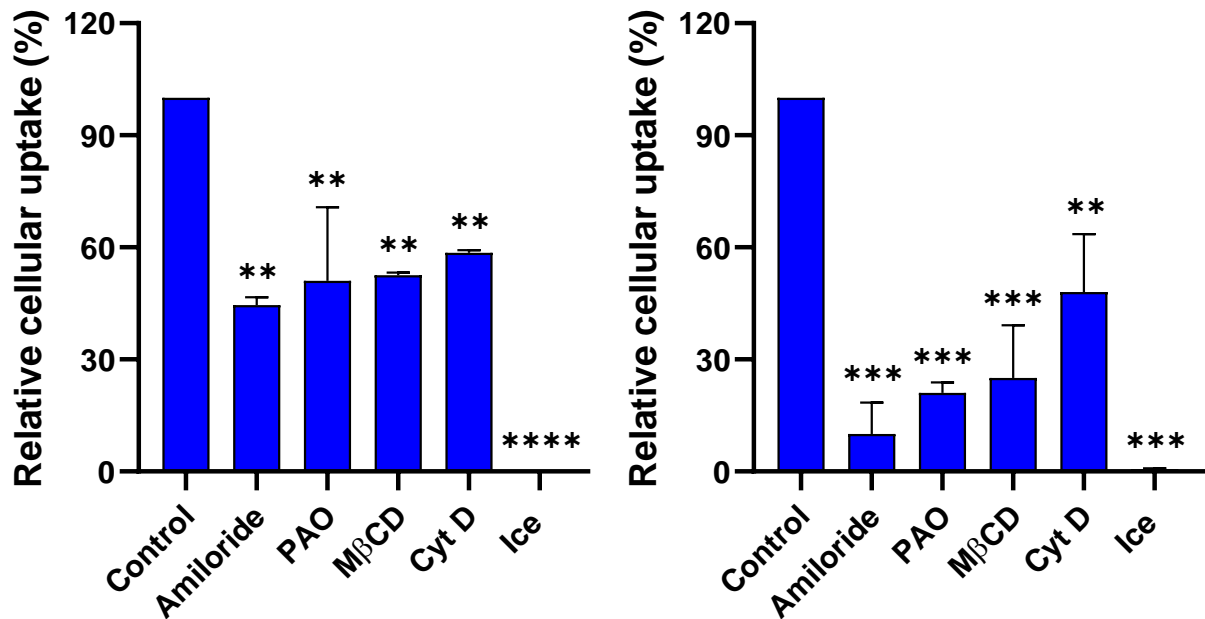
Figure 5.3.3 - FACS quantitative analyses of the influence of pathway-specific inhibitors on orange-emitting $(\text{CdSe/ZnS})_A$ (A) and green-emitting $(\text{CdSe/ZnS})_B$ (B) QDs uptake.



RAW cells were pre-incubated with different inhibitors, such as amiloride, phenyl arsine oxide (PAO), methyl-beta-cyclodextrin (M β CD), cytochalasin D (Cyt D), and 4 °C, for 1 h, then exposed to Qs for additional 3 hours. The cells were washed by PBS, harvested by trypsinization and suspended in PBS. The samples were read by FACS, exploiting three different lasers i.e., violet ($\lambda = 405$ nm), blue ($\lambda = 488$ nm), and yellow-green ($\lambda = 561$ nm), and the change in fluorescence intensity was recorded at PE-Cy-7 channel for $(\text{CdSe/ZnS})_A$ and Alexa Fluor 488 channel for $(\text{CdSe/ZnS})_B$, respectively. The diversity in profiles reflects the contribution of cellular pathways responsible for QDs uptake. The

inset of images A and B shows the autofluorescence (a), control positive (b), and change in fluorescence intensity in the presence of amiloride (c), PAO (d), M β CD (e), Cyt D (f), 4 °C (g), and joint histogram (h), respectively.

Figure 5.3.4 - Effect of pathway-specific inhibitors on orange-emitting (CdSe/ZnS)_A (left) and green-emitting (CdSe/ZnS)_B (right) QDs.



RAW cells were pre-treated with each inhibitor (i.e., sucrose, methyl-beta-cyclodextrin (CD), phenylarsine oxide (PAO), cytochalasin D (Cyto D) and ice) for 1 h, and then treated with QD (50 μ g/mL) for additional 4 h. The samples were read by FACS, and the data were analyzed by Flowjo software. Cells not treated with inhibitors were used as positive control. n = 2, *p \leq 0.05; **p \leq 0.01; ***p \leq 0.001; ****p \leq 0.0001.

Conclusively, the findings suggest the three major pathways are responsible for the uptake of (CdSe/ZnS)_B and (CdSe/ZnS)_A except for the difference in the amount of QDs internalized: the pathways include micropinocytosis, clathrin-mediated endocytosis, and caveolae-mediated endocytosis. No significantly detectable signal was observed for (CdSe/ZnS)_B and (CdSe/ZnS)_A at lower temperature treatment, which is consistent with energy-dependent endocytosis.

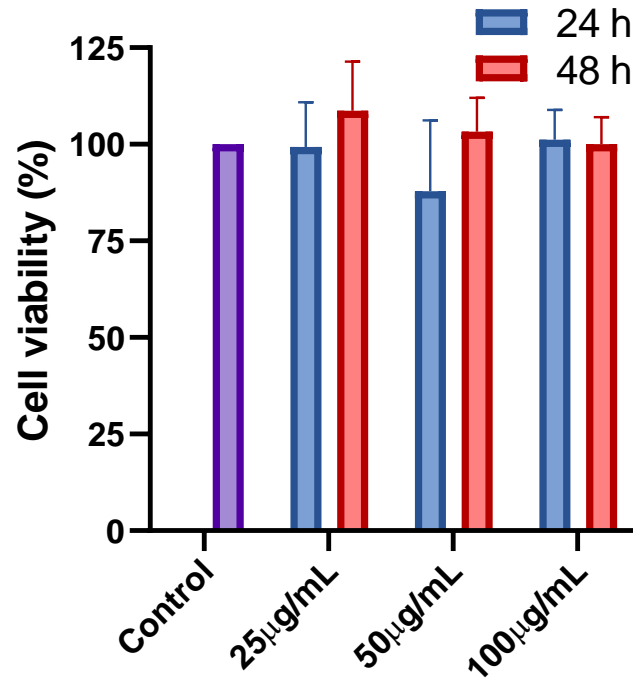
5.4. Developing the Red-emitting CdS/ZnS Core-Shell QDs Based Nanoprobe For Macrophages

The current work aims to explore the red-emitting CdS/ZnS core-shell QDs for developing bionanoprobe used for the bioanalysis and the diagnosis of macrophages-mediated disorders. The QDs were synthesized *via* the high-temperature organo-metals procedure, converted to water-soluble by ligand exchange approach, and determined their physicochemical and photoluminescent properties, exploiting various characterization techniques. The QDs were studied in the biological system of a murine macrophage cell line, RAW 264.7, and determined their effect on cell viability, qualitative detection by fluorescence imaging and FACS, and the mechanism underlying cellular internalization. The QDs presented good colloidal stability in the biological medium and chemical stability in the physiological environment, high cell viability, and intense fluorescence imaging. The internalization of QDs was nearly completely halted at a lower temperature (4 °C) consistent with energy-dependent endocytosis. It was observed that cellular uptake was predominantly facilitated by clathrin and caveolae-mediated endocytosis. Based on the initial findings, the QDs can be useful to develop biocompatible and sensitive bionanoprobe for site-specific analyses and diagnosis of macrophage-functional abnormality or macrophages-mediated disorders.

5.4.1. Cytotoxicity Assessment of QDs

MTT assay was conducted to determine the cell viability QDs at a concentration of 100 µg/mL treated for 24 hours. The assay did not identify any significant discrepancy between the treated and untreated (negative control), suggesting that the QDs are highly biocompatible, as shown in **Figure 5.4.1**. Usually, Cd-based are considered cytotoxic; therefore, the high cell viability can be explained by surface passivation of CdSe by non-toxic ZnS that protects the core from exposure to acidic cellular environment and hence hinders the degradation and leaching of Cd²⁺ ions [144], [145].

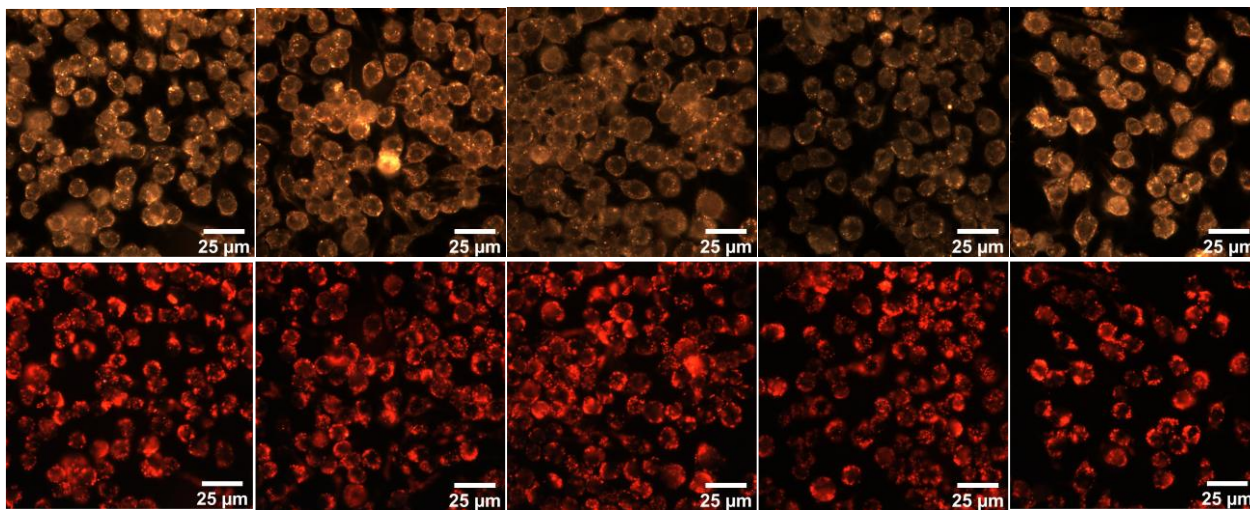
Figure 5.4.1 - Effect of CdS/ZnS QDs (25, 50, and 100 $\mu\text{g/mL}$) on the cell viability of RAW macrophages incubated for 24 and 48 hours.



5.4.2. Fluorescence Imaging of Cells

The study of live RAW macrophages imaging was conducted at a concentration of 100 $\mu\text{g/mL}$ QDs incubated for 24 hours. The photoluminescent images were obtained by CytoViva enhanced dark-field and dual-mode fluorescence imaging system exciting the QDs at $\lambda = 390\text{-}440$ nm. To confirm the cellular uptake of QDs, fluorescence imaging of live cells was performed, as shown in **Figure 5.4.2**. The QDs were visualized in the vicinity of the cell membrane and nucleus both in aggregates and non-aggregates, as evident from the background fluorescence of cells. The QDs presented intense fluorescence emission inside the cells after 24 h of incubation, which is the manifestation of higher chemical stability in the physiological environment and biocompatibility of QDs.

Figure 5.4.2 –CytoViv enhanced dark-field and dual-mode fluorescence images of live RAW cells treated with red-emitting CdS/ZnS QDs.



RAW cells were treated with QDs (100 $\mu\text{g/mL}$) for 24 hours. The cells were washed by PBS, mounted on a slide, and visualized by CytoViva microscope. The upper row shows the CytoViva enhanced dark-field images and the lower row shows dual-mode fluorescence images of cells.

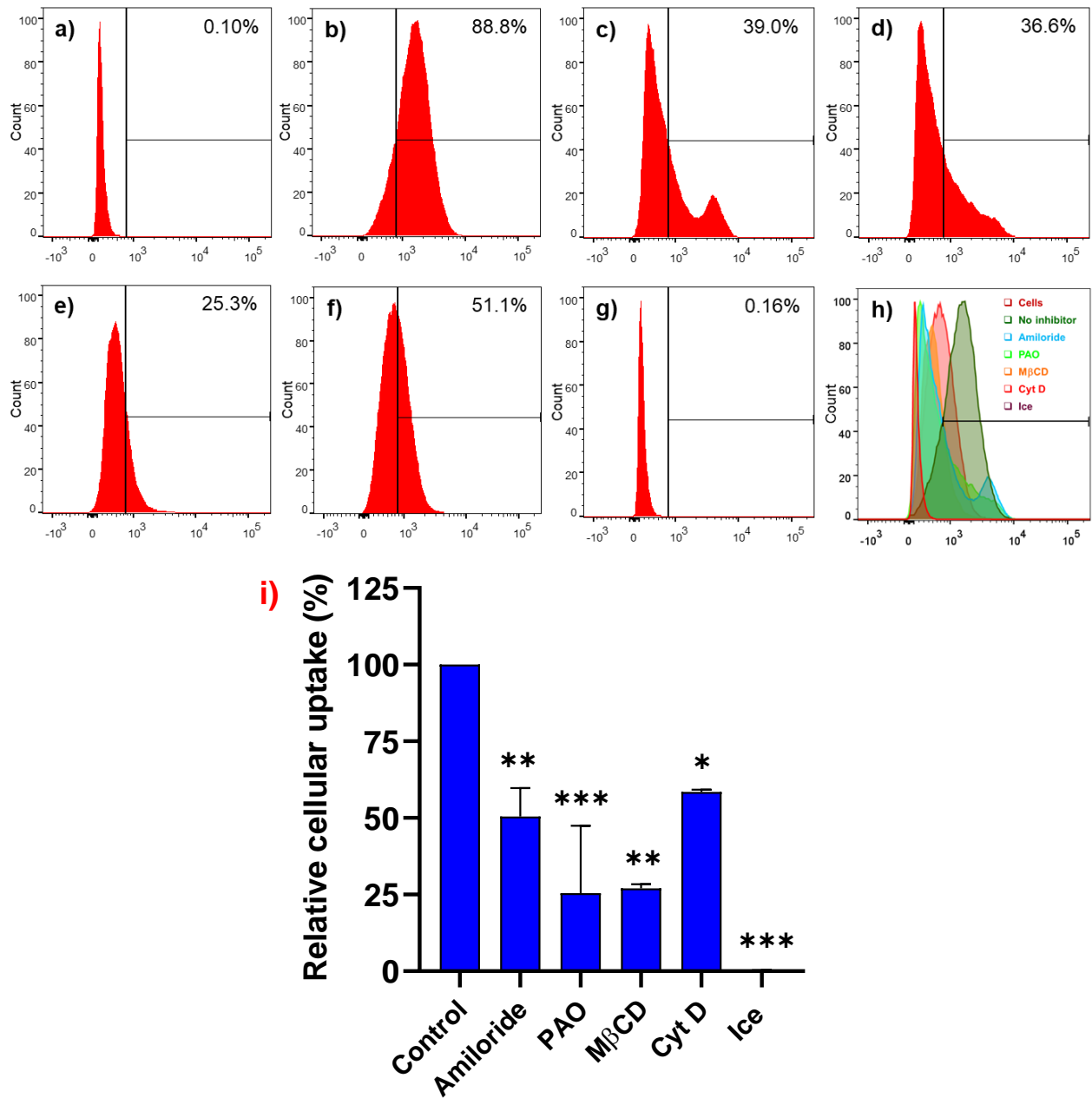
5.4.3. Cellular Uptake Mechanism of QDs

The study aims to unravel the specific pathway involved in the uptake of QDs of size 5.6 nm in our system. Cellular endocytosis usually proceeds *via* different pathways consistent to the threshold radius of particles: such as >0.500 nm *via* phagocytosis and pinocytosis; 100-200 nm *via* clathrin-mediated endocytosis; 50-80 nm *via* caveolin-mediated endocytosis, and 40-50 nm *via* clathrin- and caveolae independent endocytosis (40-50 nm) [82], [89], [136]–[139], [142], [143].

To elucidate the uptake mechanism, different endocytosis inhibitory drugs were selected: Cyt D to block the phagocytosis; M β CD to block the caveolae-mediated endocytosis; PAO to block the clathrin-mediated endocytosis; amiloride to block the macropinocytosis; and low temperature which is a general inhibitor of energy-dependent uptake mechanisms. The systematic analyses of endocytosis accomplished by FACS (**Figure 5.4.3a-h**) presented considerable inhibition of QDs with PAO and M β CD drugs, indicating that the QDs are majorly endocytosed by clathrin- and caveolae-mediated endocytosis, respectively (**Figure 5.4.3i**). The PAO comparatively contributed to strong inhibition of QDs uptake, which signifies that the endocytosis is more facilitated by clathrin-mediated endocytosis. M β CD drugs also induced a considerable decline in QDs uptake, manifesting that endocytosis is carried out to a large extent by the caveolae-mediated pathway. However, amiloride and Cyt D comparatively showed weak inhibition, which is the signature of QDs internalization by

macropinocytosis and phagocytosis, even though the pathways are generally involved in the uptake of fluid and larger particles. At lower temperature (4 °C), the cellular uptake of QDs was completely blocked, which is the hallmark of energy-dependent endocytosis.

Figure 5.4.3 – FACS analyses of the effect of pathway-specific inhibitors on red-emitting CdS/ZnS QDs.



RAW cells were pre-incubated with different inhibitors such as amiloride, phenylarsine oxide (PAO), methyl-beta-cyclodextrin (M β CD), cytochalasin D (Cyt D), and 4 °C, for 1 h, then exposed to QDs (50

$\mu\text{g/mL}$) for additional 4 hours. The cells were washed by PBS, harvested by trypsinization and suspended in PBS. The samples were read by FACS, exploiting three different lasers i.e., violet (λ) = 405 nm, blue (λ) = 488 nm, and yellow-green (λ) = 561 nm, and the change in fluorescence intensity was recorded at BV 605 channel. The diversity in profiles reflects the contribution of cellular pathways responsible for QDs uptake. The inset of images B shows the autofluorescence (a), control positive (b), amiloride (c), PAO (d), M β CD (e), Cyt D (f), 4 °C (g), joint histogram (h), and graphical illustration of QDs uptake inhibition, respectively. Cells not treated with inhibitors were used as positive control. n = 2, *p \leq 0.05; **p \leq 0.01; ***p \leq 0.001; ****p \leq 0.0001.

Chapter 6

CONCLUSION AND PERSPECTIVES

6.1 Conclusion

Over the past few decades, nanotechnology has revolutionized medicine, especially concerning improving the diagnostics and therapeutics efficiency. Among the nanomaterials, QDs have drawn considerable attention due to their optoelectronic and photoluminescence versatility, and can be used as bioanoprobe in site-specific analyses and diagnosis of macrophage-mediated disorders such as atherosclerosis, obesity, autoimmune diseases, etc.

The precise knowledge of cellular uptake mechanism and its kinetic, intracellular trafficking, subcellular localization and fate, biocompatibility, colloidal and photoluminescence stability, and detection sensitivity of QDs, plays a crucial role to enhance the diagnostic sensitivity and theranostics efficiency of the new generation bioanoprobe. In this work, a range of color-tunable QDs were synthesized and studied their physicochemical and photoluminescent properties. Their surface chemistry was transformed to become soluble in aqueous-solutions and cell culture medium. The detailed study of the physicochemical and photoluminescence properties of QDs, including orange-emitting ZnSe:Mn²⁺, multicolor-fluorescence ZnSe:Eu²⁺/Mn²⁺@ZnS, color-tunable CdSe/ZnS, and CdS/ZnS showed good colloidal stability in water and RPMI culture medium supplemented with 10% FBS, intense emission (ranging from blue to red), high crystallinity, cubic zinc-blende phase, small size (4-7 nm), and broad negative zeta potential (ranging from -8 to -69 mV). We studied the effect of these QDs on the cell viability, fluorescence imaging, and mechanism underlying the cellular uptake in the model of a cell line of macrophages (RAW 264.7) for bioanalysis, biomedical, and clinical diagnostic applications.

The cytotoxicity assessment of QDs in RAW macrophages did not confirm any deleterious effect to cell viability, suggesting that QDs are highly biocompatible in the biological system. The RAW cells endocytosed a sufficient amount of QDs efficiently and gave highly intense fluorescence signals in the intracellular environment, which enabled the cells to be easily detected and quantified by CytoViva® enhanced dark-field and dual mode fluorescence (DMF) imaging system and by FACS, respectively. The cells treated with ZnSe:Eu²⁺/Mn²⁺@ZnS QDs displayed color-tunable fluorescence images at different excitation wavelengths. This unique intrinsic feature of QDs can be utilized for site-specific analyses by enhancing the value of the signal to noise ratio *via* modulating and tuning the emission color.

The systematic study of endocytosis by FACS showed that at a lower temperature (4 °C), cellular uptake of QDs was extensively depleted or completely blocked in some cases, consistent

with energy-dependent endocytosis mechanism. The QDs were observed to adhere to cell membranes singly and aggregately surrounded by membrane protrusions before being internalized by cells, indicating the involvement of endocytosis. Furthermore, we found that RAW cells executed endocytosis cells *via* different pathways for different particles. However, clathrin and caveolae-mediated endocytosis were identified as the most dominant entry pathways, as expected. The cellular uptake of ZnSe:Mn²⁺ was predominantly facilitated *via* clathrin and caveolae-mediated endocytosis. The ZnSe:Eu²⁺/Mn²⁺@ZnS QDs were predominantly internalized *via* caveolae-mediated endocytosis and macropinocytosis. The endocytosis of (CdSe/ZnS)_A was relatively executed *via* all the entry pathways, including micropinocytosis, clathrin, and caveolae-mediated endocytosis, and phagocytosis whereas the (CdSe/ZnS)_B was predominantly internalized *via* macropinocytosis and clathrin-mediated endocytosis. In the case of CdS/ZnS QDs, clathrin-and caveolae-mediated endocytosis contributed to the major cellular uptake. The apparent diversity in uptake pathways for specific QDs of nearly similar ultrasmall size (4-7 nm) can be due to the dominance of surface features of QDs, especially the zeta potential and colloidal stability. Our results suggest that such magnificent physicochemical and photoluminescence properties, good colloidal stability in the biological media, high cell viability, chemical stability in the physiological environment, enhanced fluorescence bioimaging, and energy-dependent specific entry pathway of QDs would be helpful, comparing to traditional organic dyes and proteins fluorochrome, to enhance the diagnostic sensitivity and develop a new generation bionanoprobe used for the monitoring, tracking and diagnosis of the macrophages-mediated disorders.

6.1 Perspectives

- Evaluation of the bionanoprobe *in vivo* model system.
- The exploitation of nanoprobe for the early detection of defects in the innate defense system (e.g. Reticule endothelial system (RES)).
- Functional analysis of abnormal macrophages and diagnosis of macrophages-mediated inflammatory mediated disorders such as atherosclerosis, obesity, autoimmune diseases, etc.
- Choice of the read-out method (e.g. tumor vs normal cells).
- Determination of sensitivity (e.g. minimum number of cells for signal).
- Clinical evaluation.

Chapter 7

REFERENCES

REFERENCES

- [1] Ali, M.; Zayed, D.; Ramadan, W.; Kamel O. A.; Shehab, M.; Ebrahim S. Synthesis, characterization and cytotoxicity of polyethylene glycol-encapsulated CdTe quantum dots. *Int. Nano Lett.*, vol. 9, no. 1, pp. 61–71, 2019.
- [2] Khan, L. U.; Khan, Z. U. Bifunctional nanomaterials: Magnetism, luminescence and multimodal biomedical applications. *Complex Magn. Nanostructures Synth. Assem. Appl.*, p. 121–171, 2017.
- [3] Mayor, S.; Pagano, R. E. Pathways of clathrin-independent endocytosis. *Nat. Rev. Mol. Cell Biol.*, vol. 8, no. 8, p. 603–612, 2007.
- [4] Yang, T.; Tang, Y.; Liu, L.; Lv, X.; Wang, Q.; Ke, H.; Deng, Y.; Yang, H.; Yang, X.; Liu, G.; Zhao, Y.; Chen, H. Size-Dependent Ag₂S Nanodots for Second Near-Infrared Fluorescence/Photoacoustics Imaging and Simultaneous Photothermal Therapy. *ACS Nano.*, vol. 11, no. 2, p. 1848–1857, 2017.
- [5] Wu, Q.; Chu, M.; Shao, Y.; Wo, F.; Shi, D. Reduced graphene oxide conjugated with CuInS₂/ZnS nanocrystals with low toxicity for enhanced photothermal and photodynamic cancer therapies. *Carbon N. Y.*, vol. 108, p. 21–37, 2016.
- [6] Farkhani, S. M.; Valizadeh, A.; Review: Three synthesis methods of CdX (X = Se, S or Te) quantum dots. *IET Nanobiotechnology.*, vol. 8, no. 2, p. 59–76, 2014.
- [7] Mir, I. A.; Radhakrishanan, V. S.; Rawat, K.; Prasad, T.; Bohidar, H. B. Bandgap tunable AgInS based quantum dots for high contrast cell imaging with enhanced photodynamic and antifungal applications. *Sci. Rep.*, vol. 8, no. 1, p. 1–12, 2018.
- [8] Martynenko I. V.; Litvin, A. P.; Purcell-Milton, F.; Baranov, A. V.; Fedorov, A. V.; Gun Y. K. Application of semiconductor quantum dots in bioimaging and biosensing. *J. Mater. Chem. B.*, vol. 5, no. 33, p. 6701–6727, 2017.
- [9] Nandan, Y.; Mehata, M. S. Wavefunction Engineering of Type-I/Type-II Excitons of CdSe/CdS Core-Shell Quantum Dots. *Sci. Rep.*, vol. 9, no. 1, p. 1–11, 2019.

- [10] Maity, P.; Ghosh, H. N. Strategies for extending charge separation in colloidal nanostructured quantum dot materials. *Phys. Chem. Chem. Phys.*, vol. 21, no. 42, p. 23283–23300, 2019.
- [11] Ca, N.X.; Hien, N.T.; Tan, P.M.; Phan, T.L.; Thanh, L.D.; Do, P.V.; Bau, N.Q.; Lien, V.T.K.; Van, H.T Tunable dual emission in type-I/type-II CdSe/CdS/ZnSe nanocrystals. *J. Alloys Compd.*, vol. 791, p. 144–151, 2019.
- [12] Bera D.; Qian, L.; Tseng, T. K.; Holloway, P. H. Quantum dots and their multimodal applications: A review. *Materials (Basel)*., vol. 3, no. 4, p. 2260–2345, 2010.
- [13] Online V. A.; Chang, J.; Waclawik, E. R. Colloidal semiconductor nanocrystals : controlled synthesis and surface chemistry in organic media. *RSC Adv.*, vol. 4, no. 45, p. 23505–23527, 2014.
- [14] Girma, W. M.; Fahmi, M. Z.; Permadi, A.; Abate, M. A.; Chang, J. Y. Synthetic strategies and biomedical applications of I-III-VI ternary quantum dots. *J. Mater. Chem. B.*, vol. 5, no. 31, p. 6193–6216, 2017.
- [15] Toufanian, R.; Piryatinski, A.; Mahler, A. H.; Iyer, R.; Hollingsworth, J. A.; Dennis, A. M. Bandgap engineering of indium phosphide-based core/shell heterostructures through shell composition and thickness. *Front. Chem.*, vol. 6, no. NOV, p. 1–12, 2018.
- [16] Dennis, A. M.; Mangum, B. D.; Piryatinski, A.; Park, Y.; Hannah, D. C.; Casson, J. L.; Darrick Williams, J.; Schaller, R. D.; Htoon, H.; Hollingsworth, J. A. Suppressed blinking and auger recombination in near-infrared type-II InP/CdS nanocrystal quantum dots. *Nano Lett.*, vol. 12, no. 11, p. 5545–5551, 2012.
- [17] Kim, S.; Park, J.; Kim, T.; Jang, E.; Jun, S.; Jang, H.; Kim, B.; Kim, S. Reverse Type-I ZnSe/InP/ZnS Core/Shell/Shell nanocrystals: Cadmium-free quantum dots for visible luminescence. *Small.*, vol. 7, no. 1, p. 70–73, 2011.
- [18] Jing, L.; Kershaw, S. V.; Kipp, T.; Kalytchuk, S.; Ding, K.; Zeng, J.; Jiao, M.; Sun, X.; Mews, A.; Rogach, A. L.; Gao, M. Insight into strain effects on band alignment shifts, carrier localization and recombination kinetics in CdTe/CdS core/shell quantum dots. *J.*

- Am. Chem. Soc.*, vol. 137, no. 5, p. 2073–2084, 2015.
- [19] Chang, J. Y.; Wang, S. R.; Yang, C. H. Synthesis and characterization of CdTe/CdS and CdTe/CdSe core/shell type-II quantum dots in a noncoordinating solvent. *Nanotechnology*, vol. 18, no. 34, p. 345602–345608, 2007.
- [20] Bang, J.; Park, J.; Lee, J. H.; Won, N.; Nam, J.; Lim, J.; Chang, B. Y.; Lee, H. J.; Chon, B.; Shin, J.; Park, J. B.; Choi, J. H. Cho, K.; Park, S. M.; Joo, T.; Kim, S. ZnTe/ZnSe (core/shell) type-II quantum dots: Their optical and photovoltaic properties. *Chem. Mater.*, vol. 22, no. 1, p. 233–240, 2010.
- [21] Zeng, Q.; Kong, X.; Sun, Y.; Zhang, Y.; Tu, L.; Zhao, J.; Zhang, H. Synthesis and optical properties of type II CdTe/CdS core/shell quantum dots in aqueous solution via successive ion layer adsorption and reaction. *J. Phys. Chem. C.*, vol. 112, no. 23, p. 8587–8593, 2008.
- [22] Kim, S.; Fisher, B.; Eisler, H. J.; Bawendi, M. Type-II quantum dots: CdTe/CdSe(core/shell) and CdSe/ZnTe(core/shell) heterostructures. *J. Am. Chem. Soc.*, vol. 125, no. 38, p. 11466–11467, 2003.
- [23] Zeng, R.; Zhang, T.; Liu, J.; Hu, S.; Wan, Q.; Liu, X.; Peng, Z.; Zou, B. Aqueous synthesis of type-II CdTe/CdSe core-shell quantum dots for fluorescent probe labeling tumor cells. *Nanotechnology*, vol. 20, no. 9, p. 095102–095110, 2009.
- [24] Chuang, C. H.; Lo, S. S.; Scholes, G. D.; Burda, C. Charge separation and recombination in CdTe/CdSe core/shell nanocrystals as a function of shell coverage: Probing the onset of the quasi type-II regime. *J. Phys. Chem. Lett.*, vol. 1, no. 17, p. 2530–2535, 2010.
- [25] Makkar, M.; Viswanatha, R.; Frontier challenges in doping quantum dots: Synthesis and characterization. *RSC Adv.*, vol. 8, no. 39, p. 22103–22112, 2018.
- [26] Soumya, S.; Sheemol, V. N.; Amba, P.; Mohamed, A. P.; Ananthakumar S. Sn and Ag doped ZnO quantum dots with PMMA by in situ polymerization for UV/IR protective, photochromic multifunctional hybrid coatings. *Sol. Energy Mater. Sol. Cells*, vol. 174, no. 9, p. 554–565, 2018.

- [27] Sakthivel, P.; Venkatesan, G. K. D. P.; Subramaniam, K. Structural and optical properties of ZnO . 98T0 . 02S (T = Mn , Cu , Ni , Co , Cr , Cd & Sn) quantum dots : A comparative study. *AIP Conference Proceedings.*, vol. 020040, no. 4, p. 0–4, 2019.
- [28] Wu, P.; Yan, X. P. Doped quantum dots for chemo/biosensing and bioimaging. *Chem. Soc. Rev.*, vol. 42, no. 12, p. 5489–5521, 2013.
- [29] Archer P. I.; Santangelo, S. A.; Gamelin, D. R. Direct observation of sp-d exchange interactions in colloidal Mn²⁺ - And Co²⁺ -doped CdSe quantum dots. *Nano Lett.*, vol. 7, no. 4, p. 1037–1043, 2007.
- [30] Dethlefsen, J. R.; Mikhailovsky, A. A.; Burks, P. T.; Døssing, A.; Ford, P. C. Lanthanide modification of CdSe/ZnS core/shell quantum dots. *J. Phys. Chem. C.*, vol. 116, no. 44, p. 23713–23720, 2012.
- [31] Wei, X.; Wang, W.; Chen, K. Preparation and characterization of ZnS:Tb,Gd and ZnS:Er,Yb,Gd nanoparticles for bimodal magnetic-fluorescent imaging. *Dalt. Trans.*, vol. 42, no. 5, p. 1752–1759, 2013.
- [32] Ribeiro, R. T.; Dias, J. M. M.; Pereira, Gi. A.; Freitas, D. V.; Monteiro, M.; Filho, P. E. C.; Raelle, R. A.; Fontes, A.; Navarro, M.; Santos, B. S. Electrochemical synthetic route for preparation of CdTe quantum-dots stabilized by positively or negatively charged ligands. *Green Chem.*, vol. 15, no. 4, p. 1061–1066, 2013.
- [33] Steigerwald, M. L.; Brus, L. E. Semiconductor Crystallites: A Class of Large Molecules. *Acc. Chem. Res.*, vol. 23, no. 6, p. 183–188, 1990.
- [34] Murray, C. B.; Norris, D. J.; Bawendi, M. G. Synthesis and Characterization of Nearly Monodisperse CdE (E = S, Se, Te) Semiconductor Nanocrystallites. *J. Am. Chem. Soc.*, vol. 115, no. 19, p. 8706–8715, 1993.
- [35] Lv, G.; Guo, W.; Zhang, W.; Zhang, T.; Li, S.; Chen, S.; Eltahan, A. S.; Wang, D.; Wang, Y.; Zhang, J.; Wang, P. C.; Chang, J.; Liang, X. Near-Infrared Emission CuInS/ZnS Quantum Dots: All-in-One Theranostic Nanomedicines with Intrinsic Fluorescence/Photoacoustic Imaging for Tumor Phototherapy. *ACS Nano.*, vol. 10, no.

- 10, p. 9637–9645, 2016.
- [36] Amiens, C.; Chaudret, B.; Ciuculescu-Pradines, D.; Collie`re, V.; Fajerweg, K.; Fau, P.; Kahn, M.; Maisonnat, A.; Soulanticac, K.; Philippot, K. Organometallic approach for the synthesis of nanostructures. *New J. Chem.*, vol. 37, no. 11, p. 3374–3401, 2013.
- [37] Li, H.; Wang, C.; Peng, Z.; Fu, X. A Review on the Synthesis Methods of CdSeS-Based Nanostructures. *J. Nanomater.*, vol. 2015, p. 1-16, 2015.
- [38] Hu, M. Z.; Zhu, T. Semiconductor Nanocrystal Quantum Dot Synthesis Approaches Towards Large-Scale Industrial Production for Energy Applications. *Nanoscale Res. Lett.*, vol. 10, no. 1, p. 1–15, 2015.
- [39] Pu, Y.; Cai, F.; Wang, D.; Wang, J. X.; Chen, J. F. Colloidal Synthesis of Semiconductor Quantum Dots toward Large-Scale Production: A Review. *Ind. Eng. Chem. Res.*, vol. 57, no. 6, p. 1790–1802, 2018.
- [40] Crouch, D. J.; O'brien, P.; Malik, M. A.; Skabara, P. J.; Wright, S. P. A one-step synthesis of cadmium selenide quantum dots from a novel single source precursor. *Chem. Commun.*, vol. 3, no. 12, p. 1454–1455, 2003.
- [41] Zhang, W.; Zhang, H.; Feng, Y.; Zhong, X. Scalable Single-Step Noninjection Synthesis of High-Quality Core / Shell Quantum Dots with Emission Tunable from Violet to Near Infrared. *ACS Nano.*, vol. 6, no. 12, p. 11066–11073, 2012.
- [42] Ma, Y.; Zhang, Y.; Yu, W. Near Infrared Emitting Quantum Dots: Synthesis, Luminescent Properties and Applications. *J. Mater. Chem. C.*, p. 13662–13679, 2019.
- [43] Che, O.; Zhao, J.; Chauhan, V. P.; Cui, J.; Wong, C.; Harris, D. K.; Wei, H.; Han, H.; Fukumura, D.; Jain, R. K.; Bawendi, M. G. Compact high-quality CdSe-CdS core-shell nanocrystals with narrow emission linewidths and suppressed blinking. *Nat. Mater.*, vol. 12, no. 5, p. 445–451, 2013.
- [44] Law, W.; Yong, K.; Roy, I.; Ding, H.; Hu, R.; Zhao, W.; Prasad, P. N. Aqueous-phase synthesis of highly luminescent CdTe/ZnTe core/shell quantum dots optimized for targeted bioimaging. *Small*, vol. 5, no. 11, p. 1302–1310, 2009.

- [45] Wang, Y.; Si, B.; Lu, S.; Ma, X.; Liu, E.; Fan, J.; Li, X.; Hu, X. Effective improvement in optical properties of colloidal CdTe@ZnS quantum dots synthesized from aqueous solution. *Nanotechnology.*, vol. 27, no. p. 36, 365707- 365716, 2016.
- [46] Kalyuzhny, G.; Murray, R. W. Ligand effects on optical properties of CdSe nanocrystals. *J. Phys. Chem. B.*, vol. 109, no. 15, p. 7012–7021, 2005.
- [47] Rogach, A. L.; Katsikas, L.; Kornowski, A.; Dangsheng, S.; Eychmüller, A.; Weller, H. Synthesis and characterization of thiol-stabilized CdTe nanocrystals. *Berichte der Bunsengesellschaft/Physical Chem. Chem. Phys.*, vol. 100, no. 11, p. 1772–1778, 1996.
- [48] Zhang, H.; Wang, C.; Li, M.; Ji, X.; Zhang, J.; Yang, B. Fluorescent nanocrystal-polymer composites from aqueous nanocrystals: Methods without ligand exchange. *Chem. Mater.*, vol. 17, no. 19, p. 4783–4788, 2005.
- [49] Deng, D.; Zhang, W.; Chen, X.; Liu, F.; Zhang, J.; Gu, Y.; Hong, J. Facile synthesis of high-quality, water-soluble, near-infrared-emitting PbS quantum dots. *Eur. J. Inorg. Chem.*, no. 23, p. 3440–3446, 2009.
- [50] Brichkin, S. B.; Razumov, V. F. Colloidal quantum dots: synthesis, properties and applications. *Russ. Chem. Rev.*, vol. 85, no. 12, p. 1297–1312, 2016.
- [51] Kapatkar, P. S.; Shettar, R. B.; Kapatkar, S. B.; Patil, N. R. Synthesis, Structural and Optical Investigation of CdSe semiconductor Quantum Dots. *IOP Conf. Ser. Mater. Sci. Eng.*, vol. 360, no. 1, p. 012009, 2018.
- [52] Li, Z.; Dong, C.; Tang, L.; Zhu, X.; Chen, H.; Ren, J. Aqueous synthesis of CdTe/CdS/ZnS quantum dots and their optical and chemical properties. *Luminescence*, vol. 26, no. 6, p. 439–448, 2011.
- [53] Liu, X.; Ma, C.; Yan, Y.; Yao, G.; Tang, Y.; Huo, P.; Shi, W.; Yan, Y. Hydrothermal synthesis of CdSe quantum dots and their photocatalytic activity on degradation of cefalexin. *Ind. Eng. Chem. Res.*, vol. 52, no. 43, p. 15015–15023, 2013.
- [54] Ummartyotin, S.; Infahsaeng, Y. A comprehensive review on ZnS: From synthesis to an approach on solar cell. *Renew. Sustain. Energy Rev.*, vol. 55, p. 17–24, 2016.

- [55] Mirzaie, M.; Khanbabaie, R.; Jahanshahi, M.; Darzi, G. N. Preparation , Optimization , and Characterization of CuInS₂ quantum dots by a D-optimal Design. vol. 3, no. 4, p. 311–320, 2018.
- [56] Nishimura, H.; Lin, Y.; Hizume, M.; Taniguchi, T.; Shigekawa, N.; Takagi, T.; Sobue, S.; Kawai, S.; Okuno, E.; Kim, D. Hydrothermal synthesis of ZnSe:Mn quantum dots and their optical properties. *AIP Adv.*, vol. 9, no. 2, p. 25223-25230, 2019.
- [57] Mao, W.; Guo, J.; Yang, W.; Wang, C.; He, J.; Chen, J. Synthesis of high-quality near-infrared-emitting CdTeS alloyed quantum dots via the hydrothermal method. *Nanotechnology*, vol. 18, no. 48, p. 48561-4811568, 2007.
- [58] Aboulaich, A.; Billaud, D.; Abyan, M.; Balan, L.; Gaumet, J.; Medjadhi, G.; Ghanbaja, J.; Schneider, R. One-pot noninjection route to CdS quantum dots via hydrothermal synthesis. *ACS Appl. Mater. Interfaces*, vol. 4, no. 5, p. 2561–2569, 2012.
- [59] Bruna, N.; Collao, B.; Tello, A.; Caravantes, P.; Díaz-Silva, N.; Monrás, J. P.; ÓrdenesAenishanslins, N.; Flores, M.; Espinoza-Gonzalez, R.; Bravo, D.; Pérez-Donoso, J. M. Synthesis of salt-stable fluorescent nanoparticles (quantum dots) by polyextremophile halophilic bacteria. *Sci. Rep.*, vol. 9, no. 1, p. 1–13, 2019.
- [60] Gallardo-Benavente, C.; Carrión, O.; Todd, J. D.; Pieretti, J. C.; Seabra, A. B.; Durán, N.; Rubilar, O.; Pérez-Donoso, J. M.; Quiroz, A. Biosynthesis of cds quantum dots mediated by volatile sulfur compounds released by antarctic pseudomonas fragi. *Front. Microbiol.*, vol. 10, no. 8, p. 1–15, 2019.
- [61] Bao, H.; Hao, N.; Yang, Y.; Zhao, D. Biosynthesis of biocompatible cadmium telluride quantum dots using yeast cells. *Nano Res.*, vol. 3, no. 7, p. 481–489, 2010.
- [62] Bao, H.; Lu, Z.; Cui, X.; Qiao, Y.; Guo, J.; Anderson, J. M.; Li, C. M. Extracellular microbial synthesis of biocompatible CdTe quantum dots. *Acta Biomater.*, vol. 6, no. 9, p. 3534–3541, 2010.
- [63] Zhou, J.; Yang, Y.; Zhang, C. Y. Toward Biocompatible Semiconductor Quantum Dots: From Biosynthesis and Bioconjugation to Biomedical Application. *Chem. Rev.*, vol.

115, no. 21, p. 11669–11717, 2015.

- [64] Yun, H. J.; Paik, T.; Edley, M. E.; Baxter, J. B.; Murray, C. B. Enhanced charge transfer kinetics of CdSe quantum dot-sensitized solar cell by inorganic ligand exchange treatments. *ACS Appl. Mater. Interfaces.*, vol. 6, no. 5, p. 3721–3728, 2014.
- [65] Oh, J. K. Surface modification of colloidal CdX-based quantum dots for biomedical applications. *J. Mater. Chem.*, vol. 20, no. 39, pp. 8433–8445, 2010.
- [66] Hatakeyama, M.; Kishi, H.; Kita, Y.; Imai, K.; Nishio, K.; Karasawa, S.; Masaike, Y.; Sakamoto, S.; Sandhu, A.; Tanimoto, A.; Gomi, T.; Kohda, E.; Abea, M.; Handa, H. A two-step ligand exchange reaction generates highly water-dispersed magnetic nanoparticles for biomedical applications. *J. Mater. Chem.*, vol. 21, no. 16, p. 5959–5966, 2011.
- [67] Drbohlavova, J.; Adam, V.; Kizek, R.; Hubalek, J. Quantum dots - characterization, preparation and usage in biological systems. *Int. J. Mol. Sci.*, vol. 10, no. 2, p. 656–673, 2009.
- [68] Yu, W. W. Semiconductor quantum dots: Synthesis and water-solubilization for biomedical applications. *Expert Opin. Biol. Ther.*, vol. 8, no. 10, p. 1571–1581, 2008.
- [69] Ayoubi, M.; Naserzadeh, P.; Hashemi, M. T.; Rostami, M. R.; Tamjid, E.; Tavakoli, M. M.; Simchi, A. Biochemical mechanisms of dose-dependent cytotoxicity and ROS-mediated apoptosis induced by lead sulfide/graphene oxide quantum dots for potential bioimaging applications. *Sci. Rep.*, vol. 7, no. 1, p. 1–10, 2017.
- [70] Dong, H.; Tang, S.; Hao, Y.; Yu, H.; Dai, W.; Zhao, G.; Cao, Y.; Lu, H.; Zhang, X.; Ju, H. Fluorescent MoS₂ Quantum Dots: Ultrasonic Preparation, Up-Conversion and Down-Conversion Bioimaging, and Photodynamic Therapy. *ACS Appl. Mater. Interfaces.*, vol. 8, no. 5, p. 3107–3114, 2016.
- [71] He, T.; Qiu, X.; Li, J.; Pang, G.; Wu, Z.; Cheng, J.; Zhou, Z.; Hao, J.; Liu, H.; Ni, Y.; Li, L.; Lin, X.; Hu, W.; Wang, K.; Chen, R. Water-soluble chiral CdSe/CdS dot/rod nanocrystals for two-photon fluorescence lifetime imaging and photodynamic therapy.

Nanoscale., vol. 11, no. 32, p. 15245–15252, 2019.

- [72] Sun, J.; Guo, Y.; Zhu, L.; Yang, L.; Shi, W.; Wang, K.; Zhang, H. Photodynamic Therapy of Human Hepatoma Using Semiconductor Quantum Dots as Sole Photosensitizer. *Part. Part. Syst. Charact.*, vol. 34, no. 10, p. 1–10, 2017.
- [73] Bilan, R.; Nabiev, I.; Sukhanova, A. Quantum Dot-Based Nanotools for Bioimaging , Diagnostics , and Drug Delivery. *ChemBioChem.*, vol. 17, no. 22, p. 2103–2114, 2016.
- [74] Liu, N. Toxic effects and involved molecular pathways of nanoparticles on cells and subcellular organelles. no. March 2019, p. 16–36, 2020.
- [75] Martynenko, I. V.; Kuznetsova, V. A.; Orlova, A. O.; Kanaev, P. A.; Maslov, V. G.; Loudon, A.; Zaharov, V.; Parfenov, P.; Gun'ko, Y. K.; Baranov, A. V.; Fedorov, A. V. Chlorin e6-ZnSe/ZnS quantum dots based system as reagent for photodynamic therapy. *Nanotechnology.*, vol. 26, no. 5, p. 55102, 2015.
- [76] Martynenko, I. V.; Litvin, A. P.; Purcell-Milton, F.; Baranov, A. V.; Fedorov, A. V.; Gun'ko, Y. K. Application of Semiconductor Quantum Dots in Bioimaging and Biosensing. *J. Mater. Chem. B.*, vol. 5, no. 33, p. 7601–7627, 2017.
- [77] Yang, Y.; Mao, G.; Ji, X.; He, Z. DNA-Templated quantum dots and their applications in biosensors, bioimaging, and therapy. *J. Mater. Chem. B.*, vol. 8, no. 1, p. 9–17, 2019.
- [78] Xia, C.; Wang, W.; Du, L.; Rabouw, F. T.; van den Heuvel, D. J.; Gerritsen, H. C.; Mattoussi, H.; Donega, C. M. Förster Resonance Energy Transfer between Colloidal CuInS₂/ZnS Quantum Dots and Dark Quenchers. *J. Phys. Chem. C.*, vol. 124, no. 2, p. 1717–1731, 2020.
- [79] Rizvi, S. B.; Ghaderi, S.; Keshtgar, M.; Seifalian, A. M. Semiconductor quantum dots as fluorescent probes for in vitro and in vivo bio-molecular and cellular imaging. *Nano Rev.*, vol. 1, no. 1, p. 5161, 2010.
- [80] Chen, C.; Tian, R.; Zeng, Y.; Chu, C.; Liu, G. Activatable Fluorescence Probes for ‘ Turn-On ’ and Ratiometric Biosensing and Bioimaging : From NIR - I to NIR-II. *Bioconjugate Chem.*, vol. 31, no.2, p. 276–292, 2020.

- [81] Chinnathambi, S.; Shirahata, N. Recent advances on fluorescent biomarkers of near-infrared quantum dots for in vitro and in vivo imaging. *Sci. Technol. Adv. Mater.*, vol. 20, no. 1, p. 337–355, 2019.
- [82] Zhang, S.; Gao, H.; Bao, G. Physical Principles of Nanoparticle Cellular Endocytosis. *ACS Nano.*, vol. 9, no. 9, p. 8655–8671, 2015.
- [83] Castro, C. E.; Ribeiro, C. A.S.; Alavarse, A. C.; Albuquerque, L. J. C.; Silva, M. C.; Jager, C. E.; Surman, F.; Schmidt, V.; Giacomelli, C.; Giacomelli, F. C. Nanoparticle-Cell Interactions: Surface Chemistry Effects on the Cellular Uptake of Biocompatible Block Copolymer Assemblies. *Langmuir.*, vol. 34, no. 5, p. 2180–2188, 2018.
- [84] Zhao, J.; Stenzel, M. H. Entry of nanoparticles into cells: The importance of nanoparticle properties. *Polym. Chem.*, vol. 9, no. 3, p. 259–272, 2018.
- [85] Couteur, H. L.; McCourt, P. A. G.; Singla, N.; Kang, S. W. S.; Burgess, A.; Kuncic, Z.; Couteur, David, G. L.; Cogger, V. C. Rapid Intestinal Uptake and Targeted Delivery to the Liver Endothelium Using Orally Administered Silver Sulfide Quantum Dots. *ACS Nano.*, vol. 14, no. 2, p. 1492–1507, 2020.
- [86] Kumari, S.; Mg, S.; Mayor, S. Endocytosis unplugged: Multiple ways to enter the cell. *Cell Res.*, vol. 20, no. 3, p. 256–275, 2010.
- [87] Parton, R. G.; Simons, K. The multiple faces of caveolae. *Nat. Rev. Mol. Cell Biol.*, vol. 8, no. 3, p. 185–194, 2007.
- [88] Behzadia, S.; Serpooshanb, V.; Taa, W.; Hamalyc, M. A.; Alkawarekd, M. Y.; Dreadene, E. C.; Brownf, D.; Alkilanyd, A. M.; Farokhzada, O. C.; Mahmoudi, M. Cellular Uptake of Nanoparticles: Journey Inside the Cell. *HHS Public Access.*, vol. 46, no. 14, p. 4218–4244, 2018.
- [89] Mosquera, J.; García, I.; Liz-Marzán, L. M. Cellular Uptake of Nanoparticles versus Small Molecules: A Matter of Size. *Acc. Chem. Res.*, vol. 51, no. 9, p. 2305–2313, 2018.
- [90] Firdessa, R.; Oelschlaeger, T. A.; Moll, H. Identification of multiple cellular uptake pathways of polystyrene nanoparticles and factors affecting the uptake: Relevance for

drug delivery systems. *Eur. J. Cell Biol.*, vol. 93, no. 8–9, p. 323–337, 2014.

- [91] Donahue, N. D.; Acar, H.; Wilhelm, S. Concepts of nanoparticle cellular uptake, intracellular trafficking, and kinetics in nanomedicine. *Adv. Drug Deliv. Rev.*, vol. 143, p. 68–96, 2019.
- [92] Hillaireau, H.; Couvreur, P. Nanocarriers' entry into the cell: Relevance to drug delivery. *Cell. Mol. Life Sci.*, vol. 66, no. 17, p. 2873–2896, 2009.
- [93] Aderem, A.; Underhill, D. M. Mechanisms of Phagocytosis in Macrophages. *Annu. Rev. Immunol.*, vol. 17, no. 1, p. 593–623, 1999.
- [94] Kuhn, D. A.; Vanhecke, D.; Michen, B.; Blank, F.; Gehr, P.; Petri-Fink, A.; Rothen-Rutishauser, B. Different endocytotic uptake mechanisms for nanoparticles in epithelial cells and macrophages. *Beilstein J. Nanotechnol.*, vol. 5, no. 1, p. 1625–1636, 2014.
- [95] Yameen, B.; Il Choi, W.; Vilos, C.; Swami, A.; Shi, J.; Farokhzad, O. C. Insight into nanoparticle cellular uptake and intracellular targeting. *J. Control. Release.*, vol. 190, p. 485–499, 2014.
- [96] Claus, V.; Jahraus, A.; Tjelle, T.; Berg, T.; Kirschkei, H.; Faulstich, H.; Griffiths, G. Lysosomal enzyme trafficking between phagosomes, endosomes, and lysosomes in J774 macrophages: Enrichment of cathepsin H in early endosomes. *J. Biol. Chem.*, vol. 273, no. 16, p. 9842–9851, 1998.
- [97] Gustafson, H. H.; Holt-Casper, D.; Grainger, D. W.; Ghandehari, H. Nanoparticle uptake: The phagocyte problem. *Nano Today.*, vol. 10, no. 4, p. 487–510, 2015.
- [98] Parton, R. G.; Del Pozo, M. A. Caveolae as plasma membrane sensors, protectors and organizers. *Nat. Rev. Mol. Cell Biol.*, vol. 14, no. 2, p. 98–112, 2013.
- [99] Foroozandeh, P.; Aziz, A. A. Insight into Cellular Uptake and Intracellular Trafficking of Nanoparticles. *Nanoscale Res. Lett.*, vol. 13, no.1, p. 1-12, 2018.
- [100] Bemquerer, M. P.; Jr, C. B.; Brito, H. F.; Teotonio, E. E. S.; Miranda, M.; Teresa, M. Steady-state luminescence investigation of the binding of Eu (III) and Tb (III) ions

- with synthetic peptides derived from plant thionins. *J. Inorg. Biochem.*, vol. 91, p. 363–370, 2002.
- [101] Li, T.; Li, Y.; Xu, G.; Du, G.; Wang, F.; Han, J.; Zhang, J.; Ma, Z.; Liu, Z.; Yao, K. Optical Properties of Monodisperse ZnSe:Mn/ZnS Core–Shell Nanocrystals Synthesized via an Alkylthiol-Assisted Phosphine-Free Method. *Sci. Adv. Mater.*, vol. 9, no. 3/4, 2017.
- [102] Ning, Z.; Molna, M.; Chen, Y.; Friberg, Peter.; Gan, L.; Grena, H. Fu, Y. Role of surface ligands in optical properties of colloidal CdSe/CdS quantum dots. *Phys. Chem. Chem. Phys.*, vol. 13, no. 13, p. 5848, 2011.
- [103] Pradhan, N.; Battaglia, D. M.; Liu, Y.; Peng, X. Efficient, Stable, Small, and Water-Soluble Doped ZnSe Nanocrystal Emitters as Non-Cadmium Biomedical Labels. *Nano Lett.*, vol. 7, no. 2, p. 312–317, 2007.
- [104] Zhou, W.; Liu, R.; Tang, D.; Zou, B. The effect of dopant and optical micro-cavity on the photoluminescence of Mn-doped ZnSe nanobelts. *Nanoscale Res. Lett.*, vol. 8, no. 1, p. 1–10, 2013.
- [105] Deng, Z.; Lie, F. L.; Shen, S.; Ghosh, I.; Mansuripur, M.; Muscat, A. J. Water-based route to ligand-selective synthesis of ZnSe and Cd-doped ZnSe quantum dots with tunable ultraviolet A to blue photoluminescence. *Langmuir*, vol. 25, no. 1, p. 434–442, 2009.
- [106] Wang, C.; Gao, X.; Ma, Q.; and Su, X. Aqueous synthesis of mercaptopropionic acid capped Mn²⁺-doped ZnSe quantum dots. *J. Mater. Chem.*, vol. 19, no. 38, p. 7016–7022, 2009.
- [107] Cooper, J. K.; Gul, S.; Lindley, S. A.; Yano, J.; Zhang, J. Z. Tunable Photoluminescent Core/Shell Cu⁺-Doped ZnSe/ZnS Quantum Dots Codoped with Al³⁺, Ga³⁺, or In³⁺. *ACS Appl. Mater. Interfaces*, vol. 7, no. 18, p. 10055–10066, 2015.
- [108] Suyver, J. F.; Wuister, S. F.; Kelly, J. J.; Meijerink. Luminescence of nanocrystalline ZnSe : Mn²⁺. *Phys. Chem. Chem. Phys.*, vol. 2, p. 5445–5448, 2000.

- [109] Chem, J. M.; Shao, P.; Wang, H.; Li, Y. White light emission from Mn-doped ZnSe d-dots synthesized continuously in microfluidic reactors. *J. Mater. Chem.*, vol. 21, no. 44, p. 17972–17977, 2011.
- [110] “Manganese Doped Fluorescent Paramagnetic Nanocrystals for Dual-Modal Imaging Manganese Doped Fluorescent Paramagnetic Nanocrystals for Dual-Modal Imaging. *small.*, vol. 10, no. 23, p. 4961–4966, December, 2014.
- [111] Zhang, L. J.; Shen, X. C.; Liang, H.; Chen, F. Y.; Huang, H. J. Phosphine-free synthesis of ZnSe:Mn and ZnSe:Mn/ZnS doped quantum dots using new Se and S precursors. *New J. Chem.*, vol. 38, no. 1, p. 448, 2014.
- [112] J. Li, Y. Liu, J. Hua, L. Tian, and J. Zhao. Photoluminescence properties of transition metal-doped Zn–In–S/ZnS core/shell quantum dots in solid films,” *RSC Adv.*, vol. 6, no. 50, p. 44859–44864, 2016.
- [113] Salem, A.; Saion, E.; Al-Hada, N. M.; Shaari, A. H.; Kamari, H. M.; Soltani, N. Radiman, S. Formation of a colloidal CdSe and ZnSe quantum dots via a gamma radiolytic technique. *Appl. Sci.*, vol. 6, no. 10, p. 278, 2016.
- [114] Soltani, N.; Saion, E.; Hussein, M. Z.; Erfani, M.; Abedini, A.; Bahmanrokh, G.; Navasery, M.; Vaziri, P. Visible light-induced degradation of methylene blue in the presence of photocatalytic ZnS and CdS nanoparticles. *Int. J. Mol. Sci.*, vol. 13, no. 10, p. 12242–12258, 2012.
- [115] Aboulaich, A.; Geszke, M.; Balan, L.; Ghanbaja, J.; Medjahdi, G.; Schneider, R. Water-Based Route to Colloidal Mn-Doped ZnSe and Core / Shell ZnSe / ZnS Quantum Dots. *Inorg. Chem.*, vol. 49, no. 23, p. 10940–10948, 2010.
- [116] Hossu, M.; Schaeffer, R. O.; Ma, L.; Chen, W.; Zhu, Y.; Sammynaiken, R.; Joly, A. G. On the luminescence enhancement of Mn²⁺ by co-doping of Eu²⁺ in ZnS:Mn,Eu. *Opt. Mater. (Amst.)*, vol. 35, no. 8, p. 1513–1519, 2013.
- [117] Li, K.; Geng, D.; Shang, M.; Zhang, Y.; Lian, H.; Lin, J. Color-tunable luminescence and energy transfer properties of Ca₉Mg(PO₄)₆F₂:Eu²⁺, Mn²⁺ phosphors for UV-

- LEDs. *J. Phys. Chem. C*, vol. 118, no. 20, p. 11026–11034, 2014.
- [118] Dabbousi, B. O.; Rodriguez-Viejo, J.; Mikulec, F. V.; Heine, J. R.; Mattoussi, H.; Ober, R.; Jensen, K. F.; Bawendi, M. G. (CdSe)ZnS core-shell quantum dots: Synthesis and characterization of a size series of highly luminescent nanocrystallites. *J. Phys. Chem. B.*, vol. 101, no. 46, p. 9463–9475, 1997.
- [119] Li, L.; Reiss, P.; Protie, M. Core / Shell Semiconductor Nanocrystals. *small.*, vol. 5, no. 2, p. 154–168, 2009.
- [120] Xia, X.; Liu, Z.; Du, G.; Li, Y.; Ma, M. Structural Evolution and Photoluminescence of Zinc-Blende CdSe-Based CdSe / ZnS Nanocrystals. *J. Phys. Chem.*, vol. 114, no. 32, p. 13414–13420, 2010.
- [121] Bae, W. K.; Char, K.; Hur, H.; Lee, S. Single-Step Synthesis of Quantum Dots with Chemical Composition Gradients. *Chem. Mater.* vol. 20, no. 2, p. 531–539, 2008.
- [122] Acharya, K. P.; Nguyen, H. M.; Paulite, M.; Piryatinski, A.; Zhang, J.; Casson, J. L.; Xu, H.; Htoon, H.; Hollingsworth, J. A. Elucidation of Two Giants : Challenges to Thick-Shell Synthesis in CdSe/ZnSe and ZnSe/CdS Core/Shell Quantum Dots. *J. Am. Chem Soc.*, vol. 137, no. 11, p. 6–9, 2015.
- [123] Guo, X.; Kuang, Y.; Wang, S.; Li, Z.; Shen, H.; Guo, L. Shell-dependent blinking behavior and fluorescence dynamics of single ZnSe/CdS core/shell quantum dots. *Nanoscale.*, vol. 10, p. 18696–18705, 2018.
- [124] Veamatahau, A.; Jiang, B.; Seifert, T.; Makuta, S.; Latham, K.; Kanehara, M.; Teranishi, T.; Tachibana, Y. Origin of surface trap states in CdS quantum dots: Relationship between size dependent photoluminescence and sulfur vacancy trap states. *Phys. Chem. Chem. Phys.*, vol. 17, no. 4, p. 2850–2858, 2015.
- [125] Watanabe, T.; Iso, Y.; Isobe, T.; and Sasaki, H. Photoluminescence color stability of green-emitting InP/ZnS core/shell quantum dots embedded in silica prepared via hydrophobic routes. *RSC Adv.*, vol. 8, no. 45, p. 25526–25533, 2018.
- [126] Chen, D.; Zhao, F.; Qi, H.; Rutherford, M.; Peng, X. Bright and Stable Purple / Blue

Emitting CdS / ZnS Core / Shell Nanocrystals Grown by Thermal Cycling Using a Single-Source Precursor. *Chem. Mater.*, vol. 119, no. 11, p. 1437–1444, 2018.

- [127] Kim, M. R.; Kang, Y.; Jang, D. Synthesis and Characterization of Highly Luminescent CdS @ ZnS Core - Shell Nanorods. *J. Phys. Chem. C.*, vol. 111, no. 50, p. 18507–18511, 2007.
- [128] Wang, W.; Germanenko, I.; El-shall, M. S. Room-Temperature Synthesis and Characterization of Nanocrystalline CdS, ZnS, and Cd_xZn_{1-x}S. *Chem. Mater.*, vol. 14, no. 7, p. 3028–3033, 2006.
- [129] Xie, R.; Kolb, U.; Li, J.; Basche, T.; Mews, A. Synthesis and Characterization of Highly Luminescent CdSe-Core CdS/Zn_{0.5}Cd_{0.5}S/ZnS Multishell Nanocrystals. *J. Am. Chem. Soc.*, vol. 127, no. 20, p. 7480–7488, 2005.
- [130] Celebi, S.; Erdamar, A. K.; Sennaroglu, A.; Kurt, A.; Acar, H. Y. Synthesis and Characterization of Poly(acrylic acid) Stabilized Cadmium Sulfide Quantum Dots. *J. Phys. Chem. B.*, vol. 111, no. 44, p. 12668–12675, 2007.
- [131] Manna, L.; Scher, E. C.; Li, L.; Alivisatos, A. P. Epitaxial Growth and Photochemical Annealing of Graded CdS / ZnS Shells on Colloidal CdSe Nanorods. *J. Am. Chem. Soc.*, vol. 124, no. 24, p. 7136–7145, 2002.
- [132] Datta, A.; Panda, S. K.; Chaudhuri, S. Synthesis and Optical and Electrical Properties of CdS / ZnS Core / Shell Nanorods. *J. Phys. Chem. C.*, vol. 111, no. 46, p. 17260–17264, 2007.
- [133] Dabbousi, B. O.; Rodriguez-Viejo, J.; Mikulec, F. V.; Heine, J. R.; Mattoussi, H.; Ober, R.; Jensen, K. F.; Bawendi, M. G. (CdSe) ZnS Core - Shell Quantum Dots : Synthesis and Characterization of a Size Series of Highly Luminescent Nanocrystallites. *J. Phys. Chem. B.*, vol. 101, no. 46, p. 9463–9475, 1997.
- [134] Chu, Z.; Huang, Y.; Tao, Q.; Li, Q. Cellular uptake, evolution, and excretion of silica nanoparticles in human cells. *Nanoscale.*, vol. 3, no. 8, p. 3291, 2011.
- [135] Herd H.; Daum, N.; Jones, A. T.; Huwer, H.; Ghandehari, H.; Lehr, C. Nanoparticle

- Geometry and Surface Orientation Influence Mode of Cellular Uptake. *ACS Nano.*, vol.7, no. 3, p. 1961–1973, 2013.
- [136] Hunt, N. J.; Lockwood, G. P.; Couteur, F. H.; McCourt, P. A. G.; Singla, N.; Kang, S. W. S.; Burgess, A.; Kuncic, Z.; Couteur, D. G.; Cogger, V. C. Rapid Intestinal Uptake and Targeted Delivery to the Liver Endothelium Using Orally Administered Silver Sulfide Quantum Dots. *ACS Nano.*, vol. 14, no. 2, p. 1492–1507, 2020.
- [137] Halder, A.; Godoy-Gallardo, M.; Ashley, J.; Feng, X.; Zhou, T.; Hosta-Rigau, L.; Sun, Yi. One-pot green synthesis of biocompatible graphene quantum dots and their cell uptake studies. *ACS Appl. Bio Mater.*, vol. 1, no. 2, p. 452–461, 2018.
- [138] Cheng, X.; Tian, X.; Wu, A.; Li, J.; Tian, J.; Chong, Y.; Chai, Z.; Zhao, Y.; Chen, C.; Ge, C. Protein Corona Influences Cellular Uptake of Gold Nanoparticles by Phagocytic and Nonphagocytic Cells in a Size-Dependent Manner. *ACS Appl. Mater. Interfaces.*, vol. 7, no. 37, p. 20568–20575, 2015.
- [139] Wang, X.; Wang, X.; Bai, X.; Yan, L.; Liu, T.; Wang, M.; Song, Y.; Hu, G.; Gu, Z.; Miao, Q.; Chen, C. Nanoparticle Ligand Exchange and Its Effects at the Nanoparticle-Cell Membrane Interface. *Nano Lett.*, vol. 19, no. 1, p. 8–18, 2019.
- [140] Rojas-Gutierrez, P. A.; Bekah, D.; Seuntjens, J.; Dewolf, C.; Capobianco, J. A. Cellular Uptake, Cytotoxicity and Trafficking of Supported Lipid-Bilayer-Coated Lanthanide Upconverting Nanoparticles in Alveolar Lung Cancer Cells. *ACS Appl. Bio Mater.*, vol. 2, no. 10, p. 4527–4536, 2019.
- [141] Hewlett, L. J.; Prescott, A. R.; Watts, C. The coated pit and macropinocytic pathways serve distinct endosome populations. *J. Cell Biol.*, vol. 124, no. 5, p. 689–703, 1994.
- [142] Ehrlich, M.; Boll, W.; Oijen, A.; Hariharan, R.; Chandran, K.; Nibert, M. L.; Kirchhausen, T. Endocytosis by random initiation and stabilization of clathrin-coated pits. *Cell.*, vol. 118, no. 5, p. 591–605, 2004.
- [143] Barber, V. C. THE FINEST STRUCTURE of THE Statocyst. *Zellforschung.*, vol. 107, no. 5, p. 91–107, 1966.

- [144] Chen, N.; He, Y.; Su, Y.; Li, X.; Huang, Q.; Wang, H.; Zhang, X.; Tai, R.; Fan, C. The cytotoxicity of cadmium-based quantum dots. *Biomaterials.*, vol. 33, no. 5, p. 1238–1244, 2012.
- [145] Peuschel, H.; Ruckelshausen, T.; Kiefer, S.; Silina, Y.; Kraegeloh, A. Penetration of CdSe/ZnS quantum dots into differentiated vs undifferentiated Caco-2 cells. *J. Nanobiotechnology.*, vol. 14, no. 1, p. 1–19, 2016.
- [146] Rabouw, F.T.; Mello, D. C. Excited-state dynamics in colloidal semiconductor nanocrystals. *Top Curr Chem (Z).*, no. 58, p. 374, 2016.
- [147] Zheng, Y; Gao, S; Ying, J. Y. Synthesis and Cell-Imaging Applications of Glutathione-Capped CdTe Quantum Dots. *Advanced Materials.*, vol. 19, p. 376-380, 2007.

Annex A

Orange-Emitting ZnSe:Mn²⁺ Quantum Dots as Nanoprobes for Macrophages

Zahid U. Khan, Mayara K. Uchiyama, Latif U. Khan, Eduardo M. Ramos-Sanchez, Luiza Campos Reis, Marcelo Nakamura, Hiro Goto, Ana O. De Souza, Koiti Araki, Hermi F. Brito, and Magnus Gidlund*

Cite This: <https://dx.doi.org/10.1021/acsanm.0c02242>

Read Online

ACCESS

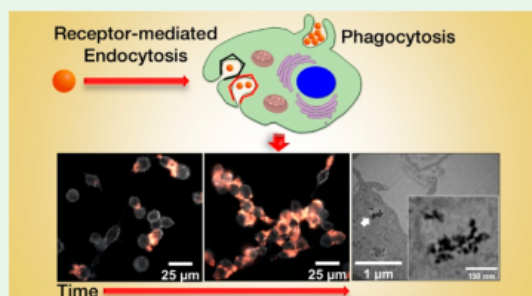
Metrics & More

Article Recommendations

Supporting Information

ABSTRACT: The biocompatibility, bionanointeraction, uptake efficiency, and entry pathway of luminescent nanomaterials are the key factors to understand development of an efficient bionanoprobe. The foremost objective of this work is to explore the potential of 3-mercaptopropionic acid (3-MPA) capped ZnSe:*x*Mn²⁺ (*x* = 5, 10, and 15 mol %) quantum dots (QDs) for the development of bionanoprobe used in future biological and clinical applications. For this purpose, highly intense orange-emitting activator Mn²⁺ ion doped ZnSe QDs were synthesized via a high-temperature organometallic method and rendered water-soluble by a ligand exchange approach. The morphological and physicochemical characterizations displayed the ultrasmall zinc-blend cubic crystal structure of QDs with an elliptical shape nanocrystals and average diameter of 4 nm. The luminescent nanomaterials exhibited orange emission centered at 584 nm under excitation at 385 nm. The biocompatibility, time-dependent cellular uptake, and the uptake mechanism of QDs were studied in RAW 264.7 macrophages, accomplished by various cytotoxicity assays, CytoViva hyperspectral enhanced dark-field and dual-mode fluorescence (DMF) microscopy, and transmission electron microscopy (TEM) images. The cytotoxicity study did not confirm any noticeable deleterious effect of QDs within incubation for 6 h. The fluorescence images of cells incubated with QDs showed efficient emission, which is a manifestation that QDs are photochemically stable in the intracellular environment. The cellular uptake findings demonstrated that the QDs were predominantly internalized via clathrin- and caveolae-mediated pathways. After the uptake, QDs aggregates appeared inside the vesicles in the cytoplasm, and their number and size gradually increased as a function of time. Nevertheless, the fluorescent QDs presented remarkable colloidal stability in various media, biocompatibility within the designated time, efficient time-dependent uptake, and distinct entry pathway in RAW macrophages, suggesting promising candidates to explore for the development of future bionanoprobes.

KEYWORDS: bionanoprobe, fluorescent nanocrystals, RAW 264.7, biocompatibility, time-dependent uptake, entry pathway



Fe₃O₄@SiO₂ Nanoparticles Concurrently Coated with Chitosan and GdOF:Ce³⁺,Tb³⁺ Luminophore for Bioimaging: Toxicity Evaluation in the Zebrafish Model

Latif U. Khan,^{*,†} Gabriela H. da Silva,^{†,‡} Aline M. Z. de Medeiros,^{†,‡} Zahid U. Khan,[§] Magnus Gidlund,[§] Hermi F. Brito,^{||} Oscar Moscoso-Londoño,^{⊥,#} Diego Muraca,[⊥] Marcelo Knobel,[⊥] Carlos A. Pérez,^{*,||} and Diego Stéfani T. Martinez^{*,†,‡}

[†]Brazilian Nanotechnology National Laboratory (LNNano), Brazilian Center for Research in Energy and Materials (CNPEM), 13084-970 Campinas, São Paulo, Brazil

[‡]Center of Nuclear Energy in Agriculture (CENA), University of São Paulo (USP), 13416-000 Piracicaba, São Paulo, Brazil

[§]Department of Immunology, Institute of Biomedical Sciences-IV, University of Sao Paulo (USP), 05508-000 São Paulo, São Paulo, Brazil

^{||}Department of Fundamental Chemistry, Institute of Chemistry, University of Sao Paulo (USP), 05508-000 São Paulo, São Paulo, Brazil

[⊥]Institute of Physics "Gleb Wataghin", University of Campinas (UNICAMP), 13083-859 Campinas, São Paulo, Brazil

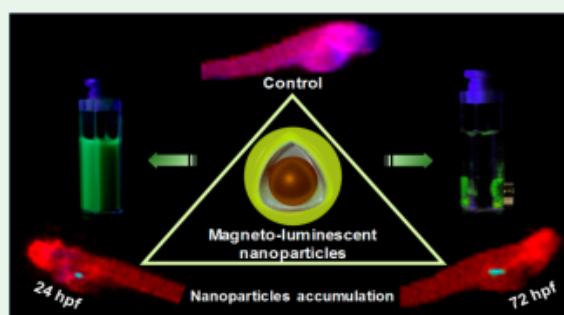
[#]Faculty of Engineering, Autonomous University of Manizales, Antigua Estación del Ferrocarril, 170003 Manizales, Colombia

[¶]Brazilian Synchrotron Light Laboratory (LNLS), Brazilian Center for Research in Energy and Materials (CNPEM), 13084-970 Campinas, São Paulo, Brazil

Supporting Information

ABSTRACT: In this work, design and physicochemical characterization of a biocompatible nanoplatform with integrated photoluminescence and magnetic properties were reported. The potential in vivo toxicity was assessed by exploring the biodistribution of nanoparticles using synchrotron X-ray fluorescence (SXRF) imaging in the zebrafish embryos as a biological model. Their synthesis is accessible through combining magnetic iron oxide nanoparticles with Ce³⁺- and Tb³⁺-doped GdOF luminophore and concurrent capping in situ with chitosan biopolymer. The Fe₃O₄@SiO₂/GdOF:*x*Ce³⁺,*y*Tb³⁺ nanoparticles manifested near superparamagnetic behavior at 300 K, displaying green emission lines, arising from the characteristic ⁵D₄ → ⁷F_J transitions (*J* = 6–0) of Tb³⁺ ion. The limited permeability of the chorion membrane is a critical factor in toxicity screening, a potential approach to remove the chorion and expose the chorion-off zebrafish embryos to nanoscale materials. Accordingly, multifunctional nanoparticles exhibited no acute toxicity to the with-chorion and chorion-off zebrafish embryos up to 100 mg L⁻¹ exposure concentration, suggesting remarkable in vivo biocompatibility. By assessing the nanobio interaction via deep-tissue SXRF imaging, it was visualized that the distribution of Gd and Fe elements had occurred with a roughly constant relative ratio in the whole body of early-stage embryos. However, the elements mapping data revealed a predominant localization of Gd and Fe in the gastrointestinal tract, manifesting bioaccumulation of magneto-luminescent nanoparticles as an integrated nanoplatform in the respective region. This result demonstrated that the particles' uptake by embryos were mostly through oral exposure rather than the dermal pathway, offering a new route to oral administration of nanoparticles for future biological and environmental applications.

KEYWORDS: multifunctional nanoparticles, magnetism, green-emission, nanotoxicity, nanosafety, μ -XRF imaging



Advanced Optical Materials

Wide Visible-Range Activatable Fluorescence ZnSe:Eu²⁺/Mn²⁺@ZnS Quantum dots as Nanoprobe for Bioimaging

--Manuscript Draft--

Manuscript Number:	adom.202001973
Article Type:	Full Paper
Corresponding Author:	Hermi Felinto Brito UNIVERSITY OF SAO PAULO SAO PAULO, São Paulo BRAZIL
Corresponding Author E-Mail:	hefbrito@iq.usp.br
Order of Authors:	Zahid Ullah Khan, Doctrate Mayara Klimuk Uchiyama, Doctrate Latif Ullah Khan, Doctrate Koiti Araki, Doctrate Hiro Goto Maria C. F. C. Felinto Ana Olivia Souza, Doctrate Hermi Felinto Brito Magnus Ake Gidlund, Doctrate
Keywords:	Quantum dots; Mn ²⁺ and Eu ²⁺ activators; Multicolor-tunable fluorescence; Cellular labeling and imaging; Cellular uptake mechanism and Exocytosis
Section/Category:	
Abstract:	The development of bionanoprobe fundamentally relies upon the precise knowledge of particle-cell interaction, movement of a particle in and out of the cell, and the fate of particle. We present the design and engineering of water-dispersible Eu ²⁺ /Mn ²⁺ -doped ZnSe@ZnS core/shell quantum dots (QDs) and the study of their potentiality for biomedical applications in RAW 264.7 macrophages. A novel approach is developed to relieve the excitation constraint of wide bandgap ZnSe by co-incorporation of Eu ²⁺ /Mn ²⁺ , enabling the QDs to be excited at a wide UV-visible range. The QDs address luminescence tunable emission colors by a gradual increase in Eu ²⁺ concentration and at a fixed amount of Mn ²⁺ , concurrently leveraging the Mn ²⁺ emission intensity via energy transfer from the Eu ²⁺ to Mn ²⁺ . The QDs present high cell viability above 85%, inducing no cell activation. The detailed analyses of QDs treated cells by CytoViva microscopy confirm a systematic color-tunable fluorescence and its intensity enhances as a function of incubation time. The cells internalize the QDs predominantly via caveolae-mediated endocytosis and macropinocytosis pathways and retained an efficient amount for 24 h. The unique color tunability, and consistent high fluorescence emission over days of QDs can be useful for developing multiplex fluorescent nanoprobe.

CURRICULUM SUMMARY

PERSONAL INFORMATION

Name: **Zahid Ullah Khan**

Biocologia USP

Avenida Prof. Lineu Prestes, 2415 - Edifício ICB – III,

Cidade Universitária, CEP. 05508-900

Universidade São Paulo-USP

São Paulo-SP-Brasil

Email: zahidmwt1@gmail.com / zahidkhan@usp.br

Education

Bachelor of Science (BSc), 2008.

Master of Science (MSc) in Chemistry, 2010.

Master of Philosophy (M.Phil) in Biochemistry, 2015.

Ph.D, 2016-present.

MAIN SCIENTIFIC PUBLICATIONS

- 1) **Khan, Z. U.**; Uchiyama, M. K.; Khan, L. U.; Araki, K.; Goto, H.; Maria. C. F. C. Felinto.; Souza, A. O.; Brito, H. F.; Gidlund, M. Wide Visible-Range Fluorescence ZnSe:Eu²⁺/Mn²⁺@ZnS QDs as Nanoprobe for Bioimaging. *Advanced Optical Materials*. **Submitted**
- 2) **Khan, Z. U.**; Uchiyama, M. K.; Khan, L. U.; Ramos-Sanchez, E. M.; Reis, L. C.; Nakamura, M.; Goto, H.; Souza, A. O.; Araki, K.; Brito, H. F.; Gidlund, M. Orange-Emitting ZnSe:Mn²⁺ Quantum Dots as Nanoprobes for Macrophages. *ACS Applied Nanomaterials (ACS)*, September 2020, <https://doi.org/10.1021/acsanm.0c02242>
- 3) Khan, L.U.; Silva, G.H.; de Medeirosa, A.M. Z.; **Khan, Z.U.**; Gidlund, M.; Brito, H.F.; Moscoso-Londoño, O.; Muraca, D.; Knobel, Marcelo; Pérez, C.A.; Martinez, D.S.T. Fe₃O₄@SiO₂ nanoparticles concurrently coated with chitosan and GdOF:Ce³⁺,Tb³⁺

luminophore for bioimaging: Toxicity evaluation in zebrafish model. *ACS Applied Nanomaterials* (ACS), Vol. 2, pp. 3414-3425, May 2019, <https://doi.org/10.1021/acsanm.9b00339>

- 4) Khan L.U.; **Khan, Z.U.**; Rodrigues, R.V.; Costa, L.S.; Gidlund, M.; Brito, H.F. Synthesis and characterization of tunable color upconversion luminescence β -NaGdF₄:Yb³⁺,Er³⁺ nanoparticles. *Journal of Materials Science: Materials in Electronics* (Springer), Vol. 30, pp 16856–16863, May 2019, DOI: <https://doi.org/10.1007/s10854-019-01462-2>.
- 5) Shrivastava, N.; Khan, L.U.; **Khan, Z.U.**; Vargas, J.M.; Moscoso-Londoño, O.; Ospina, C.; Brito, H.F.; Felinto, M.C.F.C.; Knobel, Marcelo; Sharma, S.K. Building block magneto-luminescent nanomaterials of iron-oxide@ZnS/LaF₃:Ce³⁺,Gd³⁺,Tb³⁺ with green emission. *Journal of Material Chemistry C. (RSC)*, Vol. 5, pp. 2282-2290 January 2017. <https://doi.org/10.1039/C6TC05053K>

CHAPTERS/BOOKS

CHAPTERS

- 1) Khan L.U.; **Khan, Z.U.** Bifunctional Nanomaterials: Magnetism, luminescence and Multimodal Biomedical Applications. Chapter 4, pp 121-171, In., *Complex Magnetic Nanostructures Synthesis, Assembly and Applications*. Sharma, S.K. (Editor), Springer International Publishing (SPRINGER NATURE), 2017 (ISBN 978-3-319-52087-2). DOI: https://doi.org/10.1007/978-3-319-52087-2_4.
- 2) Khan L.U.; **Khan, Z.U.** Rare Earths Luminescence: Electronic Spectroscopy and Applications. Chapter 10, pp 345-404, In, *Handbook of Materials Characterization*. Sharma, S.K.; Verma, D.S.; Khan, L.U.; Kumar, S.; Khan, S.B. (Editors), Springer International Publishing (SPRINGER NATURE), 2018. DOI: https://doi.org/10.1007/978-3-319-92955-2_10.

SUMMARIES PUBLISHED IN CONFERENCE PROCEEDINGS

- 1) **Khan, Z. U.**; Brito, H. F.; Khan, L.U.; Goto, H.; Sanchez, E.; Gidlund, M. A. Synthesis and characterization of ZnSe:xMn²⁺ quantum dots. Analysis of their toxicity and kinetic of uptake in vitro (RAW 264-7) as a first step in the development of a Diagnostic Nanoprobe. 8th International Conference on Optical, Optoelectronic and Photonic Materials and Applications (ICOOPMA2018), 2018, Maresias-SP.
- 2) **Khan Z. U.** Color-tunable ZnSe:Mn²⁺/Eu²⁺ and ZnSe:Mn²⁺,Eu²⁺/ZnS core/shell quantum dots for use as a biosensor in clinical diagnostic: Evaluation of toxicity and functional uptake by macrophages. J Biotechnol Biomater., 20019, vol. 09.
- 3) Khan, L. U.; **Khan, Z. U.** Size dependent tunable color upconversion luminescence Er³⁺ and Yb³⁺ doped NaGdF₄ nanoparticles. In: 8th International Conference on Optical, Optoelectronic and Photonic Materials and Applications (ICOOPMA), 2018, Maresias Sao Paulo.
- 4) Sharma, Surender K.; Shrivastava, Navadeep; Khan, L. U.; **Khan, Z. U.**; Vargas, J. M.; Moscoso-Londono, O.; Ospina, C.; Brito, H. F.; Javed, Y.; Felinto, M. C. F. C.; Menezes, A. S.; Knobel, M. Combinatorial investigation of magneto-luminescence properties of bifunctional nanostructures of iron-oxide@ternary doped rare-earth fluorides. In: XVI Brazil MRS Meeting (SBPMAT), 2017, Gramado/RS.
- 5) **Khan, Z. U.**; Khan, L. U.; Brito, H. F.; Gidlund, M. A. Green-emitting magnetic nanoensembles of Fe₃O₄@SiO₂@GdOF:Ce³⁺,Tb³⁺: Toxicity Assessment in Zebrafish Embryos. In: International Conference on Agricultural and Food Science & 7th International Conference on Biotechnology and Bioengineering, 2017. v. 1. p. 29-29.
- 6) Shrivastava, N.; Khan, L.U.; **Khan, Z.U.**; Vargas, J.M.; Brito, H.F.; Felinto, M.C.F.C.; Sharma, S.K. Optical and magnetic nanocomposites containing Fe₃O₄@ZnS coated with green-emitting LaF₃:Ce³⁺,Gd³⁺,Tb³⁺ materials. In: XV Brazil MRS Meeting (SBPMAT), Campinas-SP, 2016.
- 7) **Khan, Z. U.**; Khan, L.U.; Goto, H.; Felinto, M.C.F.C.; Brito, H.F.; Gidlund, M.A. Development of optical and magnetic immunoassay nanoprobe based on Fe₃O₄@SiO₂@GdF₃:Ce³⁺,Tb³⁺ for the quantitative study of phagocytes. In: 6th

International Conference on Excited States of Transitions Elements, Polanica-Zdrój, 2016.

SCIENTIFIC AWARDS AND SCHOLARSHIPS

- 1) 2016: Best Poster award, 2nd Biotechnology World Convention, *OMICS International*, USA, held at Sao Paulo Brazil (**Presenter**).

- 2) 2016–2020: Doctorate scholarship from *The World Academy of Sciences for the advancement of science in developing countries (TWAS)* (**Principal Investigator, Supervisor: Prof. Dr. Magnus Ake Gidlund**).